Advancements in Optical Diagnostics for Experimental Aeroelasticity
Benchmarking the cylinder-foil system

Gonzalez Saiz, G.

Citation (APA)
Gonzalez Saiz, G. (2023). *Advancements in Optical Diagnostics for Experimental Aeroelasticity: Benchmarking the cylinder-foil system*. [Dissertation (TU Delft), Delft University of Technology]. https://doi.org/10.4233/uuid:65a92e32-3830-4c4e-a244-ad5bbcb7af89

Important note
To cite this publication, please use the final published version (if applicable).
Please check the document version above.

ADVANCEMENTS IN OPTICAL DIAGNOSTICS FOR EXPERIMENTAL AEROELASTICITY

BENCHMARKING THE CYLINDER-FOIL SYSTEM

ADVANCEMENTS IN OPTICAL DIAGNOSTICS FOR EXPERIMENTAL AEROELASTICITY

BENCHMARKING THE CYLINDER-FOIL SYSTEM

Dissertation

for the purpose of obtaining the degree of doctor
at Delft University of Technology,
by the authority of the Rector Magnificus, Prof.dr.ir. T.H.J.J van der Hagen,
Chair of the Board of Doctorates,
to be defended publicly on
Wednesday 6th December 2023 at 17:30 o'clock

by

Gabriel GONZÁLEZ SAIZ

Master of Science in Aeronautical Engineering,
University Carlos III of Madrid, Spain,
born in Madrid, Spain.

This dissertation has been approved by the *promotors.*

Composition of the doctoral committee:

Rector Magnificus,	chairperson
Prof. dr. F. Scarano,	Delft University of Technology, *promotor*
Dr. A. Sciacchitano,	Delft University of Technology, *copromotor*

Independent members:

Prof. dr. ir. C.J. Simão Ferreira	Delft University of Technology
Prof. dr. A. Schröder	German Aerospace Center (DLR)
Prof. dr. F. Coletti	Swiss Federal Institute of Technology (ETH Zurich)
Dr. L. Chatellier	Université de Poitiers (CNRS)
Dr. A. Nila	LaVision GmbH

Reserve members:

Prof. dr. M. Kotsonis	Delft University of Technology

Success is not final; failure is not fatal:
It is the courage to continue that counts.

Winston S. Churchill

CONTENTS

SUMMARY

Experimental aeroelasticity has been hindered by the intrusivity of measurement equipment and complexity of the experimental setups. Advancements in hardware development have been encouraging optical tracking techniques to replace cross correlation approaches in experimental aerodynamics. However, digital image correlation (DIC) is still the standard optical technique in structural diagnostics. The first experiment of the dissertation assesses the accuracy of an established tracking technique, such as Shake-the-Box, for tracking surface markers on a moving panel, comparing it to DIC. Despite being outperformed in terms of spatial resolution by DIC, surface marker tracking resulted in the same order of accuracy, making structural tracking suitable for large-scale applications. Such results imply the feasibility of characterizing experimentally aeroelastic problems by tracking, in a simultaneous manner, flow tracers and surface markers.

Collar's triangle illustrates the interaction of the forces involved in the aeroelastic problem: aerodynamic, elastic, and inertial. Measuring simultaneously all three components implies the closure of the triangle, required to fully understand the fluid-structure coupling of aeroelastic phenomena. In this dissertation, an experimental methodology is proposed to study aeroelastic systems by evaluating the three physical mechanisms that produce Collar's forces. It is achieved with a single optical system, by tracking simultaneously flow tracers and surface markers. The evaluation of the forces brings the Collar closure criterion, which considers the residual of the force equilibrium as a measure of the accuracy. The experiment regards Lagrangian particle tracking with a high-speed 4-camera system and LED illumination. The model is a benchmark problem of fluid-structure interaction, a cylinder with a flexible splitter plate attached to its rear. Results reveal that the most challenging step of the force estimation is the elastic force, which relies on structural spatial resolution, often disregarded in large-scale aeroelastic measurements.

Later, the experimental cylinder-foil case is explored further to understand the coupling mechanism between the cylinder wake and the flexible splitter plate. Several regimes of foil motion are imaged and identified based on the amplitude and span-wise coherence: low oscillations, resonance, chaotic, and bi-stable. Two regimes, resonance and chaotic, were analysed with Proper Orthogonal Decomposition to identify the most dominant modes, and compared to a clean cylinder configuration. Different coupling mechanisms are recognized for each regime. The motion of the structure at resonance was driven by the dominant features of the flow, acting as a single way channel. Conversely, the chaotic regime exhibited a 2-way coupling between flow and structure.

Particle-based optical methods offer an increased local accuracy by eliminating windowing modulation. The increased performance comes at the expense of gappy data, which becomes more critical in aeroelastic environments where the solid-fluid interphase is crucial to close the problem. The last part of this dissertation is devoted to physics-based data assimilation to increase spatial resolution in, first, general fluid do-

mains by using temporal information of the particles, and second, close vicinity of non-uniform solid boundaries. Vortex-in-Cell Time-Segment Assimilation (VIC-TSA) is a technique that considers data distributed over a finite time-segment to reconstruct the optimal 3D vorticity and velocity fields described within such segment. Its principle is presented by identifying three main data reduction regimes, which are verified by a numerical analysis. The numerical assessment with synthetic 3D fields of sinusoids shows the potential of using long time segments when tracers concentration is low. The technique is further challenged with an experimental dataset of a cylinder wake. The VIC-TSA analysis reveals an optimum track time length longer than the theoretically predicted. The topology analysis of the vortex structure of the cylinder wake confirms the increase in spatial resolution by detecting sub-structures at a scale comparable to the average inter-particle distance.

On the other hand, two approaches based on computational fluid-structure interaction frameworks are proposed to handle deformable solid walls intruding into the fluid domain by adapting the existing VIC+ technique. The Arbitrary-Lagrangian-Eulerian VIC+ method, ALE-VIC+, includes a mesh deformation step to adapt the fluid domain to the solid boundaries. Conversely, ImVIC+ makes use of immersed boundary treatments without deforming the computational grid, thus benefiting from FFT-based Poisson solvers for pressure evaluation. The proposed approaches are assessed with a numerical test dealing with flow over periodic hills, where higher accuracy than the reference VIC+ is achieved close to the walls. An experimental analysis, featuring a turbulent boundary layer interacting with an unsteadily moving elastic panel, shows accurate pressure distribution computation over the surface with the proposed techniques.

SAMENVATTING

Experimentele aëro-elasticiteit wordt gehinderd door de indringendheid van meetapparatuur en de complexiteit van de experimentele meetopstelling. Vooruitgang in hardwareontwikkelingenheeft optische particle trackingtechniekenin staat gebrachtom kruiscorrelatiebenaderingen te vervangen in de experimentele aerodynamica. *Digital Image Correlation* (DIC) is echter nog steeds de standaard optische meettechniek op hetgebied van de structurele meetmethoden. Het eerste experiment van het proefschrift beoordeelt de nauwkeurigheid van een veel gebruikteparticle tracking techniek, zoals Shake-the-Box, voor het volgen van oppervlaktemarkersop een bewegend paneel, en vergelijkt deze met DIC. Ondanks dat DIC beter presteert in ruimtelijke resolutie, resulteerde het volgenvan oppervlaktemarkersin 3D dezelfde orde van nauwkeurigheid, wat structureel volgen geschikt maakt voor grootschalige toepassingen. Dergelijke resultaten impliceren de haalbaarheid van het experimenteel karakteriseren van aëro-elastische problemen door gelijktijdig stromingstracers en oppervlaktemarkerste volgen.

Collar's triangle illustreert de interactie van de krachten die betrokken zijn bij het aëro-elastische probleem: aërodynamisch, elastisch en traagheid. Het gelijktijdig meten van alle drie de componenten maakt het mogelijkCollar's triangleals het warete "sluiten", wat nodig is om de koppeling tussen stromingen constructie onder invloed vanaëroelastische verschijnselen volledig te begrijpen. In dit proefschrift wordt een experimentele methodologie voorgesteld om aëro-elastische systemen te bestuderen door de drie fysische mechanismen te evalueren die de krachten van Collar's triangleproduceren. Dit wordt bereikt met een enkel optisch meetsysteem door gelijktijdig stromingstracers en oppervlaktemarkers te volgen. De evaluatie van de krachten brengt het Collar's- sluitingscriterium met zich mee waarinhet residu van het krachtenevenwicht beschouwt wordtalsmaat voor de nauwkeurigheid. Het experiment betreft Lagrangiaanse particle tracking met een hogesnelheidmeetsysteem van4 camera's en LED-verlichting. Het gebruiktemodel vormt eenbenchmark experimentele opstelling van de stroming- constructieinteractie, namelijkeen cilinder met flexibele splitterplaat bevestigd aan de achterkant. De resultaten laten zien dat de meest uitdagende stap van de krachtbepalingende elastische kracht is, die afhankelijk is van de ruimtelijke resolutie waarmee de positie van de constructie gemeten wordt. Iets datvaak buiten beschouwing wordt gelaten bij grootschalige aëro-elastische metingen.

Later wordt deexperimentele cilinder-splitterplaatopstellingverder onderzocht om het koppelingsmechanisme tussen het cilinderzog en de flexibele splitterplaat te begrijpen. Verschillende situatiesvan de beweging van de splitterplaatworden in beeld gebracht en geïdentificeerd op basis van de amplitude en de coherentie in orthogonalerichting ten opzichte vande stromingsrichting, namelijk: lage oscillaties, resonantie, chaotisch en bi-stabiel. Twee situaties, resonantie en chaotisch, zijngeanalyseerd met behulp van de Proper Orthogonal Decomposition om de meest dominante modeste identificeren en om te vergelijken met een cilinderconfiguratie zonder splitterplaat. Voor

elkesituatieworden verschillende koppelingsmechanismen herkend. De beweging van de constructiebij resonantie werd aangedreven door de dominante kenmerken van de stroming, die zich gedroeg als een eenrichtingskanaal. Omgekeerd vertoonde de chaotische situatieeen 2-weg koppeling tussen stroming en constructie.

Optische methoden op basis van stromingstracersbieden een verhoogde lokale nauwkeurigheid door het elimineren van onnauwkeurigheden die anders geïntroduceerd worden door het gebruik van "interrogation-windows" in kruiscorrelatietechnieken. De verbeterdeprestatiesgaanten kostenvan ruimtelijk schaarsemanier waarop data verkregen wordt. Ietswat kritisch kan zijnin aëro-elastische situaties waarineen precieze grensbepaling van destroming-constructieovergangcruciaal is om Collar's triangle te sluiten. Het laatste deel van dit proefschrift is gewijd aan fysica-gebaseerde data-assimilatie om de ruimtelijke resolutie van stromingsmetingente verhogen in verschillende situaties.Ten eerste vooralgemene stromingsdomeinen door gebruik te maken van temporele informatie van de stromingstracersen ten tweede voormetingen inde nabije omgeving van niet-uniforme object oppervlakken. Time-Segment Assimilation (TSA) is een techniek die gegevens verdeeld over een eindig tijdssegment gebruiktom de optimale 3D vorticiteits- en snelheidsvelden beschreven binnen zo'n segment te reconstrueren. Het principe wordt gepresenteerd door drie belangrijke gegevensreductiesituatieste identificeren, die worden geverifieerd met behulp vannumerieke analyse. De numerieke resultaten bestaan uitsynthetische 3D stromingsvelden van sinusoïden entonenhet potentieel van het gebruik van lange tijdsegmenten wanneer de concentratie van stromingstracers laag is. De techniek wordt verder getestmet een experimentele dataset van een cilinderzog. De VIC-TSA-analyse onthult een optimale "track time length"die langer is dan de theoretisch voorspelde. De topologieanalyse van de vortexstructuur inhet cilinderkielzog bevestigt de toename in ruimtelijke resolutie door substructuren te detecteren op een schaal die vergelijkbaar is met de gemiddelde afstand tussen de stromingstracers.

Aan de andere kant worden er twee benaderingen voorgesteld die gebaseerd zijn op numeriekestroming-constructie interactie methodenom vervormbare oppervlaktes te behandelen die binnendringen in het vloeistofdomein door de bestaande VIC+ techniek aan te passen. De Arbitrair-Lagrangiaans-Euleriaanse VIC+ methode, ALE-VIC+, bevat een meshvervormingsstap om het vloeistofdomein aan te passen aan de oppervlakte eenobject. Omgekeerd maakt ImVIC+ gebruik van een "immersed boundary" formulatie zonder het meshte vervormen, waardoor het profiteert van FFT-gebaseerde Poisson solvers voor drukevaluatie. De voorgestelde benaderingen worden beoordeeld aan de hand van een numerieke test met stroming over periodieke heuvels, waarbij een hogere nauwkeurigheid wordt bereikt dan met de referentie VIC+ dicht bij de wanden. Een experimentele analyse, met een turbulente grenslaag in interactie met een onregelmatigbewegend elastisch paneel, toont een nauwkeurige berekening van de drukverdeling over het oppervlak met de voorgestelde technieken.

1

INTRODUCTION

Some fear flutter because they do not understand it.
And some fear it because they do.

Theodore von Karman

This first chapter serves to establish the background for the content of the dissertation. The introduction starts with the concept of aeroelasticity with a historical example. Some interesting, yet critical, aeroelastic phenomena will be described to understand the relevance of the field to prevent catastrophic events. The connection between fluid-structure interaction and aeroelasticity is understood with the concept of Collar's triangle, which will be relevant for chapter 4. The current state of approaches to deal with computational and experimental aeroelasticity shows the challenges to overcome. The final sections include a short review about cylinder flow and the effect of splitter plates that might be useful for chapters 4 and 5.

1.1. Aeroelasticity: a complex field

Washington, USA, 1940. A recently constructed bridge connecting the Kitsap Peninsula to the Tacoma city collapsed with the morning winds the 7th of November. It was the now famous "Tacoma Narrows Bridge", or *Galloping Gertie*, as it was nicknamed by the construction workers, who suffered the vertical movement of the deck during windy conditions. And no matter how much effort was devoted by engineers to damp the odd motions of the local attraction after its inauguration, the bridge was prone to aeroelastic flutter. Historically, the Tacoma Narrows bridge collapse has been ascribed to structural resonance, i.e. vibration from the excitation of a natural frequency. However, the phenomenon was somehow more complex, and did not involve only the structural characteristics of the bridge, but also its aerodynamics.
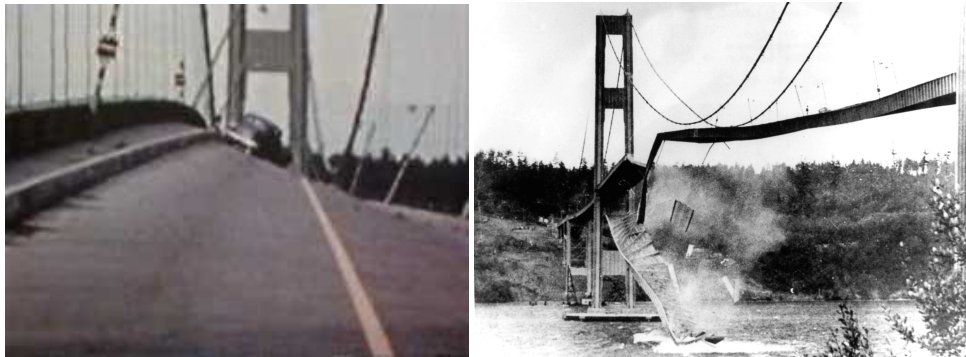
Figure 1.1: Tacoma Narrows Bridge: under strong oscillations (left) and during collapse (right).

Nowadays aeroelasticity its a matter of study by itself and belongs to the main focus of many international research groups. The dynamic interaction between structures, typically with a certain degree of flexibility, and a flow is relevant to many fields: bridges (Scanlan, 1978), air transport (BHATIA and Wertheimer, 1993), wind energy (Hansen, 2007), micro air vehicles (Ifju et al., 2002), and even within our bodies (Bodnár, Galdi, and Nečasová, 2014). Despite the previous examples dealing with low-speed flow regimes, aeroelasticity phenomena become particularly dangerous in the compressible flow regime for high-speed flight, such as in civil aviation (Gao and Zhang, 2020), military vehicles (Kuipers et al., 2007) and space launchers (Carrera and Zappino, 2014).

Even though aeroelasticity in aviation has always been relevant, it has become more significant with the adoption of lightweight structures, with increased degree of flexibility, such as composite materials. An example is illustrated in Fig. 1.3 with the evolution of the latter in civil aviation throughout the last 50 years.

The aim in air transport over the last decades has been focused on reducing operational costs, thus making it cheaper and more accessible to the general users. The most straightforward way to achieve such cost reduction is reducing weight, e.g. structural. The reduction also involves decreasing the fuel consumed, since there is less energy required to move that extra mass around. In addition, international regulations are focusing on reducing combustion emissions, and so fuel burnt, for sustainability, forcing the

Figure 1.2: Systems undergoing aeroelastic deformations. From small and light (micro-air-vehicles and lightweight aircraft) to larger ones (wind turbines and suspended bridges).

industry to evolve towards lighter structures at an accelerated pace.

In this context, progress has been made in the last decades to find new materials, such as composite, more efficient in withstanding loads in specific directions than the established aeronautic choice, metal alloys. In that regard, the discovery of new materials has not aided the aeroelasticity problem. A lighter structure, with less weight and higher flexibility, is prone to oscillate with a higher amplitude at relatively higher frequency, which makes it more prone to couple with the time-scales of the unsteady flow (introduced, for instance by flow separation, wind gusts or induced by vortices).

Nonetheless, the paradigm of structural integrity also changed with the adoption of these highly flexible structures. This is an essential topic for engineers for two main reasons. First, the interaction can lead to static or dynamic instabilities which can result in failure of the structure, either by exceeding the maximum strength of the material or by structural fatigue. A more detailed description of these instabilities is provided in the following sections. Secondly, the behaviour of flexible structures is not yet fully predicted by models as applied in industrial approaches, such as the classical decoupling of structural and aerodynamic computations in aeroelastic simulations, or even state-of-the-art algorithms. The main reason behind this lack of understanding is that simple linear models cannot be applied for flexible structures due to the large deformations of the latter. Despite the fact that numerical aeroelasticity is outside of the scope of this thesis, some words will be said about its challenges in the coming sections to understand

Figure 1.3: Evolution of composite materials in aviation. Figure adapted from *Composite World*: Http://www.compositesworld.com/blog/2014.

the need of experimental work in such field.

1.1.1. COLLAR'S TRIANGLE OF AEROELASTICITY
Aeroelasticity studies the behaviour and stability of systems composed of a structure and a fluid stream subject to the combined effect of aerodynamic forces, and the structure inertia and elastic behaviour (Bisplinghoff and Ashley, 2013). The physical phenomena occurring in such systems are commonly referred to as fluid-structure interaction (FSI). Other forces may act on such systems, such as the gravitational force, which contribute to the total stiffness of the system, but they are relatively unimportant in aeronautics and can be excluded from the aeroelasticity problem [1]. The three relevant forces and their interactions can be graphically related by the Collar triangle of forces (Collar, 1946), shown in Figure 1.4. The former are located at the vertices of the triangle: *A* for aerodynamics, *E* for elastics, and *I* for inertia. Such configuration leaves a space with four regions, the inner area of the triangle, and the three sectors away from the sides. The latter can be called static aeroelasticity, mechanical vibrations, and rigid-body aerodynamics. The subjects within the domain of aeroelasticity can be classified by linking them to the appropriate forces and locating them at the right zone. When the latter phenomena are related to the three forces, they are placed inside the triangle and are said to be a dynamic aeroelastic problem, e.g. flutter.

1.1.2. AEROELASTIC PHENOMENA
The interaction of the Collar forces on the aeroelastic systems can lead to several types of instabilities, always detrimental to the aerodynamic performance and often catastrophic for the structure. These instabilities are broadly classified into *static* and *dynamic*. Static aeroelasticity studies the interaction of elastic and aerodynamic forces. Inertial forces do not play a role since mass properties are not significant. Two clear examples are di-

---

[1]In civil engineering, bridges, power lines and alike, gravity remains an important factor and it affects the system behaviour.
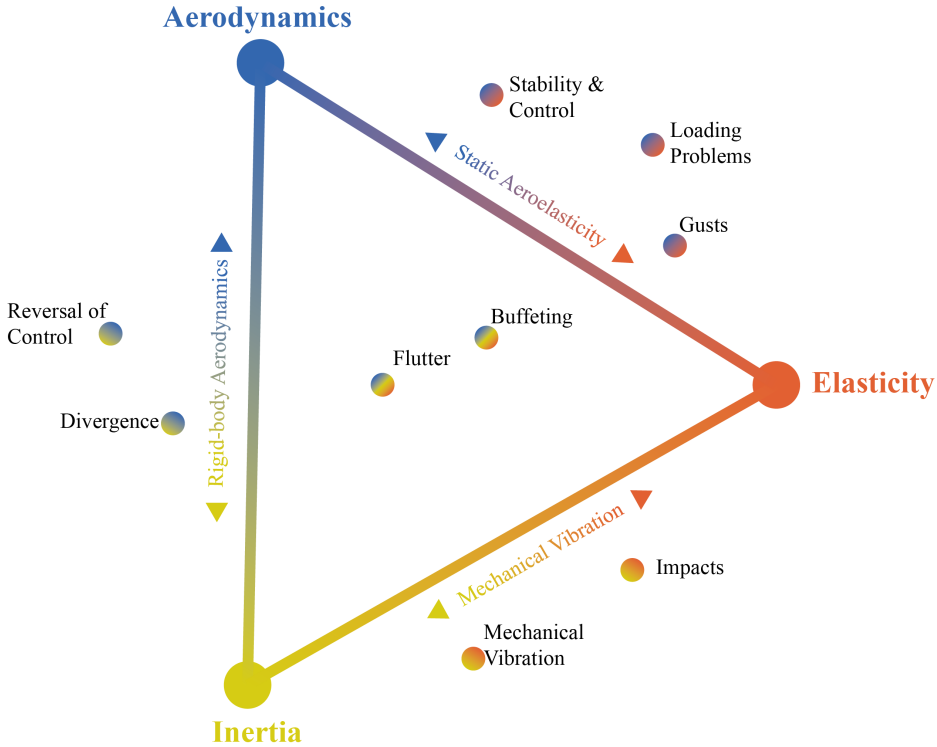
Figure 1.4: The Triangle of Forces and problems akin to aeroelasticity. Figure adapted from Collar (1946).

vergence and control surface reversal. Divergence deals with feedback loop between surface deflection and lift. As a lifting surface deflects under the aerodynamic load, the latter increases due to the higher angle of attack. This process brings the structure to its limit loads and can cause failure unless disrupted or counteracted. Control reversal consists of the loss of the response from the control surface of the aircraft. This is mostly due to the structural deformation of the lifting surface and can cause the control surface to create the opposite effect to the desired (reversal).

As illustrated in Collar's triangle, the full interaction of the forces is referred to as dynamic aeroelasticity. The latter is mostly related to dynamic responses of the structure, such as flutter and buffeting, as a consequence of external disturbances.

Flutter is one of the most general and most complex aeroelastic instabilities. It is an unstable self-starting vibration that occurs when a lifting surface (or deforming structure) extracts energy from the air-stream. Classical examples of flutter are the 'plunging and pitching airfoil' or the aileron flutter (illustrated in Fig. 1.5). The latter example considers an airfoil with a free aileron having the center of mass downstream of the hinge connection. When the configuration encounters a disturbance in the flow that reduces lift momentarily, the airfoil would follow a downward movement. Due to the inertia of
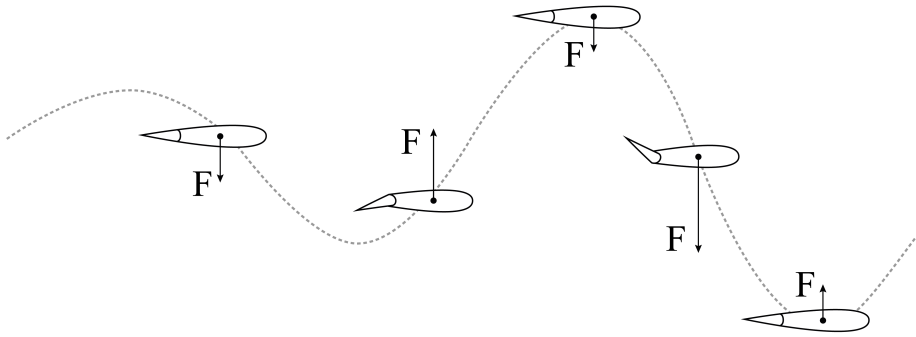
Figure 1.5: Effect of flutter on the free-aileron: an airfoil with a freely moving aileron immersed in a fluid stream, once subject to a vertical motion may dangerously amplify such oscillations.

the aileron, it will deflect upwards, shaping the airfoil to have a downward aerodynamic force. Note that the displacement of the airfoil and the force have the same direction, which means that the airfoil will extract energy from the flow in every cycle. This way, the cyclic motion will grow and eventually the stored energy will overcome the structural strength, i.e the wing will break.

In essence, flutter is the coalescence of the frequency of two structural modes making them easily excited with a redundant disturbance, since one of the latter becomes unstable. Therefore it is a highly non-linear behaviour that does not require any external periodic forcing. There are many types of flutter that affect many different components. The classical focus was on wing flutter, but as systems and material engineering advanced other types became relevant such as panel flutter, engine whirl flutter, etc (Dowell et al., 2021; Bisplinghoff and Ashley, 2013).

On the other hand, buffeting (Liepmann, 1952) is regarded as a high-frequency instability caused by a oscillatory separated wake or shock-wave impinging on a structure and forcing unsteady vibrations (Dowell et al., 2021; Bisplinghoff and Ashley, 2013).

1.1.3. Challenges in fluid-structure interaction
Most of of the mentioned phenomena are undesired for the their consequences, i.e. vibrations, decreased controllability, fatigue, structural failure, noise, etc; thus, one must first understand them, in order to predict and design for them. Generally, experiments serve as a controlled environment where real scenarios are reproduced, serving to the understanding and prediction processes. High-fidelity simulations, often computationally intensive due to the systems complexity, may also provide insights but they must be validated and verified with experimental studies or previously validated computations.

The prediction of aeroelastic regimes relies upon models based on the mathematical description of the systems. The latter can be feasibly obtained only for rather simplified configurations. Instead, the treatment of more realistic systems requires the use of computational fluid dynamics (CFD) coupled with numerical structural analysis (Lee, Price, and Wong, 1999). Yet, the complexity of such systems and the uncertainties related to

the model assumptions, make experimental validation play a pivotal role (Schuster, Liu, and Huttsell, 2003).

The most common approach towards computational aeroelasticity (Bisplinghoff and Ashley, 2013) is the physical separation of structural models and the aerodynamics model. Briefly, structural models conform a mathematical reduced-order model of the system, e.g. the aircraft, as a series of masses connected by springs and dampers which are tuned to represent the dynamic characteristics of the aircraft structure. These masses and springs constitute the stiffness and mass matrices (Fig. 1.6), which are used for simplified aeroelastic analyses coupling them with the aerodynamics modeling in an iterative fashion. An advantage of this separation strategy is the use of specific solvers for each of the models, structural and flow, which allows for individual optimization of the processes. However, an added complexity is the interphase between the solvers and geometries, where extra effort must be devoted to tackle the coupling.
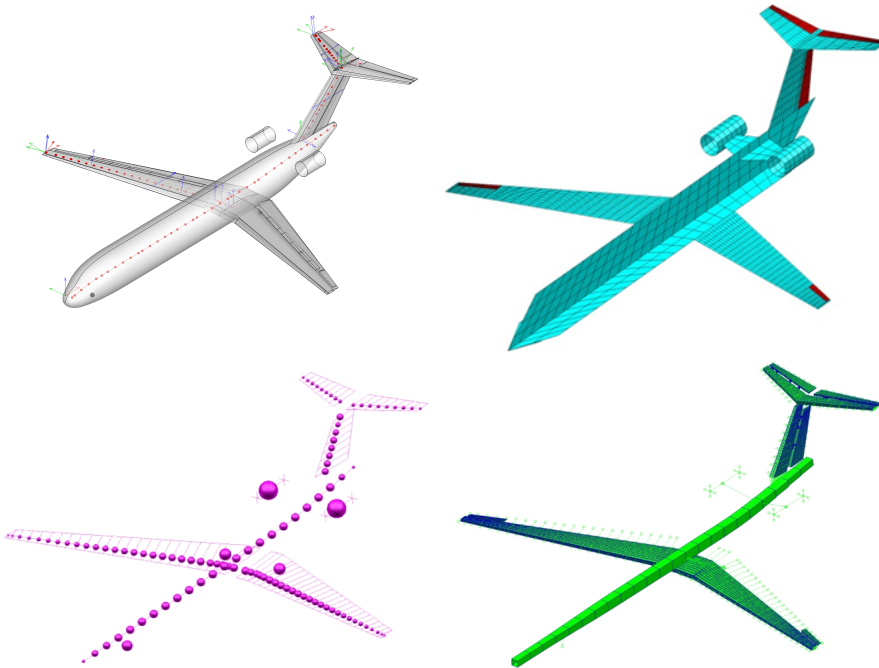
Figure 1.6: The aeroelastic model for an aircraft involves its geometry (top-left), the aerodynamically active surfaces (top-right), lumped mass distribution (bottom-left) and stiffness distribution (bottom-right). Adapted from Klimmek (2009).

On the other hand, the FSI problem can be formulated as a single model, aka monolithic approach, and resolved by simultaneously solving fluid and solid dynamics at once, achieving full coupling of forces and displacements at the interfase. The main drawbacks of this method is the computational complexity and the lack of flexibility, and since this costly model is case-dependant, effort is typically focused towards more versatile approaches. Since typically the latter strategy is not followed and the fluid-structure in-

teraction problem is not fully coupled, the prediction of some non-linear phenomena is one of the most challenging aspects of Computer Aided Engineering (CAE) (Dowell, Edwards, and Strganac, 2003).

Similarly to the challenges of CAE, experimental aeroelasticity is no different. There are various tests depending on the aim (Fig. 1.7), such as wind tunnel testing, ground vibration testing (GVT, Peeters et al., 2009), and flight flutter testing (FFT, Kehoe, 1995). Each of them require of specific equipment, and building models and equipment can be very expensive. Thus, inevitably, the first obstacle one encounters is the cost, in terms of time, money, resources, etc. Moreover, similarly to the computational approaches, some corrections are needed when using intrusive equipment for measurements or when the exact conditions cannot be achieved (Xu and Kwok, 1993).

Figure 1.7: Wind tunnel tests (top-right), ground vibration test (top-left) and flight flutter test (bottom).

Wind tunnels tests are based upon reproducing controlled flow conditions, e.g. free-stream speed, on a model that is, in most cases, a reduced size version of the real system to study. However, in order to reflect the same physical phenomena with the smaller model, some conditions may need to be scaled (Bushnell, 2006). In aeroelastic research, this scaling must include the ratios of aerodynamic, inertia and elastic forces, respectively. Inertia scales with the volume of the system, aerodynamics, with its surface, and the elasticity, often solely on its length. Therefore a scaled-down experiment tends to overestimate elastic forces with respect to the inertia and even more the effect of the aerodynamics. In most cases, it is a challenge to achieve such scaling because matching configurations would require the use of exotic solutions such as very heavy metals (lead and gold) or heavy gases (freon), which are very unfeasible to test with. Furthermore, there are very few wind tunnel installations that cater for aeroelastic tests.

The ground vibration tests aim to measure the structural modes, which are defined by their frequency and their mode shape). The output serves to validate the computa-

tional models of stiffness and mass of the aircraft. GVT can be performed on components or on the entire system, but in both cases the model must be installed with excitation equipment, such as electromechanical exciters, and measurement equipment to quantify the response, such as array of accelerometers (Göge et al., 2007).

On the other hand, FFT is performed during in-flight conditions and aims prove that the flight envelop (plus a 20% extra margin) is flutter free. It measures mode frequencies and damping trends to validate models, including the aerodynamics. Safety and model integrity must be considered too, since the most critical aeroelastic phenomena have a diverging route for displacement, acceleration and deformation, thus of destructive nature. However in most of the cases these FFT to measure and predict flutter are carried out in different phases to demonstrate a flutter-free envelope (Kehoe, 1995; Dimitriadis and Cooper, 2001).

Needless to say, all the challenges associated with the uncertainty quantification in aeroelasticity (Pettit, 2004) are also relevant for aeroelastic studies, both experimental and numerical. The main reasons for the former are complex experimental setups neeed to measure distinct quantities (flow velocity and pressure, surface strain and stress); and for the later, the reduced applicability of analytical methods to real situations and the fidelity of the sophisticated computational models.

1.1.4. EUROPEAN CONSORTIUM HOMER

Wherever challenges exist, there are groups of motivated engineers devoted to overcome them (see Fig. 1.8). Given the need of advancing on experimental techniques for aeroelasticity, a group of European institutions, experts in optical techniques for aerodynamics, such as Particle Image Velocimetry (PIV) and Particle Tracking Velocimetry (PTV), started a collaborative consortium, whom they called **HOMER**, standing for *Holistic Optical Metrology for Aero-Elastic Research*. *HOMER* aimed, and succeeded, at deploying and further develop state-of-the-art non-intrusive experimental flow diagnostic methods to include and combine both aerodynamic and aeroelastic analyses.

Figure 1.8: Kick-off meeting of HOMER consortium in Gottingen, Sept. 2018.

1

As the reader may already have noticed, the work carried for this dissertation was supported by the consortium, and the current objectives are in line with those of the European project.

1.2. SELF-INDUCED VIBRATIONS

Aeroelastic phenomena experienced in aerospace and wind energy systems are the result of a complex structure interacting with unsteady 3D flows (Bisplinghoff and Ashley, 2013). One thing in common to such systems is the interaction of a fluid stream with a highly flexible object. A specific condition is given by a periodic forcing, which can be generated by periodic vortex shedding. The cylinder-foil system exemplifies such condition and has been frequently investigated to advance computer simulations and experimental methods in the field of aeroelasticity where systems exhibit a high degree of flexibility and large displacements. Furthermore, the configuration is relevant for novel energy extraction systems (Allen and Smits, 2001,Hamlehdar, Kasaeian, and Safaei, 2019), devoted to produce electricity from the deformations of the flexible plate with ocean currents. The following paragraphs will settle the basic background for cylinder flow, self-induced vibrations and some works about the cylinder-plate configuration.

1.2.1. CYLINDER FLOW

The vortex shedding off a bluff body has been of interest for the scientific community due to extensive real-life applications (King, 1977). Bluff body wakes are complex and involve shear layer interactions, which result in a vortex street causing strong velocity fluctuations, see Fig. 1.12-a. As a result, transverse flow may result in structural vibrations (Williamson, 1996). Besides the vibrations, the periodic vortex shedding also creates large pressure fluctuations that produce noise and increased drag.

The phenomenon of vortex shedding is characterized by the Strouhal number, a nondimensional number that relates the frequency of shedding to the free-stream velocity and the diameter of the cylinder. The shedding and its frequency is closely related to the formation region or length (Gerrard, 1966). The formation length is the region behind the circular cylinder which does not experience the transverse velocity fluctuations of the vortex shedding as it is upstream of its formation (Bloor, 1964). When the formation region shortens, the frequency of shedding increases due to the interaction of the shear layers that are brought closer to each other (Roshko, 1954).

Flow-induced vibrations(FIV) are a complex phenomenon, in most cases undesirable, where the periodic vortex shedding cause structural vibrations (Chen, 1985). Some examples of these forced vibrations are Vortex-induced vibrations (VIV), buffeting at low speeds and galloping at high speeds. The force exerted from the flow to the cylinder under FIV may cause transverse oscillations of the structure at a frequency similar to that of the flow. The coupling may result in the following effects: (a) increase the vortex strength, (b) increase drag, (c) increase the spanwise correlation, (d) create resonance. The increase of spanwise correlation, also called lock-in state, may lead to larger amplitude transverse oscillations. During the latter, the structure may extract energy from the flow and can be destructive, either by ultimate load failure or fatigue (Blevins, 1977).

Control and suppression of FIV has been researched through active (external energy
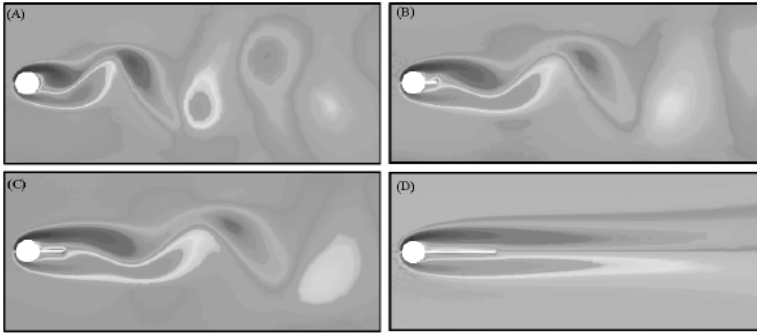
Figure 1.9: Effect length of splitter plate on cylinder wake; (a) no plate, (b) L = 0.5 D, (c) L = D ,and (d) L = 3 D. Figure adapted from Razavi, Farhangmehr, and Barar (2008).

input) and passive (no energy input, Igbalajobi et al., 2013) strategies. Ultimately, the passive approaches involve introducing a solid body of some shape into the wake, such as a splitter plates, rods, base bleeds, roughness, and helical strakes , which are recurrent configurations for flow control (Cardell, 1993).

In particular, splitter plates are two-dimensional surfaces mounted on the cylinder centerline parallel to the flow (Igbalajobi et al., 2013). They come in various shapes and sizes (see Fig 1.12), but they can be broadly classified based on how they respond to the pressure fluctuations in the wake: rigid, permeable and flexible.
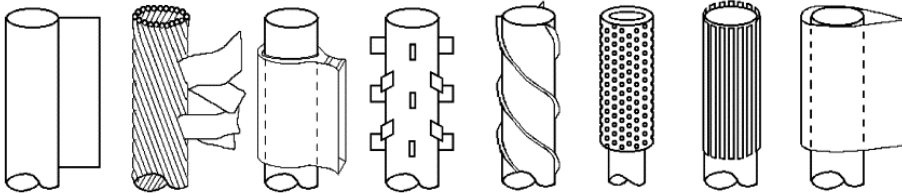
Figure 1.10: Passive vortex suppressors attached to a cylinder. Figure adapted from Blevins (1977).

A rigid splitter plate is not deformed by the flow and does not allow any communication between the shear layers across it. An intermediate step between the permeable and the rigid is the hinged rigid splitter plate, which is free to oscillate with the flow without local deformations (Cimbala and Leon, 1996). The hinged splitter plate was found useful as suppresor of vortex-induced vibrations, acting as a longer rigid splitter plate (Assi, Bearman, and Tognarelli, 2014). The permeable splitter plate interferes partially the communication between the shear layers (Cardell, 1993). Similarly to the hinged plates, permeable splitter plates aid with the galloping response of circular cylinders (Assi and Bearman, 2015).

Flexible splitter plate are made up of flexible materials (relative to the flow loading) and can deform locally at any point. Thus, pressure fluctuations from the vortices shed cause vibrations along the length of the plate. Even though this effect was first re-

1

searched for vortex modulation, one of the most relevant applications is energy harvesting by installing piezoelectric materials in the flexible structure (Allen and Smits, 2001; Taylor et al., 2001). The vibration amplitude of the plate, and so the energy potential, would be characterized by the unsteady loading caused by the vortex shedding. In contrast, the plate oscillation frequency is a combination of the vortex shedding frequency and the naturally occurring frequency of the flexible plate (Lee and You, 2013). On one hand, the cylinder shedding frequency depends on the flow Reynolds number and the cylinder size. On the other hand, the natural frequency of the plate depends on its mechanical properties, such as Young's modulus, and geometric setting, such as the length (Lee and You, 2013). However, to predict the oscillation frequency, it is important to understand the full aeroelastic interaction, where the damping of the structure also has a relevant role for the determination of the frequency.

1.2.2. CYLINDER WITH FLEXIBLE SPLITTER PLATE

The wake flow dynamics of a cylinder with a flexible splitter plate has been the subject of several investigations due to its relevance for a wide range of applications. Those include passive flow control (Sharma and Dutta, 2020) in aeronautics, stability control of plates in nuclear engineering (Guo and Païdoussis, 2000), drag reductions strategies (Apelt, West, and Szewczyk, 1973), and energy extraction with piezoelectric membranes (Allen and Smits, 2001), among others. Moreover, the cylinder-panel configuration is a convenient test case to tackle the challenges associated with the complexity of the fluid-structure interaction problem, for both laminar (Hübner, Walhorn, and Dinkler, 2004; Turek and Hron, 2006) and turbulent flow conditions (De Nayer and Breuer, 2014).
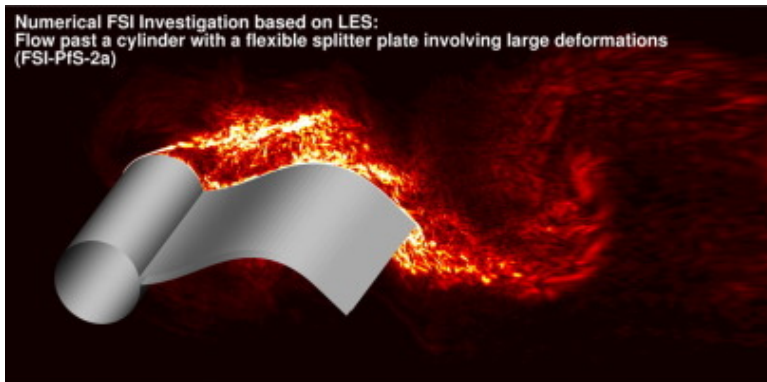
Figure 1.11: Image with cylinder foil configuration. Numerical benchmark used in De Nayer et al. (2014) and De Nayer and Breuer (2014).

Most of the studies on the abovementioned configuration have been carried out numerically by computational aeroelasticity, which usually focuses on the two dimensional coupling problem due to the challenges associated to three-dimensional aeroelasticity (Lee and You, 2013; Abdi, Hosseini, and Podhaisky, 2019; Pfister and Marquet, 2020). On the other hand, experimental studies have focused on the validation of numerical approaches rather than on the characterisation of the dynamics of the fluid-structure

interaction (Fujarra et al., 2001). In addition, experimental works have been limited to structural deformation visualizations alone (Shukla, Govardhan, and Arakeri, 2013) or combined with 2D flow measurements. De Nayer et al., 2014 performed an experimental validation of a cylinder-plate configuration test case using a laser sensor for the panel displacement and two-dimensional PIV for the flow around it.
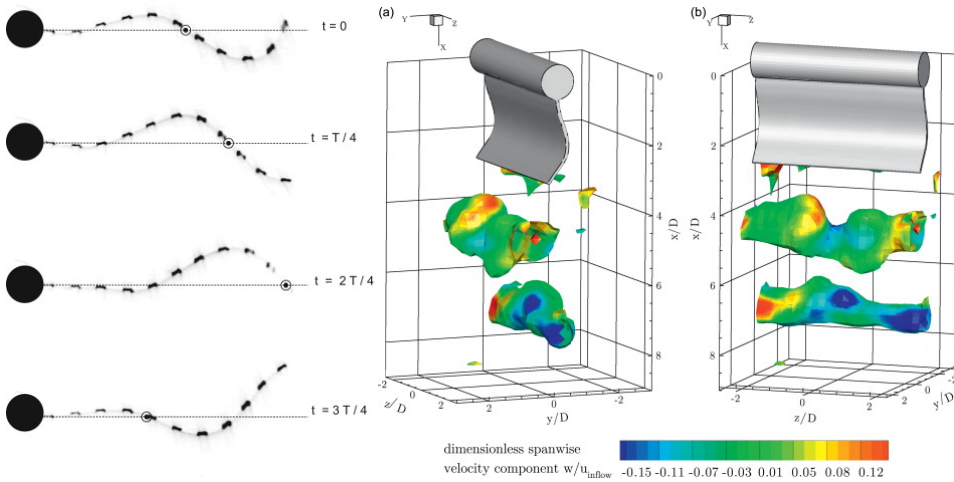
Figure 1.12: Left: time sequence of deformation a fully flexible splitter plate over one oscillation cycle (Shukla, Govardhan, and Arakeri, 2013). Right: spanwise velocity iso-surfaces convecting from the deformed flexible plate (Kalmbach and Breuer, 2013).

In contrast to previous works, Kalmbach and Breuer (Kalmbach and Breuer, 2013) achieved three-dimensional flow measurements by Volumetric Three-component Velocimetry (V3V), a technique for instantaneous volumetric measurement of three dimensional velocity fields, on a flexible para-rubber panel attached to a circular cylinder. The volumetric measurements, which comprised only part of the wake region, were presented by phase-averaging given the periodicity of the phenomenon. Together with the V3V technique, the authors used a multiple-point laser triangulation sensor to measure structural displacements and 2D PIV to measure flow in the overall domain around the model. However, the flow region close to the foil was measured only by 2D PIV; hence, the aerodynamic force estimations were based on the 2D velocity fields, and the structural response of the flexible plate was related mostly to the two-dimensional flow simplification. Also, the authors did not address the effects of the deformation of the flexible structure onto the wake flow features. In this context, three-dimensional flow features of this configuration have been typically disregarded due to the predominant two-dimensional nature of the problem, yet they might affect the performance of the aforementioned applications of flexible splitter plates in cylinders.

1

1.3. OUTLINE

The current chapter has provided the reader with some insight about aeroelasticity and the relevance of this field in various applications. Some of the most important challenges in numerical aeroelasticity have been explored, establishing the need of developing further the computational counterpart, experiments. Chapter 2 describes the measurement technique featuring the experiments gathered in this dissertation. It includes some data reduction techniques such as, statistical approaches to clean the data, and physics-based data assimilation to enhance spatial resolution. An experimental technique assessment for aeroelastic research is provided in Chapter 3. A flexible mechanically-driven panel interacting with a turbulent boundary layer is measured by both DIC and LPT, a correlation-based and tracking technique respectively. Recalling Collar's Triangle from this introduction, Chapter 4 attempts its closure by measuring the three dominant unsteady forces. The latter experiment regards a flexible foil attached to a cylinder, whose fluid-structure interaction is further examined in Chapter 5. In view of some of the experimental challenges encountered, some work was carried out in data assimilation and gathered in chapter 6 and 7. Finally, Chapter 8 concludes the dissertation with a review of the most important findings.

2

LARGE-SCALE PIV FOR AEROELASTIC RESEARCH

Throughout the centuries
there were men who took first steps, down new roads,
armed with nothing but their own vision.

Ayn Rand

To dig deeper in the experimental essence of this dissertation, the state-of-the-art measurement techniques are introduced, for both 3D velocimetry in aerodynamics and for surface loads in solid mechanics. The base for the experimental knowledge within the dissertation is established in this chapter. The latter deepens on the standard tracking technique used through the book by previously establishing in detail the general working principle for PIV. The concept of data assimilation (DA), in particular physics-based DA, is drafted as an approach to transform the Lagrangian description of tracked particles into Eulerian fields of flow velocity. In addition, some data reduction approaches, which will appear in chapters 4-7, are mathematically explained. Among the statistical methods, some insight is given about Proper Orthogonal Decomposition, that serves as reduced order model to find the most energetic features. Finally, one of the challenges in experimental FSI is the measurement of aerodynamic load on deforming surfaces. The chapter will provide with the basis for pressure reconstruction from PIV.

2.1. MEASUREMENT TECHNIQUES

After introducing them in the previous chapter, the relevance of experimental aeroelasticity and the need to overcome its associated challenges are evident. The following chapter introduces the available measurement techniques, which have been typically focused on structural or flow alone. However, it should be kept in mind that these techniques have typically focused either on the flow alone, to measure the flow velocity, pressure and/or aerodynamics loads, or on the structure, to measure the structural deflection, the strain and the elastic loads. Instead, an integrated measurement approach capable of capturing simultaneously the flow and structural behaviour is currently missing.

2.1.1. STRUCTURAL DIAGNOSTICS

Structural diagnostics is a rather broad field where many variables can be of interest depending on the field: aeroelasticity, damage detection, crack propagation, . In aeroelasticity, the focus is mostly in those related to the elastics, so strain or deformations and their spatial derivatives, and inertia, based on displacement and its temporal derivatives (Collar, 1946).

The conventional techniques for structural diagnostics are chosen according to the balance between accuracy, simplicity and cost. They can be classified in contact, e.g. force cells and strain gauges, and non-contact methods, including optical techniques (Sciammarella and Sciammarella, 2012).

Strain gauges are the most common contact methods for the determination of surface strain. They measure the change in length beneath the active measuring area of the gauge. Strain gauges are mostly sensitive to the principal direction, so a configuration with several devices is required to measure complex strain fields. Similar devices for strain measurements are extensiometers. These can be optical but with the drawbacks of measuring the average strain limited to a very small section.
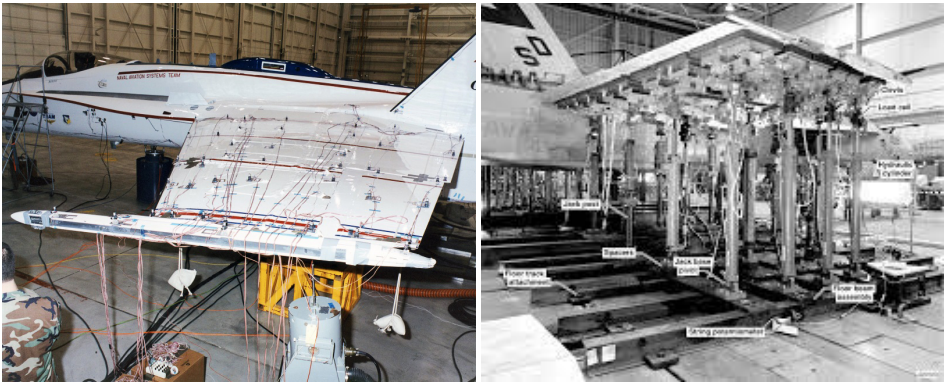

Figure 2.1: Intrusive equipment: accelerometers, strain gages.

To overcome the intrusivity of the contact methods, some optical techniques aimed to measure structural forces without affecting the structural properties. Some of these are interferometry, optical doppler, speckle metrology (Sirohi, 2020), fringe projection

(Sutton et al., 2001) and Moiré techniques (Sciammarella, 1982). Most rely on the projection of light patterns with are imaged and processed to measure displacements. In addition, some methods such as laser sensors are able to perform velocity measurements used in GVT (De Figueiredo et al., 2021).

2.1.2. DIGITAL IMAGE CORRELATION

Digital Image Correlation (DIC) is a non-contact optical measurement technique that is widely used for structural diagnostics, such as crack propagation and material deformation (McCormick and Lord, 2010). After an explosive growth in the last decades, encouraged by the evolution of hardware and digital analysis, DIC is able to measure today 3D surface shape and deformation for a wide range of scales, although it appeared as a two components (2C), in-plane measurement of the surface deformation.

DIC is a full-field measurement technique that can measure the deformation and strain of the entire specimen, rather than just a single point. It is based on characterizing the surface with a locally unique pattern that changes with the deformation. Therefore, the surface is applied with any object-based patterns including lines, grids, dots and random arrays, yet the most common is a speckle pattern (Pan et al., 2009).

The working principle of DIC is based on the comparison of two digital images of a specimen taken before and after deformation. The images are subdivided into windows and correlated at different stages of the deformation to determine the displacement and strain fields (see Fig. 2.2). The full-field shape and deformation of the surface in view allow to calculate the stress and strain distribution in the model (Pan, Yu, and Zhang, 2018). When two or more cameras are used, as in stereoscopic DIC (Wang et al., 2013), the technique is able to measure the out-of-plane component, as in Fig. 2.3.
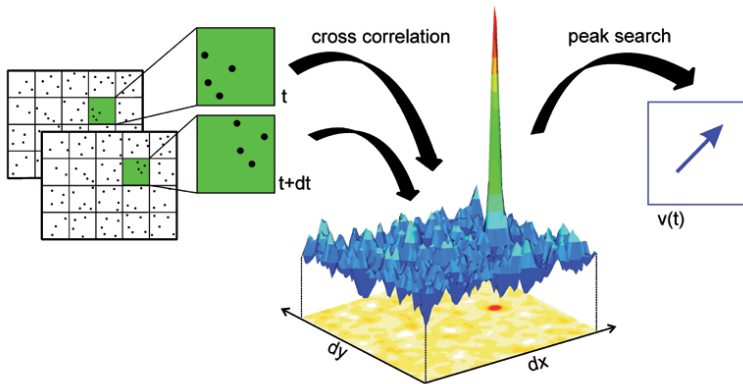
Figure 2.2: Principle for correlation based approaches like DIC or traditional PIV (Wieneke, 2017).

One of the main advantages of DIC is that it is a non-contact technique, which means that it does not require any physical contact with the specimen. This reduces the risk of damage to the specimen and allows for measurements to be taken in harsh environments. DIC has an average measurement uncertainty of about 0.01 to 0.05 pix (Balcaen

et al., 2017). The measurement uncertainty of DIC is affected by several factors, including the resolution of the camera, the quality of the images, the quality of the speckle pattern, and the accuracy of the correlation algorithms.
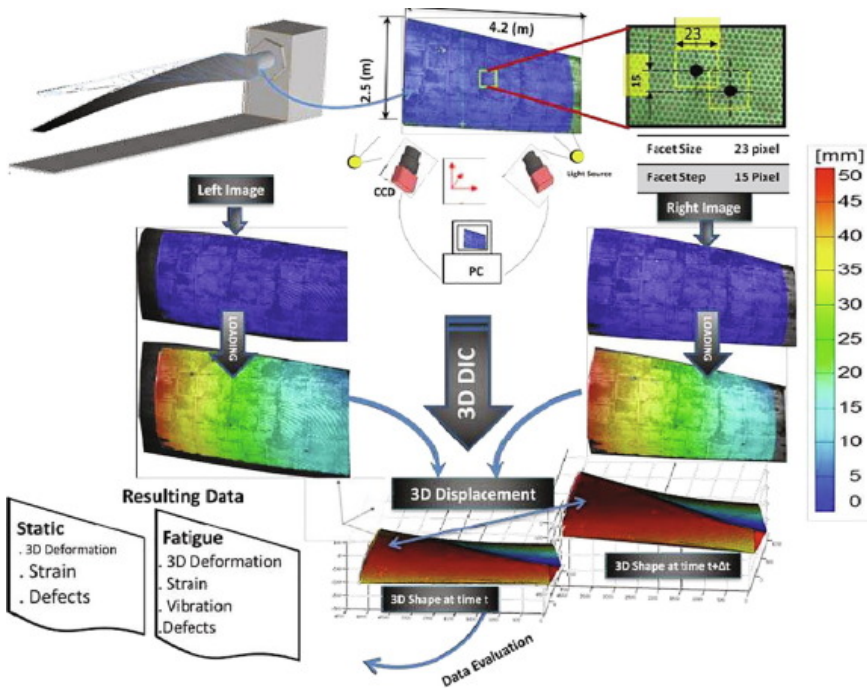
Figure 2.3: Digital Image Correlation technique applied to a large-scale composite structure. Figure adapted from Janeliukstis and Chen (2021).

2.1.3. FLOW DIAGNOSTICS

There are several flow quantities that could be measured in order to fully determine the flow state, such as, velocity, pressure, density, temperature, etc, from which velocity and pressure are the most determinant for FSI problems.

One of the first approaches to determine the direction of the flow was by oil flow visualization. It was limited to the flow direction in close proximity to the surface of an object and was unable to give quantitative measurements. Far away from the surface, smoke lines were able to provide flow streamlines for steady flows. Dyes are used for water flows, as alternative to smoke lines.This technique was upgraded with dyes in order to provide a full 2D map of flow visualization.

A technique to quantitatively measure the flow velocity, yet intrusively, is hot-wire anemometry (HWA). Hot-wire anemometry is a thermal anemometry by which the flow velocity is measured by sensing the changes in temperature, and so the heat exchange, between the flow and a heated sensor. The technique implies a calibration process and needs a complex array to measure 3D flows, i.e. three velocity components.

Regarding direct pressure measurements, the most common device is the Pitot tube,

which consists of a total pressure measurement. It is typically used to infer the free-stream velocity or local flow velocity from the measurements of total and static pressures by means of a combination of Pitot tube and static pressure ports or the pitot tube itself. Similarly to the HWA, a complex configuration with several ports in a single device is able to measure a flow vector in 3D.

The aforementioned techniques are limited by their intrusiveness in the flow, that means that the fluid is perturbed by their existence, involving a limited measurement that needs correction. Even though this error is usually stationary or biased and it might be corrected, non-intrusive diagnostics techniques are preferred.
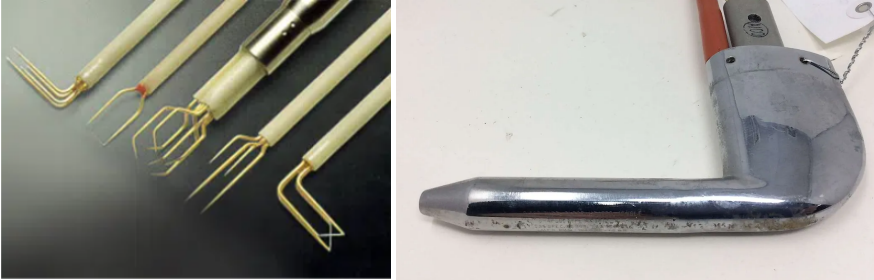
Figure 2.4: Intrusive flow measurement systems: hot-wire anemometry and pitot tube.

Figure 2.5: Generic PIV setup showing the measurement domain, the acquisition camera systems and the illumination system.

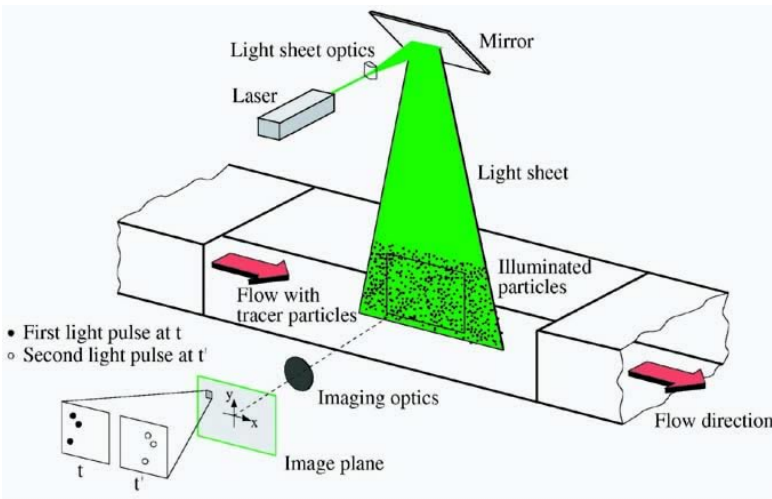Optical techniques in fluid diagnostics have been established as the standard measurement techniques for planar and volumetric flow measurements (Schröder and Willert, 2008). The most popular family of optical approaches is particle image velocimetry(PIV),

which measures velocity vectors in space, in a 2D plane or in a 3D volume. As the name PIV infers, the flow is seeded with particles that follow it. The seeded stream is then illuminated and snapshots are captured by optical sensors or cameras. The process is illustrated in figure 2.5. To extract the velocity fields from the acquired images, there are two main strategies. The classical way, within the short life of PIV, is a correlation based strategy (Fig. 2.2). The acquired images are divided into smaller portions called interrogation windows, which are cross-correlated between image pairs to find average displacements. Velocity vectors can then be calculated by using the average displacements within the windows and the light pulse time separations. Figure 2.6 shows a superposition of the flow tracers captured and the processed velocity vectors for a wing tip vortex (left) and an impinging jet (right). A key advantage of PIV versus other optical techniques, is the capability to measure vorticity or even estimate pressure. Similarly to DIC, the continuing growth in computer technology gave rise to further developments and adaptations of PIV.
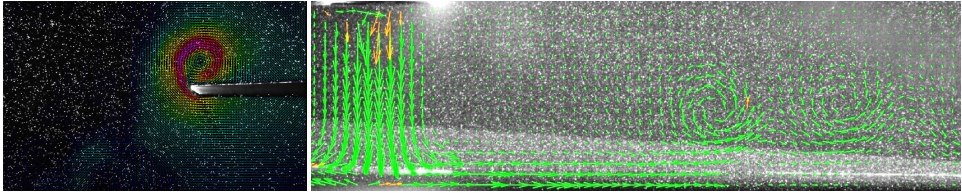
Figure 2.6: Superposition of raw PIV images and the processed velocity vectors. Left: wing tip vortex from Dantec (https://www.dantecdynamics.com). Right: impinging jet from IIT Bombay (https://rnd.iitb.ac.in).

The PIV technique has evolved in the last decades to include either more velocity components or more dimensions, as illustrated in Fig. 2.7. The latter classifies the different PIV approaches according to the velocity components and the dimensions, in both space and time. Despite the relevance of stereoscopic PIV (Arroyo and Greated, 1991) for combined measurements with DIC (Bleischwitz, De Kat, and Ganapathisubramani, 2017; Marimon Giovannetti, 2017; Jacobi and Nila, 2021), an important advancement for FSI measurements has been that of tomographic PIV (Elsinga et al., 2006). TOMO-PIV made use of additional cameras in order to reconstruct flow tracers anywhere in the volume of view.

On the other hand, novel advancements on particle tracking velocimetry (PTV, Malik, Dracos, and Papantoniou, 1993; Maas, Gruen, and Papantoniou, 1993) towards high-density scenarios (Schanz, Gesemann, and Schröder, 2016), has been a recent game-changer approach on the image-velocity step. The PTV technique consists of tracking individual particles in space rather than groups and it is typically aimed for 3D volumes. The most evident advantage is the increased spatial resolution since it is not affected by the detrimental modulation of the cross correlation approaches in interrogation windows (Scarano, 2012, see Fig. 2.9). In addition, given the lower seeding densities, tracking approaches present advantages for large scale measurements (Fig. 2.10 and 2.17). This technique is developed further in the following sections.
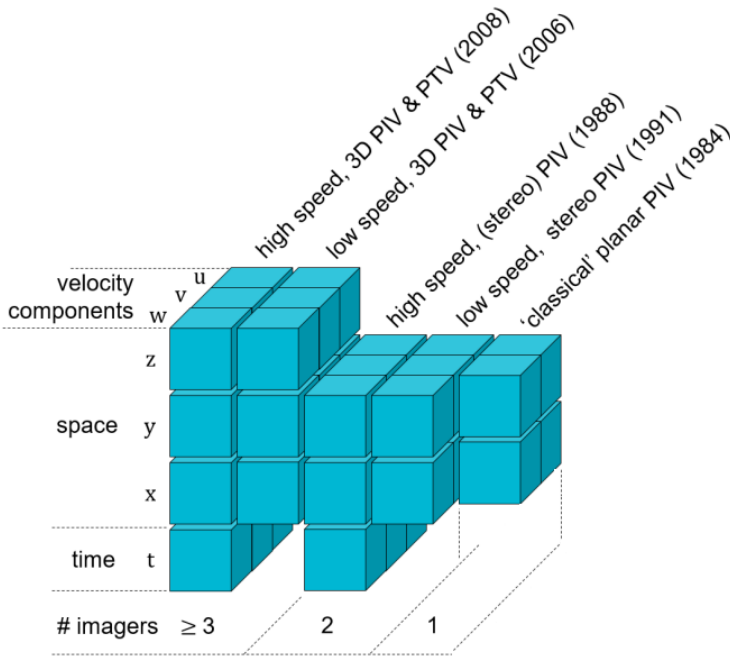
Figure 2.7: PIV systems classified by measurement dimnensionality. Figure adapted from Scarano (2012).

2.1.4. PIV WORKING PRINCIPLE

All PIV approaches are complex techniques consisting on three main components: seeding or tracers, illumination, and imaging, as introduced in Section 2.1.3. The following section will describe the components in more detail with special attention to the large scale capabilities of tracking techniques.

SEEDING

Tracer particles are the basis for PIV experiments. PIV is an indirect flow measurement, since the velocity measurement is not obtained from fluid particles themselves but from external particles seeded into the flow, under the assumption the latter will follow the flow faithfully. Therefore, the choice of the particles is critical to avoid measurement errors. The behavior of particles suspended in a fluid flow is described by the Stokes number. It is defined as the ratio of the characteristic time of a particle to a characteristic time of the flow or obstacle (Brennen, 2005),

$$St_k = \frac{\tau_p U_\infty}{l_c} \tag{2.1}$$

where τ_p is the relaxation time of the particle, U_∞ is the free-stream velocity, and l_c is the characteristic length of the obstacle or flow structure. For a particle to detect the disturbance and follow the underlaying flow streamline, the response should be faster than the smallest time scale of the flow to measure. Therefore, $Stk \ll 1$ is needed for an

2

Figure 2.8: Typical TOMO PIV setups with several cameras. Left: 3-camera setup for jetflow measurements, from Nextflow project: https://erc-nextflow.uc3m.es/the-project/. Right: 4-camera system for water flows measurements, from LaVision : https://www.lavision.de/en/products/flowmaster/tomographic-piv/.
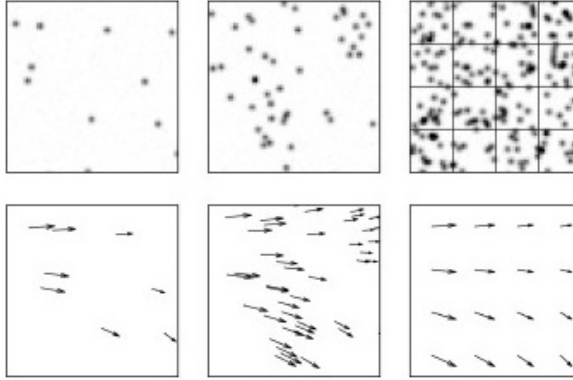
Figure 2.9: Difference in spatial resolution between cross correlation and tracking approaches.

acceptable tracing accuracy. Moreover, flow tracers must be neutrally buoyant, i.e. they must have the same density as the fluid, to minimize the relaxation time:

$$\tau_p = d_p^2 \frac{\rho_p}{18\mu} \tag{2.2}$$

where d_p is the particle diameter, ρ_p is the density of the particle, and μ is the fluid dynamic viscosity.

In addition to the flow tracer fidelity, optical characteristics are critical for a PIV measurement too, in particular light scattering. The latter depends on the particle diameter, the light wavelength and the ratio of refractive indices. Classical PIV in air flows has employed several substances as tracers with a range of sized from 1 to 100 μm. However, the scattering efficiency is lowered at larger measurement volumes thus affecting the spatial resolution (Adrian and Westerweel, 2011). Helium Filled Soap Bubbles (HFSB) appeared as a solution for large domains PIV (Bosbach, Kühn, and Wagner, 2009) thanks to their excellent characteristics when scattering light. While neutrally buoyant, HFSB are larger particles than their counterparts ($d \approx 300 \mu m$) and reflect 10,000 times more light. Re-
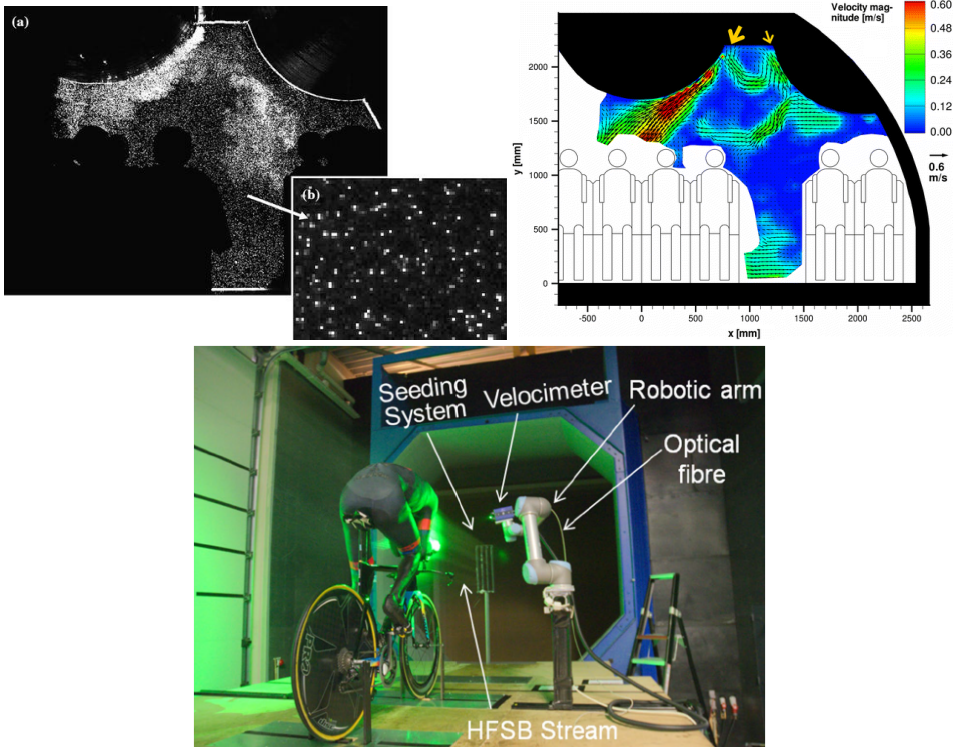
Figure 2.10: Large-scale PTV applications: flow inside aircraft cabin (Kühn, Bosbach, and Wagner, 2009, top) and flow around a cyclist (Jux, Sciacchitano, and Scarano, 2020, bottom).

cent developments in bubble generation at sub-millimeter levels has accelerated the use of HFSB in experiments (Scarano et al., 2015; Huhn et al., 2017). Using sub-millimeter bubbles adds less momentum into the flow, has a higher generation efficiency, higher sensitivity towards small objects in the flow, and lower model contamination. An example of a recent work with a large-scale highly-dense HFSB measurement while keeping a high spatial resolution in shown in Fig. 2.11.

Furthermore, for an accurate PIV measurement, the seeding density should be homogeneous throughout the domain. For that reason, flow tracers are usually introduced in the settling chamber of wind tunnels where the flow velocity is lower and allows for an increased spread of the seeding particles. Finally, there are some additional considerations like safety and contamination that determine the choice for flow tracers. Toxic, hazardous, corrosive or reactive substances are discarded.

ILLUMINATION

Once the flow is seeded with suitable flow tracers, illumination is required in order to capture them with optical diagnosis. The illumination system consists of light sources and light optics to generate an illuminated region of interest. Former PIV techniques rely on observing the particles at two instances differing Δt, which corresponds to the

2
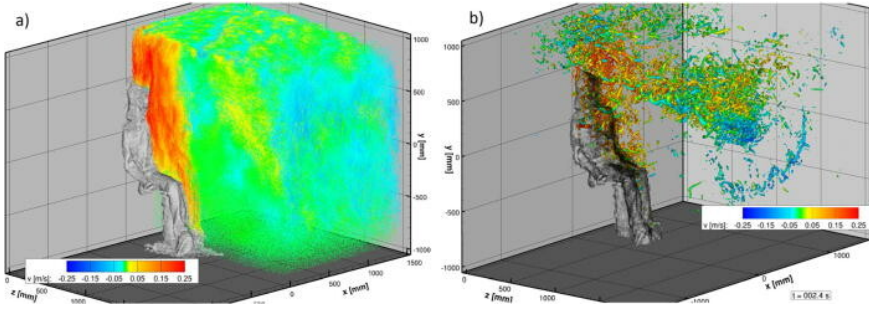
Figure 2.11: Large-scale PTV measurement with HFSB. Domain with flow tracers (left) and Q-criterion (right). Figure adapted from Schröder et al. (2022).

light pulses separation, at a low frequency. Time-resolved PIV measurements are characterized by acquiring images in a continuous manner, i.e. with a constant pulse rate. Still in this fashion, the light pulses width must be short compared to the motion of the particles, as streaks would be captured otherwise. An additional requirement is the light intensity, as enough energy must be scattered by the particles to be measured.

Lasers meet all the requirements for PIV measurements, becoming immensely useful in planar PIV and to some extent, tomographic PIV (Elsinga et al., 2006). Some advantages like emitting monochromatic light of high energy density (Raffel et al., 2018), and the easy manipulation of the light beams to produce thin sheets made lasers the standard illumination technique. A disadvantage is that they are expensive, difficult to use for safety reasons, and operated with a trigger delay (Scarano, 2012).

Under the umbrella of PIV technology, optical technology has grown immensely, but laser technology has stayed relatively the same. This is a particular challenge when dealing with medium and large-scale measurements. Recent developments in light-emitting diodes (LED) technology has made it suitable for PIV illumination (Willert et al., 2010). Both requirements of pulse width and light intensity are satisfied nowadays for applications such as low-speed volumetric measurements. Additionally, LED devices outperform lasers in terms of cost and ease of operation and conform a safer option for the human eye.

IMAGING

The light scattered by the illuminated particles within the measurement domain is captured by electronic image sensors, commonly charged coupled devices (CCD) and complementary metal–oxide–semiconductors (CMOS). The images of the tracers are created on the surface of the sensor by means of a system of lenses. Such system is characterized by some critical parameters such as the focal length, the aperture or f-number (f#), and the magnification factor. The focal length indicates how convergent or divergent the lens is and determines the distance of the camera setup to the model or measurement volume. The focal length is given from the following relation between the distance from the object to the lens, d_{ob}, and the distance from the lens to the image, d_{im}:

$$\frac{1}{f} = \frac{1}{d_{ob}} + \frac{1}{d_{im}} \tag{2.3}$$

The aperture determines the amount of light that passes through the lens into the sensor, and it is controlled by the $f_\#$ number. The latter is not only important for the intensity saturation of the PIV images but also for the depth of field, which is inversely related to the $f_\#$. Finally, the magnification M is the ratio between the image size (sensor size, A_s) and the imaged object size (field of view, FOV):

$$M = \frac{d_{im}}{d_{ob}} \tag{2.4}$$

Even though the previous parameters would determine the imaged particle size, in most conditions, the minimum particle image diameter is limited by diffraction effects. The image density in volumetric PIV, expressed as the number of particles per unit pixel area (ppp), is critical due to the posterior digital image processing algorithms. The latter are limited by a maximum seeding density, PIV to 0.2 ppp (Michaelis et al., 2010) and LPT to 0.125 ppp (Schanz, Gesemann, and Schröder, 2016, Sciacchitano, Leclaire, and Schroeder, 2021).

As for the seeding and illumination, imaging for large-scale PIV has some additional challenges, such as optical access and the focal depth. Large-scale measurements typically regard complex models with small/narrow regions where phenomena easily interact. Since such corners with poor optical access are often the domain of interest to understand the problem, the number of viewing cameras may be increased making the setup more complex. Moreover, the focal depth, defined as the range or depth in which the tracers are in focus, may conflict with light intensity of the particles, both related to the camera aperture. Opening the lens, allows more light into the sensor, but shrinks the volume at which the tracers look sharp. Consequently, large-scale PIV experiments require of additional light sources to overcome the low aperture for long focal depths.

2.2. LAGRANGIAN PARTICLE TRACKING

As introduced before, three-dimensional velocity measurements based on PIV have been transitioning from domain cross-correlation (Tomographic PIV, Elsinga et al., 2006) towards more efficient particle-based analysis techniques, notably Lagrangian Particle Tracking (LPT) and the Shake-the-Box algorithm (STB, Schanz, Gesemann, and Schröder, 2016). Particle Tracking Velocitry (PTV), a term to refer to LPT applied to flows, is a PIV technique in which the individual tracer particles are tracked in three-dimensional volume for several consecutive time instants, such as in Figure 2.12 (Novara and Scarano, 2013).

The main advantages offered by particle tracking velocimetry techniques (Nishino, Kasagi, and Hirata, 1989; Malik, Dracos, and Papantoniou, 1993; Maas, Gruen, and Papantoniou, 1993) are that the velocity is defined pointwise, as opposed to the spatial averaging over the interrogation window. The cross-correlation analysis provides a single vector that accounts for the displacement of the flow in a particular region containing several different particles, thus describing the flow in an Eulerian way. In LPT, individual particles have their own displacement vector, providing a Lagrangian insight into the flow.

A second important advantage of particle-based analysis is the significant level of data compression. With LPT, only the particle positions and their velocity need to be
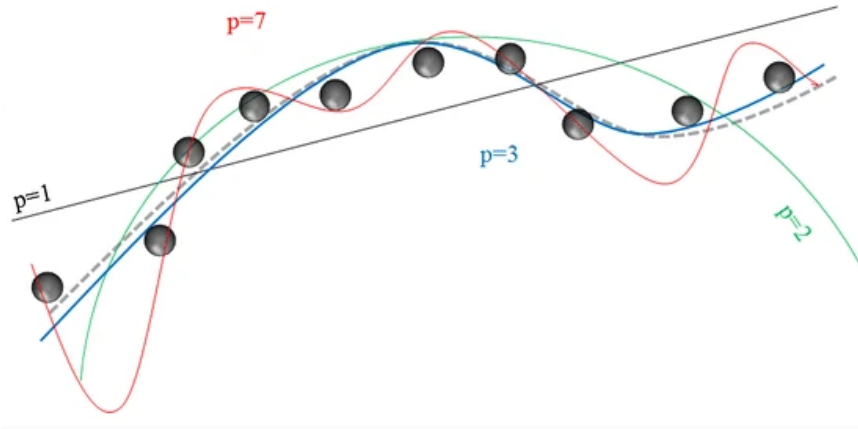
Figure 2.12: Particle-tracking algorithm along consecutive recordings with different trajectory polynomial fits. Figure reproduced from Novara and Scarano (2013).

stored, opposed to reconstructed volumes often counting billions of discrete volumetric elements (voxels), thus reducing measurement processing times.
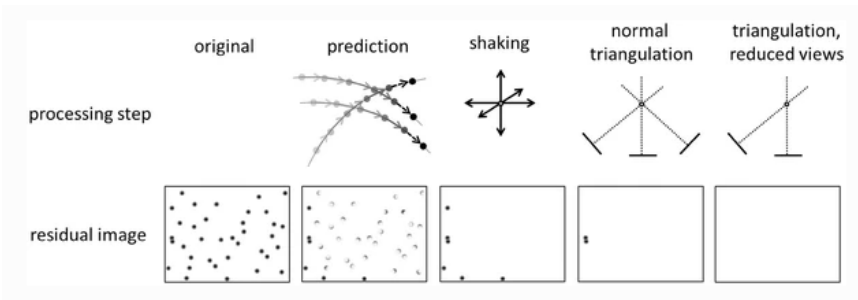
Figure 2.13: Processing strategy for Shake-the-Box: processing steps (top) and remaining image residuals (bottom). Figure reproduced from Schanz, Gesemann, and Schröder (2016).

PTV was born with the work of Maas, Gruen, and Papantoniou (1993), which detailed the hardware equipment needed to perform 3D Particle Tracking Velocimetry and discussed a mathematical model that determines 3D coordinates significantly faster than the previous manual methods. A key development in the field of particle tracking was Shake-the-box (Schanz et al., 2013), a novel tracking method that uses time-resolved data to track particles even in densely seeded flows with benefits in spatial resolution, computational load, and higher robustness to ghost particles. Nevertheless, the method requires of a mapping function, e.g. linear (Bosbach, Kühn, and Wagner, 2009), Gaussian (Elsinga et al., 2006), that relates the reconstructed volume to the camera snapshots. The sophistication of the calibration procedures and the adoption of variable Optical Transfer Functions improved the tracking and reduced the amount of ghost particles, or false

positive particle detection Schanz, Gesemann, and Schröder, 2016. Additionally, the STB methodology is computationally efficient when compared to its counterparts, former 3D-PTV (Virant and Dracos, 1997) or TOMO-PIV (Elsinga et al., 2006). However, one of the widely reported shortcomings of the PTV analysis has been the low reliability in particle image pairing. The latter problem is intrinsic of optical volumetric techniques and grows exponentially with the tracers' concentration (Schanz, Gesemann, and Schröder, 2016), as depicted in Fig. 2.14.
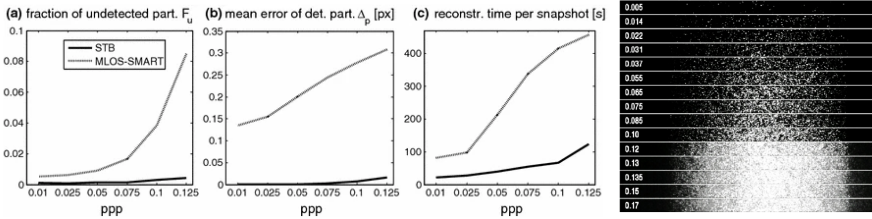
Figure 2.14: Left: effects of seeding concentration on (a) fraction of undetected particles, (b) accuracy in detection, and (c) reconstruction time, for tomographic PIV and STB algorithms (Schanz, Gesemann, and Schröder, 2016). Right: visualization of flow seeding densities for reference (Scarano, 2012).

The introduction of iterative algorithms for 3D particle field reconstruction (IPR, Wieneke, 2012) has paved the way to a more robust particle tracking analysis, i.e. STB predicts the particle distribution of the next time step using time-resolved flow data (Schanz, Gesemann, and Schröder, 2016). As a result, the tractable seeding density for particle-based methods has attained those practised for tomographic PIV (Raffel et al., 2018).

2.3. PHYSICS-BASED DATA ASSIMILATION

One of the main problems arising from the direct treatment of spatially sparse data (e.g. PTV or LPT) is the difficulty in performing a number of data reduction operations, ranging from simple visualizations to statistical analysis, spatial differentiation and evaluating more complex operators such as for pressure evaluation (Van Oudheusden, 2013). Reducing first the data onto a Cartesian grid (Cartesian grid reduction, or CGR in the remainder) is currently the norm.

Several works have aimed at optimising such process in terms of accuracy, reliability, resilience to noise and computational cost. Early works on CGR have proposed interpolation techniques, mostly using a polynomial basis for either interpolation or multidimensional regression. Specific basis functions for PTV data have also been proposed, notably the adaptive Gaussian windowing technique (AGW, Agüí and Jimenez, 1987). The main shortcoming of interpolation techniques is the mismatch between the solutions admitted by the basis functions (especially for low-order polynomials) and those representing the physical flow behaviour. For instance, a linear interpolation of scattered data produces an unphysical discontinuous distribution of the velocity gradient and the related flow properties (vorticity, rate of shear). Methods that enforce the solution to obey physical laws have been initially proposed for PIV data (already on a Cartesian grid) as a mean to reduce the measurement errors. Solenoidal filters that impose

mass conservation (Vedula and Adrian, 2005; Schiavazzi et al., 2014) fall in the above category.
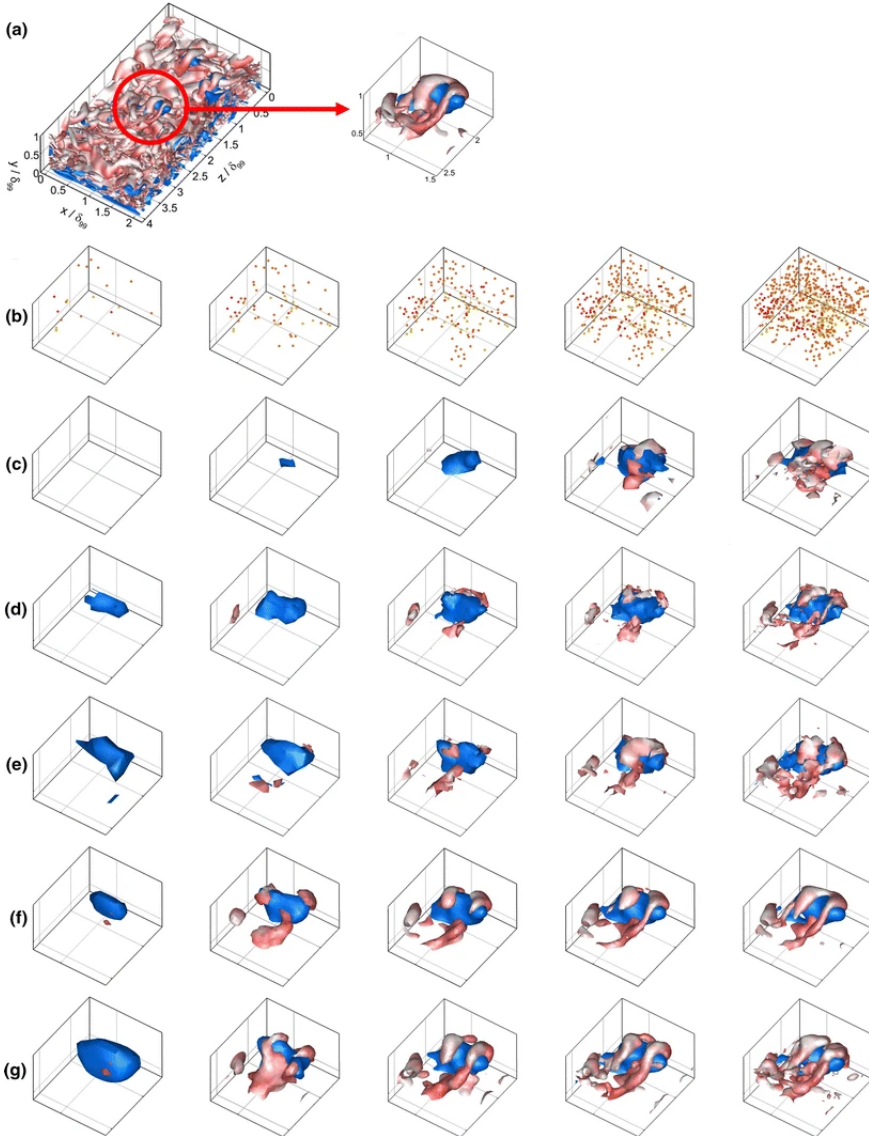
Figure 2.15: Instantaneous sample flow field (a), visualized by isosurfaces of u'/u_∞ (blue) and vorticity magnitude (red). Instantaneous particle distributions at seeding a concentration of (from left to right) 50, 200, 500, 1000 and 2000 particles/δ_{99}^3 (b, particles colored by velocity magnitude). Flow field reconstruction using PIV (c), linear interpolation (d), AGW (e), VIC without Du/Dt (f), and VIC+ (g). Figure from Schneiders and Scarano (2016).

More complex methods based on data assimilation have been introduced for CGR

2

seeking to enhance the spatial resolution. By enforcing compliance of the instantaneous flow measurement (velocity and its material derivative) with the governing equations of fluid motion (conservation of mass and momentum), data assimilation techniques have shown to enable resolving the flow at scales smaller than those attained by interpolation or cross-correlation analysis. The VIC + technique (Schneiders and Scarano, 2016) is based on the assimilation of the data to the dynamical equation of vorticity (Vortex-in-Cell, Christiansen, 1973) and it has shown to provide spatial resolution significantly higher than that of cross-correlation analysis (typically used for tomographic PIV data), as depicted in Fig. 2.15. Physical processes, such as vorticity fluctuations dynamics and turbulent kinetic energy dissipation, taking place at the right-side of the spectrum of flow scales were captured to a fuller extent by the VIC+ data assimilation, compared to the cross-correlation analysis (Schneiders, Scarano, and Elsinga, 2017). Further studies have confirmed the benefits of imposing mass and momentum conservation for CGR applied to particle trajectories measured with the STB technique (FlowFit, Gesemann et al., 2016). Furthermore, the same group (Ehlers, Schröder, and Gesemann, 2020) has investigated ways to improve the temporal consistency of FlowFit CGR by introduction of artificial Lagrangian tracers (virtual particles).

In the work of Jeon et al. (2018) (VIC#), significant advancements to the VIC + technique have been reported, both in terms of computational efficiency (multi-grid computations) and for the treatment of domain boundaries, as shown in experimental assessments (Michaelis and Wieneke, 2019).

In summary, CGR techniques can be qualified by their accuracy and spatial resolution. Figure 2.16 compares such methods, stating the relatively poor resolution and accuracy of spatial averaging methods, compared to interpolators. Further advantages to the latter are obtained with the use of physical constraints as done by data assimilation techniques.

Figure 2.16: Summary of CGR methods and qualitative indication of their performance in terms of measurement accuracy and spatial resolution. Height of the bars purely indicative.

Most of the proposed approaches perform the assimilation on the basis of the instantaneous flow properties (velocity, vorticity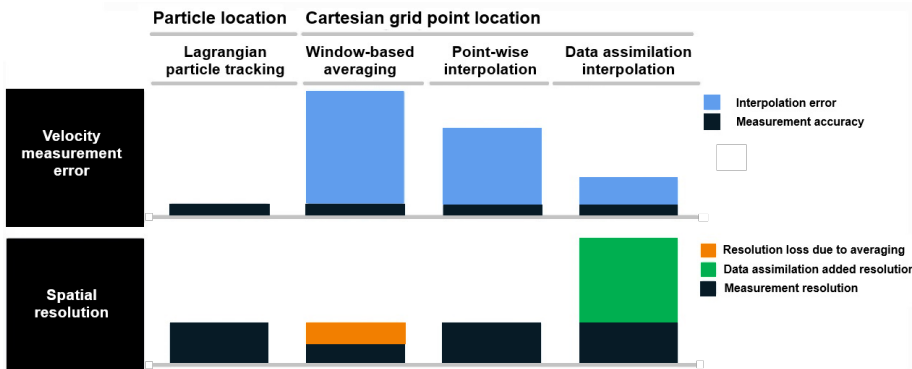, acceleration). The potential of 4D data assimilation has been already explored in the framework of variational methods in com-

putational fluid dynamics problems (Chandramouli, Mémin, and Heitz, 2020, among others).

The application to time-resolved sparse 3D data is recently being considered. The assimilation of measurements comprising a finite time interval (time-segment assimilation or TSA) has been introduced recently by Schneiders and Scarano (2016) in the framework of vortex-in-cell technique. In the latter work, the principle was introduced along with the analysis of synthetic data indicating the potential for delaying the cut-off wavenumber for spatial reconstruction.

A simpler, but computationally more efficient 4D (i.e. space-time), approach to the problem has been developed by Jeon et al. (2019) where the time-segment is spanned using Taylor approximation of the flow field velocity. The latter can be considered as an advection-based time-segment assimilation (ADV-TSA) that models the flow behaviour along a finite time interval. The study has brought evidence that an improved dense reconstruction can be achieved using different values of the time-segment. Yet, no conclusive criterion has been stated that defines an optimum for the time-segment length.

The above 4D techniques can be categorised as pouring time into space viz. enhancing the spatial resolution of the reconstruction from spatially sparse and temporally well resolved data. The latter conditions are encountered in a number of 3D flow measurements, in particular after the recent development of large-scale 3D PIV experiments by means of helium-filled soap bubbles where the flow velocity is sampled at the sparse tracers' locations.

2.4. DATA REDUCTION

The previous sections detailed the procedure by which velocity vectors are computed from scattered particles in the measurement domain. The information from the latter can be then gridded, with more or less sophistication, into a structured array of cells. The following part explains the various analyses that are performed to the gridded flows throughout the chapters of this dissertation.

2.4.1. STATISTICAL TOOLS

Turbulent flows are characterized by chaotic arrangement of scales with a wide range of size depending on the problem, implying the need of statistical analysis to filter the information and analyse turbulence. The following sections provide with basic mathematical instruments to extract statistical information from the acquired data.

Experimental data is classified into deterministic, for which there is a predefined mathematical description, and random, which is unpredicatble and described by statistical features. In this context, the velocity field is usually decomposed following Reynolds decomposition, into the mean part ($\overline{U}$(x), assumed as stationary) and the fluctuating part, **u'**(x,t):

$$\mathbf{U}(x,t) = \overline{U}(x) + \mathbf{u'}(x,t) \tag{2.5}$$

where x and t denote the spatial and time coordinates.

Regarding statistics, there is a need for large data ensembles to overcome the continuous spectrum of wavelengths and frequencies of turbulence.

As a measure of uncertainty, one can rely on the standard deviation, which is defined as,

$$std[U(x,t)] = \sqrt{var[U(x)]} = \sigma_U(x) \tag{2.6}$$

2.4.2. FREQUENCY ANALYSIS

As mentioned before, turbulent flows are dominated by a wide range of scales and frequencies denoted as turbulence. In order to separate between the flow phenomena of interest and turbulence, the frequency domain is the most desirable. The latter particularly applies to the analysis of signals, where the contribution of different frequencies is of interest. The transformation from temporal domain to the frequency domain is given by Fourier transform (Brigham, 1988). It decomposes a signal into a linear combination of orthogonal sinusoidal basis functions at different frequencies. The spectral information of the signal is thus the coefficients of the combination, or the amplitudes of the functions. A more sophisticated approach, yet based on the FT principle, is the Welch method (Welch, 1967). The method is based on segmenting the signal into shorter time series, allowing some overlap between them, typically 50%. The latter strategy was introduced by the Bartlett's method (Bartlett, 1950). Furthermore, the two methods filter these smaller sequences with a window function to yield a potential resolution. The frequency content is calculated for each filtered sequence. The resultant power spectral densities (PSD) are averaged to reduce the variance of the estimate when compared to a single periodogram of the entire signal.

Mathematically, the time series is partitioned into K segments with M points. For each segment, a windowed discrete Fourier Transform is computed:

$$X_k(v) = \sum x[m]\,w[m]\,e^{-j2\pi vm} \tag{2.7}$$

and a modified periodogram value $P_k(f)$:

$$P_k(v) = \frac{1}{\sum w^2[m]}\,|X_k(v)|^2 \tag{2.8}$$

Welch's estimate of the PSD is the average of the periodogram values:

$$S_x(v) = \frac{1}{K}\sum P_k(v) \tag{2.9}$$

2.4.3. PROPER ORTHOGONAL DECOMPOSITION

The Proper Orthogonal Decomposition (POD) is a statistical technique able to classify the flow in terms of the most energetic coherent motions resulting in a low-order reconstruction of the flow field. It consists of a linear mathematical procedure that identifies a set of orthonormal basis functions when solving the eigenvalue problem (Chatterjee, 2000).
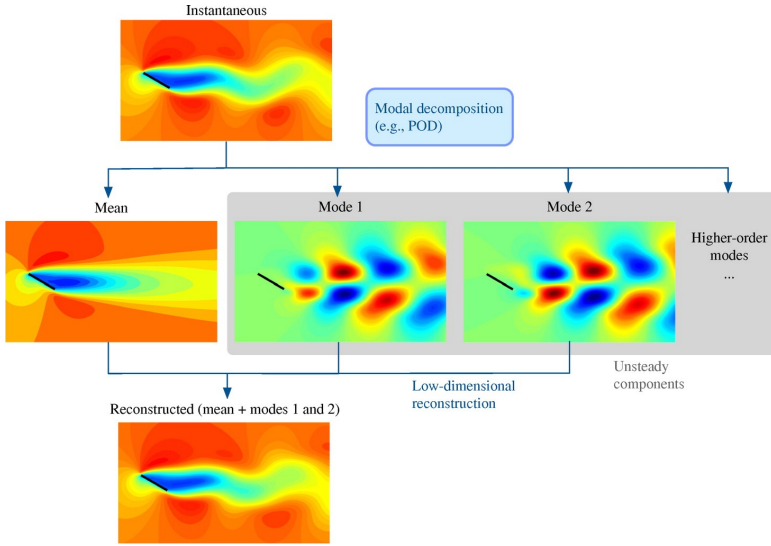
Figure 2.17: Sample Proper Orthogonal decomposition of flow around a pitched flat plate. Figure from Taira et al. (2017).

Typically, the technique is applied to the fluctuating component of the velocity decomposition (Equation 2.5). Therefore, the set of velocity fields are decomposed into a linear combination of orthogonal modes $\Psi(x)$ with the orthonormal amplitude coefficients $A_k(t)$ such,

$$u' = \sum A_k(t)\Psi_k(x) \tag{2.10}$$

The reconstruction is optimal in terms of maximizing the normalized average projection of Ψ,

$$\Psi_k(x) = \sum \phi_n^k u'(x, t_n) \qquad where \quad K = 1, 2...N \tag{2.11}$$

The modes of the decomposition can be found by solving the eigenvalue problem,

$$C_u\phi = \lambda\phi \tag{2.12}$$

where the eigenvalues denote the energy content of the modes and the eigenvectors the direction or shape. Therefore, the cumulative sum of the eigenvalues gives an insight of the relative kinetic energy gathered by such modes

$$e_k = \frac{\lambda_k}{\sum \lambda_i} \tag{2.13}$$

The POD decomposition has several applications, such as identifying mode or structures in flow fields (Berkooz, Holmes, and Lumley, 1993), reducing the order of the system as a low order reconstruction of a complex field (Raiola, Discetti, and Ianiro, 2015), or similarly cleaning undesired features from a sample set like noise or camera reflections (Mendez et al., 2017). In the current dissertation, POD will be applied to the wake

of cylinder-foil configuration in Chapter 5 in order to analyze the most energetic phenomena.
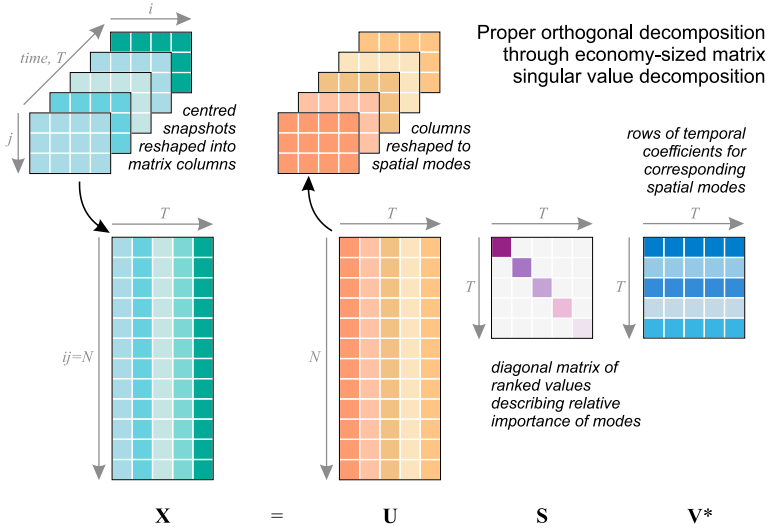
Figure 2.18: Schematic of POD inputs and outputs. Figure adapted from Ashmore et al. (2022).

2.5. PRESSURE RECONSTRUCTION

As introduced in Chapter 1, the key to understand the fluid-structure interaction mechanisms are the forces, and in particular the fluid force at the fluid-solid inter-phase, i.e. solid surface. All fluids matters are explained by the well-known Navier Stokes equations, from which the pressure is related to the conservation of momentum. The latter balances the change in fluid momentum from the forces acting on it, pressure forces, viscous forces, and body forces. An exemplified form of such velocity-pressure relation is given by Bernoulli equation, for which steady, incompressible and irrotational flow must hold:

$$p + \frac{1}{2}\rho V^2 = p_\infty + \frac{1}{2}\rho V_\infty^2 = const. \tag{2.14}$$

However, with most of the FSI problems in mind, the only assumption that may hold is flow incompressibility. Most aeroelastic phenomena are unsteady and imply some degree of flow rotation (Bisplinghoff and Ashley, 2013). Therefore, the Navier Stokes equation under incompressible flow ($\nabla \cdot \mathbf{u} = 0$) conditions could be used to compute the pressure from the momentum equation:

$$\nabla p = -\rho \frac{D\mathbf{u}}{Dt} + \mu \nabla^2 \mathbf{u} \tag{2.15}$$

Under some reasonable assumptions for most large scale applications, one realises that the key for the computation of the instantaneous pressure field is the material acceleration of the fluid particles, which is easily extracted from LPT techniques:

$$\frac{D\mathbf{u}}{Dt} = \left[\frac{d\mathbf{u}_p(t)}{dt}\right]_{Lag} = \left[\frac{\partial\mathbf{u}(t)}{\partial t} + (\mathbf{u}\cdot\nabla)\mathbf{u}\right]_{Eul} \qquad (2.16)$$

where the sub-indices *Lag* and *Eul* denote the Lagrangian and Eulerian perspectives respectively. Note that $\mathbf{u}_p(t)$ is the velocity of a particle at time t while $\mathbf{u}(t)$ is the velocity at a location from a stationary reference frame.

Despite the availability of the Lagrangian material velocity, the computation of the pressure field is desired in a gridded form due to the advantages of available solvers, such as Poisson. In order to compute the pressure field, one must take the divergence of equation 2.15, which reduces to:

$$\nabla^2 p = -\rho\nabla(\mathbf{u}\cdot\nabla)\mathbf{u} \qquad (2.17)$$

Additionally, information about the boundary conditions (BC) is always required to some extent in order to reconstruct the pressure accurately. BC are classified into two types attending to the order/derivative. Dirichlet condition is applied where the pressure itself is specified. This condition will be always needed in order to determine the static pressure field. Neumann condition, the most common, determine the pressure gradient along the surface normal and is usually present at the free flow boundaries where the pressure is unknown.

3

TECHNIQUE ASSESSMENT OF PIV AND DIC

*It is difficult to free fools
from the chains they revere.*

Voltaire

As learnt from Chapter 2, DIC is the most established optical technique for structural deformation and strain. However, for the case of flow measurements, reduction of modulation effects by tracking techniques poses an advantage compared to cross-correlation. Such advantage would be expected for structural measurements too. Thus, the coming chapter aims to prove the feasibility of using Lagrangian Particle Tracking approaches in combination with surface markers for tracking the deflection of an elastic object. This would reduce the complexity of experimental setups aiming at measuring aeroelastic quantities.The model for the measurements is a flexible plate under a controlled periodic motion exposed to a turbulent boundary layer, and the reference structural measurement is Digital Image Correlation.

3.1. Introduction

Some works in experimental FSI, such as Mertens et al. (2022) and Mitrotta et al. (2019), have already demonstrated reliable and accurate reconstruction of structural and fluidic motion is possible utilizing a single measurement system which removes the need to setup two different image acquisition configurations, separating flow and structure. Still today, digital image correlation is the preferred optical technique for the surface deformations even in experimental fluid-structure interaction scenarios (Maljaars et al., 2020; Mella et al., 2019). The present chapter aims to show that the latter complex configurations are no longer needed since tracking techniques are capable of delivering the same accuracy for structural measurements. As a part of the HOMER European Union H2020 project, the experimental setup employed in this section is designed to investigate fluid-structure kinematics of turbulent boundary layer-unsteady panel interactions where the experiments are conducted in a low-speed wind tunnel of TU Delft High Speed Laboratory.

3.2. Experimental setup

The experimental setup is designed with a square elastic membrane exposed to turbulent boundary layer conditions and equipped with two separate optical systems, as sketched in Fig. 3.1. The panel to be deformed is a square elastic membrane with sufficiently high moment of inertia to prevent any aeroelastic deformations and have full control over the membrane shape. It is clamped on an aluminum frame of $60 \times 60 \text{ cm}^2$ from all edges to restrict its motion to only elastic deformations and avoid any translational motion. A DC motor is connected to the center of the membrane by means of a gear and rod mechanism (Fig. 3.2, top-right).
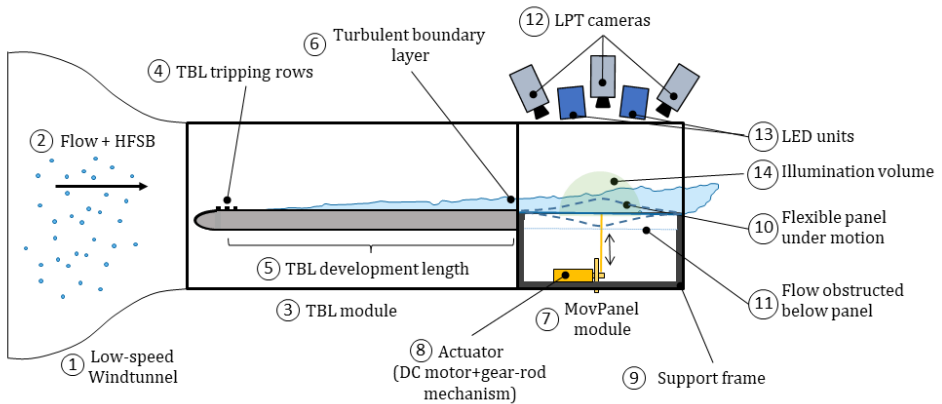
Figure 3.1: Schematic representation of the experimental setup for turbulent boundary layer interactions with unsteadily deforming elastic membrane.

The membrane is steadily deformed at three different stages of upward, middle and downward positions, and unsteady deformed while being actuated at three different frequencies of 1 Hz, 3 Hz and 5 Hz with an amplitude of 30 mm from valley to crest (Fig. 3.3).

The corresponding reduced frequencies ($k = \omega \times b/V_\infty$) obtained with the membrane motion of 1 Hz and 3 Hz (b = 0.25 m & V_∞ = 12 m/s) are in the order of $k_{1\,\text{Hz},3\,\text{Hz}} \leqslant 0.06$ where a quasi-steady state can be assumed. However, the reduced frequency at 5 Hz reaches to a level of $k \approx 0.2$ and shall be considered within the unsteady aerodynamics regime (Leishman, 2006).
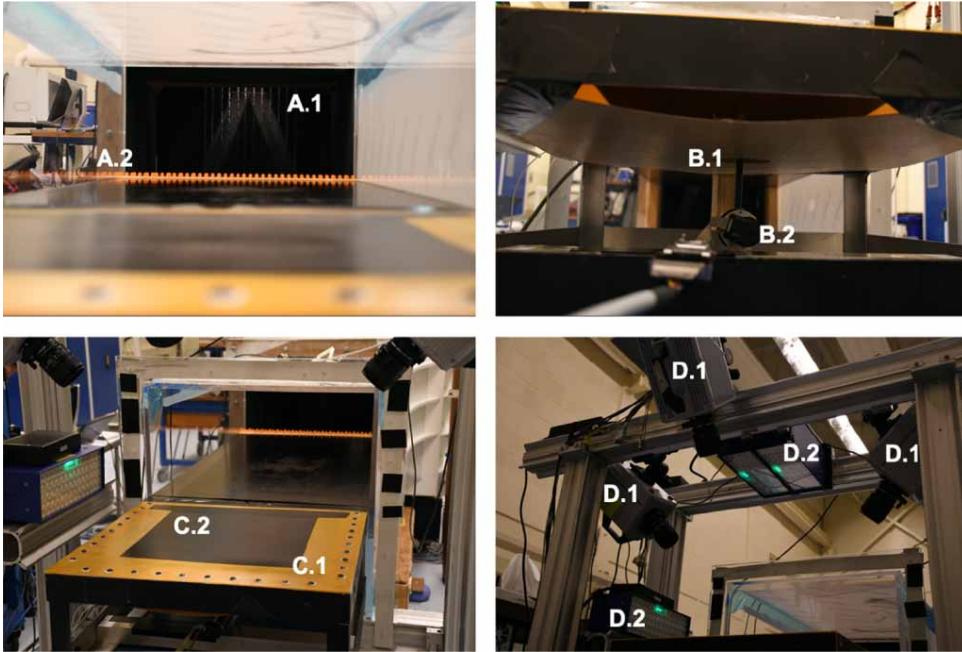
Figure 3.2: Photos of the experimental setup; HSFB seeding rakes (A.1) and boundary layer tripping Lego blocks (A.2)(top-left), gear and rod mechanism (B.1) connecting the membrane to the DC motor (B.2)(top-right), elastic membrane (C.1) with surface markers (C.2)(bottom-left) and image acquisition setup (D.1 & D.2) (bottom-right).

Moreover, a black foil with a regular grid of light-grey dots (0.8 mm diameter, 10 mm distance between adjacent dots, 36 × 36 dots) is applied to the upper face of the elastic membrane to enable the structural displacement measurements by means of LPT (Fig. 3.2, bottom-left and Fig. 3.3, top). On top of the black foil, a speckle pattern of a orange fluorescent paint is sprinkled for the DIC measurement (see Fig. 3.4 where the raw images acquired by the Phantom cameras are provided).

A 120 cm long rigid plate with Lego blocks of 9.6 mm height located at 10 cm from its leading edge is installed upstream of the model to ensure well-developed turbulent boundary conditions at the test section (Fig. 3.1).

The image acquisition for the LPT system is performed with three Photron FastCAM SA1.1 CMOS cameras (1024 × 1024 pixels, 12-bit, 20 μm pixel size) mounted 40 cm above the moving panel positioned to form a 60º angle (Fig. 3.2, bottom-right). Band-pass filters were installed on the lenses to block the light reflected from the fluorescent paint used for the DIC measurements. A laser cone from a Quantronix Darwin-Duo Nd:YLF
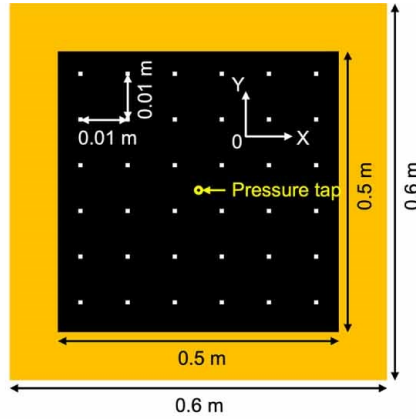
Figure 3.3: Schematic representation of the elastic membrane utilized in the experimental campaign equipped with a black foil of regular grided light-grey dots (top).

laser (25 mJ pulse energy at 1 kHz, 527 nm wavelength) was used for volumetric illumination of the flow and panel surface. Details of the experimental setup and measurement configurations are provided in table 3.1.

Table 3.1: Setup parameters for the experimental investigation of turbulent boundary layer interactions with unsteadily deforming elastic membrane.

Freestream velocity	10 m/s
Reynolds number	$Re_l = 500\,000$
Lagrangian Particle Tracking	
Illumination	Quantronix Darwin-Duo Nd:YLF laser (2×25 mJ)
Recording devices	3 × Photron FastCAM SA1.1 CMOS
Acqusition frequency	3000 Hz
Measurement volume	$20 \times 20 \times 15$ cm^3
Digital Image Correlation	
Illumination	LED 300(Blue)
Recording devices	2 × Phantom VEO 640L
Acqusition frequency	3000 Hz
Measurement area	20×20 cm^2

3.2.1. LPT processing

The processing of raw images acquired throughout the experimental campaign are performed with the commercial software package *DaVis 10.0.5* from LaVision GmbH. In order to reduce reflections from the DIC paint and increase the signal-to-noise ratio, the images were preprocessed before the 3D reconstruction of the markers see Fig. 3.5.

Raw images (Fig 3.5-left column) are substracted an sliding minimun filter of 9 × 9 pix^2 (Fig 3.5-centre column). Furthermore, in order to reduce the background noise, images are reduced in intensity by 50 counts. Finally, a Gaussian smoothing (Fig 3.5-right
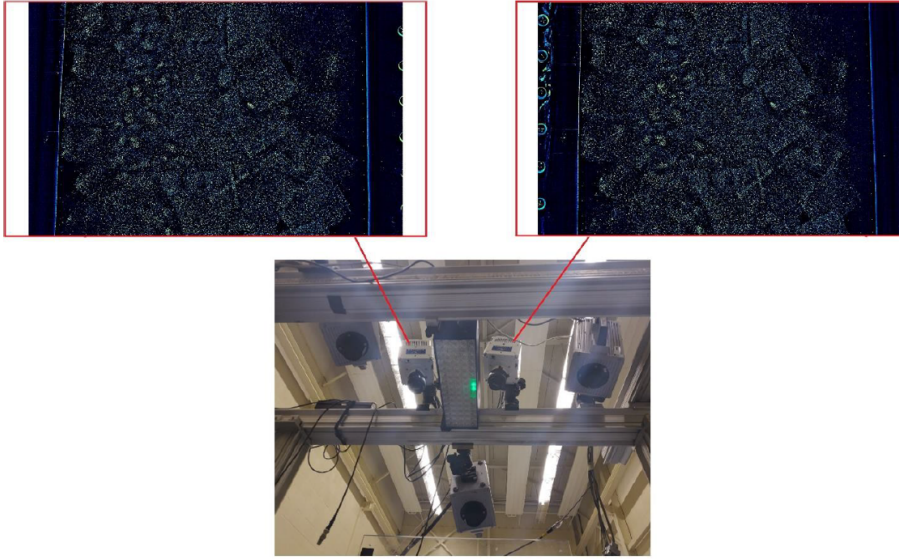
Figure 3.4: Experimental setup with two Phantom VEO 640L and blue LED 300 for DIC measurements and the three Photron SA1.1 cameras for the LPT measurements (bottom); images of the speckle pattern on the panel surface, as seen by the two Phantom cameras (top).

column) prior to the tracking algorithm, eases the recognition via the optical transfer function embedded in STB (Schanz et al., 2012).

For reconstructing the markers motion, the preprocessed images are provided to STB algorithm for LPT (Schanz, Gesemann, and Schröder, 2016). Accordingly, the particle tracks are reconstructed with a minimum track of seven instances which are regularized with second order polynomials for the computation of velocity and acceleration information.

3.2.2. DIC PROCESSING

For the DIC measurements, two Phantom VEO 640L cameras (2560x1600 pixels, 12-bit, 10 μm pixel size) were positioned forming a 20° angle and had long-pass filters installed for light separation. Two LED light sources (LaVision LED-flashlight 300) are used for illumination of the measurement volume, mounted between the cameras projecting the blue light perpendicular to the panel from the above(Fig. 3.4, bottom-right).

3.3. FLEXIBLE PANEL - TURBULENT BOUNDARY LAYER INTERACTION

The main aim of the TBL – panel interaction experiment was to assess the accuracy of the STB measurements of the surface markers via comparison with the DIC measurements. Figure 3.7 shows the time-evolution of the wall-normal position (z-direction) of a tracked marker; the red squares represent the STB measurements, whereas the blue dotted line

3
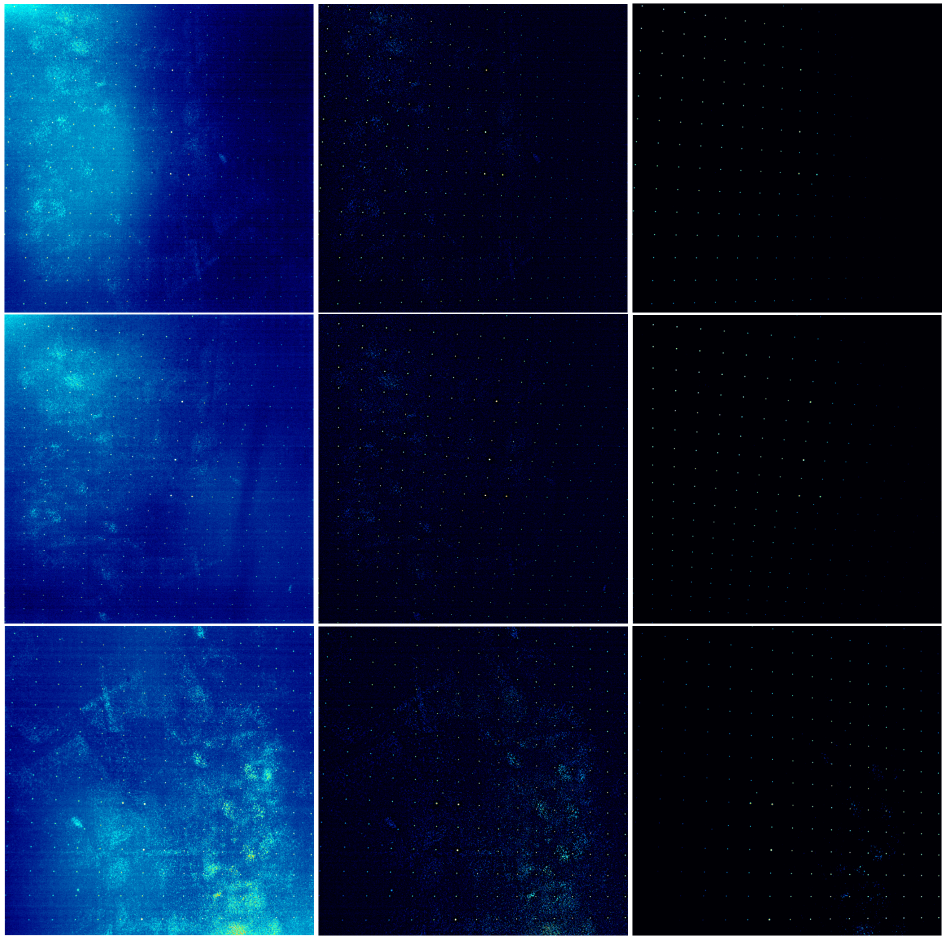
Figure 3.5: Pre-processing steps from raw images (fist column) to LPT input (last column). Each row corresponds to each camera (3 in total). Intensity range constant: 0-500 counts.

correspond to the DIC measurements at the same location. The two measurement approaches return very similar displacement values, with only small discrepancies. The difference between the displacements measured by the two techniques over a cycle had a mean value of 10 μm or 0.03% of the peak-to-peak displacement, and a standard deviation of 35 μm or 0.12% of the peak-to-peak displacement. Further reduction of such difference was achieved when the raw measurements from Lagrangian Particle Tracking were regularized via a moving space-time polynomial filter. In the latter case, the displacements measured from LPT and DIC were comparable in terms of accuracy.

The uncertainty of the DIC measurements was quantified by LaVision GmbH within HOMER project to 3 to 4 μm for the in-plane displacement, and under 10 μm for the out-of-plane displacements, which correspond to 0.02 pixels for the in-plane displacements, and under 0.05 pixels for the out-of-plane displacements. This displacement uncertainty

is in line with the values reported in the literature for DIC measurements (Pan et al., 2009).
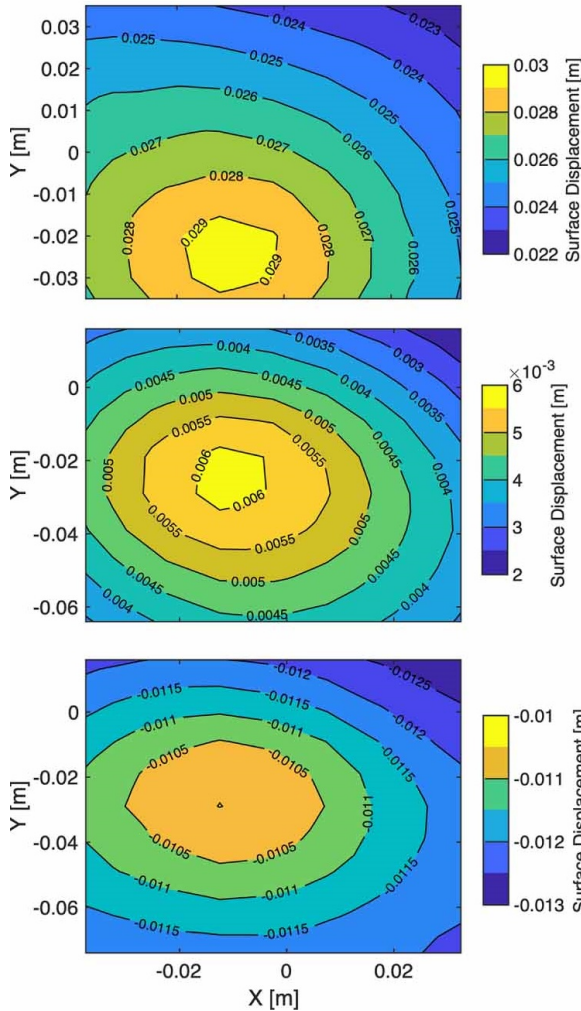
Figure 3.6: Reconstructed membrane shapes from LPT measurement with surface displacements at upward, neutral and downward (top to bottom) deformed positions.

3.4. Conclusions

A comparison between cross-correlation and tracking approaches was presented for structural displacement measurements. The experiment regarded an actuated flexible panel measured simultaneously by two different optical systems. The separation strategy followed was light frequency distinction.

Results show that both techniques, LPT and DIC, perform very similarly when capturing the evolution of the moving surface, with the standard deviation of the differences

being as low as 0.1% of the motion amplitude. It can be concluded then that even if digital image correlation is the standard technique for displacement measurements, tracking approaches may substitute them in order to reduce the number of measurement apparatus and decrease experimental cost and complexity in general.

Yet, it is true that the assessment of the techniques was performed at a single location of the surface, meaning no information about the spatial resolution is inferred. In this context and for the current experiment, DIC technique is expected to provide with a richer measurement, as the smallest scale is given by the interrogation window of the cross-correlation process. For the tracking approach, the detection of surfaces features are limited by the inter-marker distance, $d = 1$ cm for the current case. Nonetheless, large-scale FSI applications do not present scenarios where the structural motions or deformations are relatively large compared to the flow features they interact with, thus not requiring the spatial resolution of DIC technique.

Figure 3.7: Simultaneous measurement of the vertical position of a point of the panel conducted with Lagrangian Particle Tracking (Shake-the-Box algorithm, STB), and Digital Image Correlation (DIC). Panel motion actuated at 1 Hz frequency. Zoomed views of the crest and valley of the displacement curve are provided at the top right and bottom right, respectively.

4

CLOSURE OF COLLAR´S TRIANGLE

And one path we shall never choose,
and that is the path of surrender, or submission.

John F. Kennedy

The following chapter gathers the challenging step of closing Collars triangle. Once all the agents involved in the fluid-structure interaction problem have been introduced, and it is clear what techniques are the most suitable to measure the forces, one can attempt to compute the latter and close the triangle. In the current chapter, an experimental methodology is proposed to study aeroelastic systems with optical diagnostics. The approach locally evaluates the three physical mechanisms that produce the forces involved in Collar's triangle, namely aerodynamic, elastic, and inertial forces. Flow and object surface tracers are tracked by a volumetric particle image velocimetry (PIV) system based on four high-speed cameras and LED illumination. The images are analysed with Lagrangian particle tracking techniques, and the flow tracers and surface markers are separated based on the different properties of their images. The inertial and elastic forces are obtained solely analysing the motion and the deformation of the solid object, whereas the aerodynamic force distribution is obtained with pressure from PIV techniques. Experiments are conducted on a benchmark problem of fluid–structure interaction, featuring a flexible panel installed at the trailing edge of a cylinder.

The present chapter describes the foundational aspects of the experimental hardware and procedures needed to diagnose the aeroelastic forces non-intrusively by use of PIV techniques. The measurements are intended for the closure of Collar's triangle by a single experiment, that is, simultaneously determining all dynamic forces acting within the FSI problem. The demonstration makes use of a benchmark problem for aeroelasticity i.e. the oscillation of a flexible thin plate trailing a circular cylinder immersed in a fluid stream.

4.1. FSI MEASUREMENT WORKING PRINCIPLE

Let us consider a flexible, thin panel of length L, width W and thickness T (T $\ll$ L,W) in oscillatory motion induced by aerodynamic forces arising from the air flow as illustrated in Fig. 4.1. The aerodynamic loads consist of pressure p and friction τ. The object opposes deformation by its stiffness, and acceleration motions by its inertia.
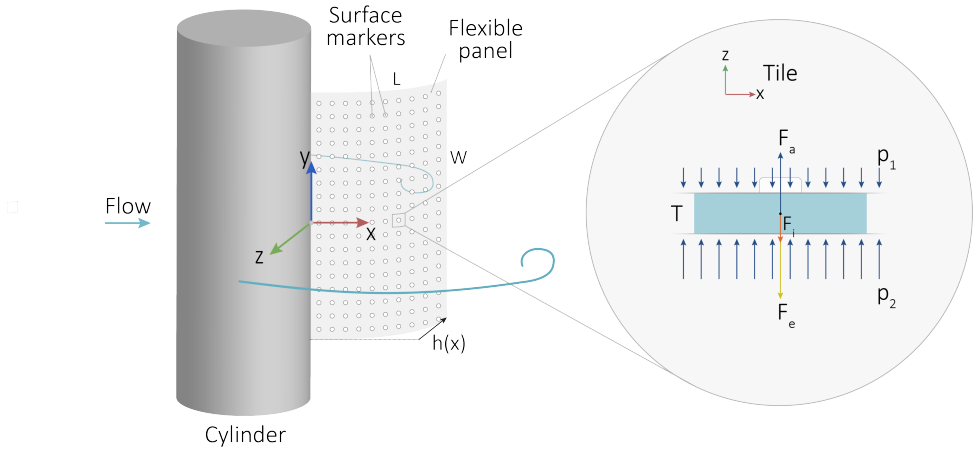
Figure 4.1: Schematic of a cylinder-trailing foil system (left) and forces acting on a tile element (right). The coordinate system (streamwise, x; spanwise, y; transverse, z) chosen for the current work is included as reference.

Considering a square tile of such panel, i.e. a small element of side length l (see Fig. 4.1), the equilibrium of forces acting on such element reads as:

$$\sum \mathbf{F} = \mathbf{F}_i + \mathbf{F}_e + \mathbf{F}_a = 0 \qquad (4.1)$$

where F_i, F_e and F_a stand for the inertia, elastic, and aerodynamic forces, respectively. For the current work, the aforementioned vector identity will be reduced to the dominant direction of motion, z or transverse component, under the assumption of small deformations. As a consequence, the vector Eq. 4.1 is projected along z and rewritten as a scalar relation. Note that z will be used as coordinate along the thickness of the element, with $z = 0$ corresponding to the middle of the plate in the undeformed state. In addition, for a simplified treatment of the problem, the quantities will be hypothesized uniform along the spanwise direction y; thus, the forces will be related solely to

the streamwise component, *x*. The accuracy of the latter hypothesis is verified for the experiment presented in the remainder of the work.

4.1.1. INERTIA FORCE

A tile subject to non-zero elastic and aerodynamic forces will accelerate in proportion to such forces. Based on Newton third principle, the reaction force F_i due to inertia acts in the direction that opposes its acceleration *a*. For a tile element, the expression of the inertia force reads as:

$$F_i = -m \cdot a = -l w T \rho_m \cdot \frac{d^2 h}{dt^2} \tag{4.2}$$

In the above equation, ρ_m is the density of the material and the displacement of the plate mid-point along *z* is denoted by *h*, as illustrated in Fig.4.1. The measurement of the object displacement and motion is typically performed by means of optical markers applied onto the surface of the panel. The markers positions in time are recorded, while their velocities and accelerations are computed from time derivatives of the positions. The inertial force is then obtained by knowledge of the tile's specific mass and volume.

4.1.2. ELASTIC FORCE

Elastic forces arise as a reaction of the object opposing deformation. The present discussion pertains to the linear elastic regime. For small displacements, the force can be considered to act normal to the surface and tensional forces (e.g., arising from aerodynamic skin friction) are neglected. In the above conditions, the whole elastic force reduces to the bending stress only.

Considering a thin deformable body, a 1-D simplification of the Kirchhoff-Love plate theory (Reddy, 1999) provides a relation between the deformation of the tile and the elastic forces, given its physical attributes. According to such theory, and invoking the strain-displacement and the stress-strain relations, the stress along the body reads:

$$\sigma_x = -\frac{E}{1 - v^2} z \cdot \frac{\partial^2 h}{\partial x^2} \tag{4.3}$$

where *E* is the Young modulus and *v* is the Poisson ratio. The linear dependence on *z* indicates tensile/compressive stresses at the opposite faces of the panel. The non-uniform normal stress distribution gives rise to a moment reaction. Finally, considering the tile moment equilibrium, the elastic reaction force, which results normal to the surface, can be expressed as,

$$F_e = -\frac{E l w T^3}{1 - v^2} \cdot \frac{\partial^4 h}{\partial x^4} \tag{4.4}$$

The complete derivation of the Kirchhoff-Love plate theory for 3D solids can be found in the book of Panc (1975). Once the material properties are known, the experimental evaluation of the elastic force relies on the assessment of the 4th spatial derivative of the instantaneous deformed shape $h(x)$. The latter is regarded as a challenging task for an experiment, where even a small extent of measurement noise propagates and amplifies through the multiple operations of spatial differentiation.

4.1.3. AERODYNAMICS FORCE

Aerodynamics loads are usually decomposed into normal (pressure) and shear (friction) stresses. Friction is negligible in most aeroelastic regimes (Fung, 2008). Moreover, the pressure loads on a thin panel reduces the discussion to the pressure difference Δp from its opposite sides. The aerodynamic force acting on the tile reads as:

$$F_a = \Delta p \, l \, w \tag{4.5}$$

The pressure field can be inferred from the velocity (and acceleration) distribution invoking the momentum equation. The latter in turn requires the numerical solution of the Poisson equation for pressure (Van Oudheusden, 2013). The instantaneous aerodynamic force is not straightforward to obtain from fluid flow measurements as it typically requires high-quality time-resolved 3D measurements (Beresh, 2021). Moreover, the choice of boundary conditions can largely affect the evaluation of the pressure field (Neeteson et al., 2016). To minimize errors due to low spatial resolution or unwanted light reflections close to solid surfaces, the surface pressure is typically estimated imposing Dirichlet boundary conditions for the pressure values in the external flow region, where the Bernoulli relation between pressure and velocity holds true. In the rotational flow region (shear layers and separated wake), the integration of the pressure can follow the 3D propagation scheme recently proposed by Jux, Sciacchitano, and Scarano (2020). It should be stressed that the evaluation of the unsteady pressure distribution over a generic surface, curved and in motion, time-resolved three-dimensional flow field measurements are required that surround such surface.

4.1.4. COLLAR'S TRIANGLE OF FORCES

Equation 4.1 can be rewritten combining the explicit terms obtained in equations 4.2, 4.4 and 4.5. The resulting equilibrium of forces is expressed as:

$$-T\rho_m \cdot \frac{d^2 h}{d t^2} + \frac{ET^3}{1 - v^2} \cdot \frac{\partial^4 h}{\partial x^4} + \Delta p = 0 \tag{4.6}$$

From such equation, the structural parameters (plate thickness T) and material properties (density ρ_m, Young modulus E and Poisson ratio μ) need to be known. The corresponding values applying to the current experiment are gathered in Table 4.1. The remaining elements in the equation, such as the pressure difference Δp, the local acceleration and the spatial derivatives of the deformed shape need to be measured to close the problem.

It is worth mentioning that although the above identity theoretically holds, the experimental determination of such forces has inherent uncertainties. The latter are mostly associated with the measurement techniques adopted to monitor the flow and object motion. Therefore, one can already predict a residual force when computing the force equilibrium for Collar´s triangle, referred to as Collar Closure Criterion (CC) force ϵ_{CC}:

$$\epsilon_{CC} = -T\rho_m \cdot \frac{d^2 h}{d t^2} + \frac{ET^3}{1 - v^2} \cdot \frac{\partial^4 h}{\partial x^4} + \Delta p \tag{4.7}$$

In the present study, an optical diagnostic system based on PIV techniques is developed for the purpose of determining the above forces. The fluid flow velocity is obtained

over an extended three-dimensional domain by tracking large tracers (sub-millimetre helium-filled soap bubbles, HFSB (Scarano et al., 2015), along their trajectories to determine the flow pressure. The acceleration of the structural element is measured by tracking the motion of surface markers with the same algorithm as for the fluid tracers. Finally, the deformation of the panel is inferred from the analysis of the markers position and their relative displacement, respectively.

4.2. EXPERIMENTAL SETUP

The following experimental description is already given in Chapter 3. A summarized version is included for completeness.

4.2.1. FLOW FACILITY AND MODEL

The experiments were conducted at the Aerodynamics laboratory of TU Delft (Aerospace Faculty), in an open-jet open-return wind-tunnel of 600×600 mm^2 exit cross section. A cylinder of 90 mm diameter was installed vertically with a flexible transparent foil attached along the rear mid-plane. The foil (size 105×200 mm^2) undergoes a 2D motion excited by the periodic shedding of vortices in the Kármán wake of the cylinder. The maximum amplitude of oscillations in a 2D regime is observed at a free stream velocity $U_\infty = 2.25$ m/s (Re $= 1.35 \times 10^4$), where experiments are conducted. The foil optical transparency allowed to track flow tracers at both sides of it even when looking from only one side. However, the amount of detected flow tracers behind the foil was slightly lower than in the region with direct view, as a result of incomplete light transmission through the foil.

Table 4.1: Physical properties of the flexible foil and tile

Dimensions	Thickness, T (mm)	0.25
	Length, L (mm); l (mm) (tile)	95, 10
	Width, W (mm); w=l (mm) (tile)	200, 10
	Aspect ratio, L/W	0.475
Material	Density, ρm (kg/m^3)	1290
	Young modulus, E (GPa)	1.0
	Poisson ratio, ν (-)	0.3
Interaction parameters	Mass ration, m$^* = (\rho_m/\rho_f)\cdot$ (T/L) (-)	2.77
	Cauchy number, Ca $= (\rho_f U^2 W L^3)/$EI (-)	7.8

For the measurement of the foil kinematics, a regular pattern of 210 bright surface markers was applied to the foil. The markers had an average diameter $d_m = 0.8$ mm and a pitch $p_m = 1$ cm. The overall experimental setup is illustrated and provided in Fig. 4.2.

4.2.2. FLOW AND STRUCTURAL MEASUREMENT

The flow was seeded with neutrally buoyant sub-millimetre (mean diameter d $\approx 350\mu$m) helium-filled soap bubbles (HFSB), released by an in-house 200-generator seeding rake installed in the tunnel settling chamber (similarly to Jux et al., 2018). The nominal production rate of the flow tracers is 6×10^6 bubbles/s, resulting in a seeding concentra-

4
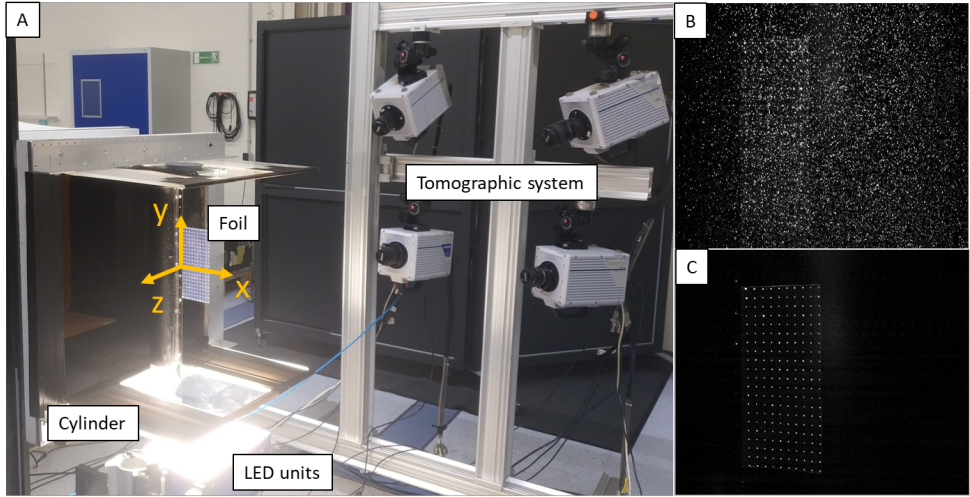
Figure 4.2: Experimental arrangement with cylinder and foil and system of coordinates. Illumination (by LED units) and tomographic imaging system (four CMOS cameras).

tion of ≈ 10 bubbles/cm^3 for a free stream velocity $U_\infty = 2.25$ m/s at the test section (seeded streamtube of 60×25 cm^2). For the current experiment, only 100 generators were operated to reduce the seeding concentration to ≈ 5 bubbles/cm^3, so as to satisfy the condition on the maximum number of particles per pixel (ppp = 0.05) for 4-camera tomographic systems (Elsinga et al., 2006; Scarano, 2012).

A measurement volume of $22 \times 40 \times 20$ cm^3 was illuminated vertically (spanwise direction) by two LaVision Flashlight 300 LED banks located under the test section. In the current experiments, flow tracers were measured at both sides of the transparent foil. A mirror was installed at the top plane of the test section to increase the light intensity in the measurement volume, thus allowing to identify the tracer particles also in the region behind the foil. The imaging system consisted of four high-speed cameras (1024×1024 pixels, 12 bit, 20 μm pixel pitch) mounted in a tomographic configuration 90 cm away from the foil, as shown in Fig. 4.2. The cameras subtended an aperture of approximately 30 degrees. Details of the optical system used in the experiments are summarized in Table 4.2.

Table 4.2: Optical system information

Illumination	2 × LaVision Flashlight 300 LED
	2 × Photron FastCam SA1.1 (1024x1024 pixels, 5400 fps)
Cameras	1 × Photron FastCam SA5 (1024x1024 pixels, 7000 fps)
	1 × HighSpeedStar 8 (1024x1024 pixels, 7000 fps)
Imaging	3 × Objectives Nikkor 50 mm - f# 1/11.2
	1 × Objectives Nikkor 60 mm - f# 1/11.2
Acquisition frequency	1000 Hz

The image acquisition and processing were conducted with the *LaVision Davis 10.0.5* software. Sets of 5000 images were recorded in continuous mode at a rate of 1 kHz. Samples of the latter can be visualized in Fig. 4.3. For the calibration process, a geometrical calibration (Soloff, Adrian, and Liu, 1997) was followed by the volume self-calibration (Wieneke, 2008) and optical transfer function determination (OTF calibration, Schanz et al., 2012). The surface markers were visually distinguished from the flow tracers based on their distinct optical characteristics. In order to track most fluid tracers (spherical bubbles) and most structural markers (2D flat bright circles), the volume self-calibration and the OTF calibration were performed separately with clean runs containing only one tracer type. Both the flow tracers' velocities and the foil markers motions were then evaluated by means of the Shake-the-Box Lagrangian Particle Tracking (LPT) algorithm (Schanz, Gesemann, and Schröder, 2016). Based on the work of Bhattacharya and Vlachos (2020), particle location uncertainty is expected below 0.3 pixels for IPR-based reconstructions and further decreases to 0.1 pixels when the particles are track over multiple time instants with the STB algorithm (Sciacchitano, Leclaire, and Schroeder, 2021).
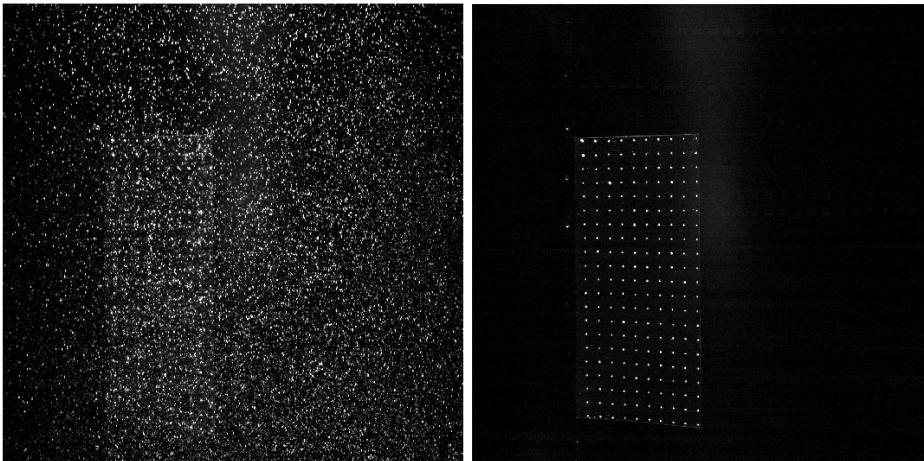
Figure 4.3: Left: digital recording capturing the marked surface and HFSB flow tracers. Right: digital recording of surface markers only.

4.3. DATA REDUCTION FOR LOAD ESTIMATION

The following section describes the data reduction procedure to obtain the distribution of forces along the foil from the analysis of the tracers and markers motion.

4.3.1. STRUCTURAL FORCES

As explained in section 4.1, inertial and elastic forces are determined from the time and space derivatives, respectively, of the measured instantaneous foil's shape. In order to avoid noise propagation through the derivation process, a spatio-temporal least-square regression is performed on the locations of the markers to generate a coherent smooth surface. The regression makes use of a high order polynomial in space (fifth

for x-direction and second for y-direction) and a second order in time, which is applied to all the measured markers over time stencil of 17 samples (10 of one oscillation cycle). The resulting foil's shape is calculated on a Cartesian grid with 0.5 cm spacing in both streamwise and spanwise (x and y, respectively) directions. Therefore, the foil can be considered as discretised by adjacent square tiles, each centred at a grid node and having a surface area of 0.25 cm^2 (0.5 cm × 0.5 cm). The derivations in time and space to determine the acceleration and elastic force, respectively, are conducted analytically based on the polynomial description of the foil's instantaneous shape. The uncertainty of the elastic and inertia forces is quantified based on the uncertainty of the regression coefficients of the least-square fit (Montgomery, Peck, and Vining, 2021) and linear error propagation.
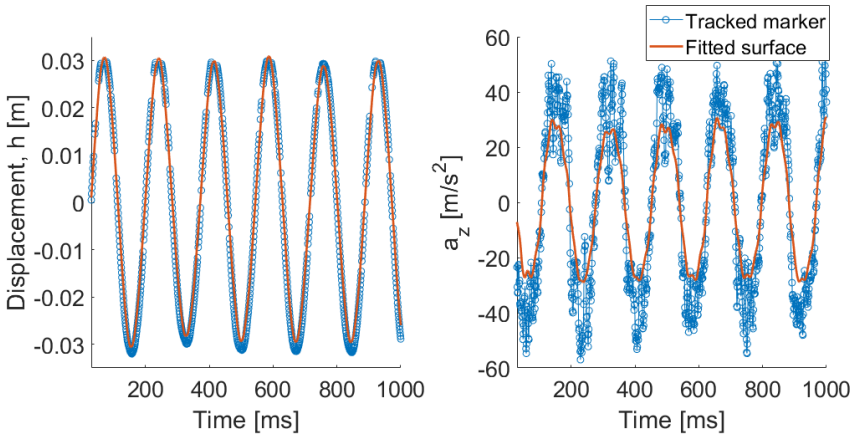
Figure 4.4: Kinematics of a measured surface marker (dotted blue) and projection onto the fitted surface (solid red) at the location ($x/L = 0.75$, $y/W = 0.5$). Left: marker displacement; Right: marker acceleration.

The comparison between the raw markers' measurements and the foil's position and acceleration based on the regression analysis is illustrated in Fig. 4.4 and Fig. 4.5. Fig. 4.4 compares the kinematics in time of a tracked surface marker with that of its projection onto the reconstructed surface. From this figure, the periodicity of the foil's motion both in terms of displacement and acceleration is evident, with the oscillation period equal to $T = 175$ ms. The use of the least-square regression allows to reconstruct missing time samples throughout the entire sequence (Fig. 4.4-left) and to clearly suppress the noise in the foil's acceleration (Fig. 4.4-right). Figure 4.5 displays the instantaneous location of the markers (in black circles) and the fitted surface at one of the extrema of the cycle, showing a contour of the transverse displacement. Even when some of the markers are not correctly reconstructed, the regression surface provides a full description of the entire foil.

4.3.2. FLUID LOAD
Finally, the surface pressure distribution along the foil is evaluated for the determination of the aerodynamic forces. The volumetric pressure field is computed based on the solution of the Poisson equation for pressure in incompressible fluids (De Kat and Van
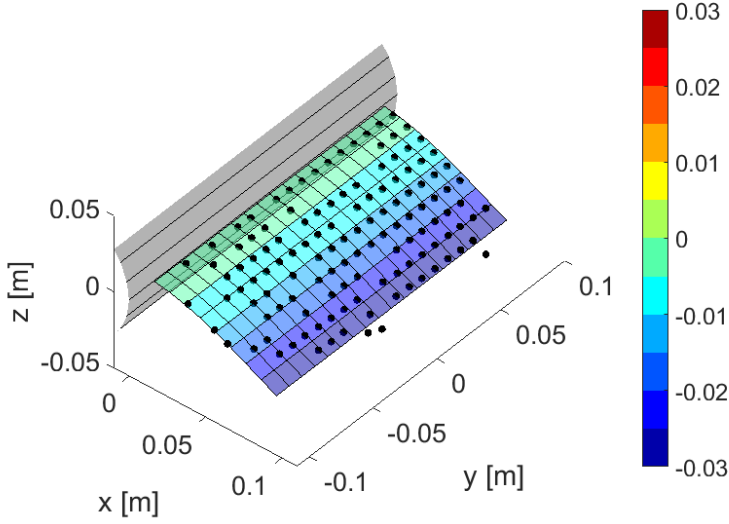
Figure 4.5: Instantaneous description of raw markers (in black circles) with the fitted surface color-coded by transverse displacement h (in [m]).

Oudheusden, 2012), which results from the divergence of the equation of conservation of momentum:

$$\nabla^2 p = \nabla \cdot \left(-\rho_f \frac{D\mathbf{u}}{Dt} + \mu \nabla^2 \mathbf{u} \right) \tag{4.8}$$

The computation of the pressure field relies upon the material derivative of the velocity $D\mathbf{u}/Dt$, which is readily available from the LPT measurements, and the viscous dissipation $\mu \nabla^2 \mathbf{u}$. Due to the high Reynolds ($Re = 2 \times 10^4$), the latter term is neglected for the pressure computation. As shown by Van Oudheusden et al. (2007) for a flow problem at similar Reynolds number, even in regions of high flow curvature, the viscous contribution to the pressure gradient is two orders of magnitude smaller than the other contributions.

Dense velocity reconstruction from particle tracks is performed with the VIC# algorithm implemented in *DaVis 10.1* (Jeon et al., 2018). The approach is based on the Vortex-in-Cell method for VIC+ (Schneiders and Scarano, 2016) and optimises the vorticity field that best fits the measured velocity and acceleration by minimizing a cost function J built upon the disparity between the computed and the measured variables. Pressure integration is performed simultaneously to the velocity reconstruction by solving the Poisson equation with Neumann conditions at every boundary and a constant Dirichlet condition at a free stream location.

Because the applicability of the VIC# algorithm is limited to Cartesian domains not containing solid objects, the pressure reconstruction is only performed over two separate regions of the measurement domain that span from its outmost boundaries to the limits of the foil motion (approximately 4 cm away from the neutral position of the foil).

Hence, the foil does not enter the fluid domain under consideration for the VIC# reconstruction (black rectangles in Fig. 4.6). For the determination of the actual surface pressure on the foil, the pressure is then extrapolated towards the foil location (from both sides) via a nearest neighbour approach, neglecting the change of static pressure across the shear layer and the wake (Schlichting and Gersten, 2016).

In order to determine an upper bound of the uncertainty of the reconstructed pressure, the aforementioned approach is performed from the outer regions towards the mid location ($z = 0$) at downstream locations of the trailing edge of the foil. The directions of extrapolation and the mid location are shown with black arrows and a red cross in Fig 4.6, respectively. The difference in static pressure at the latter location when computing it from opposite directions, $\epsilon_p = 1.7$ Pa, gives an estimation of the uncertainty of pressure jump across the foil.
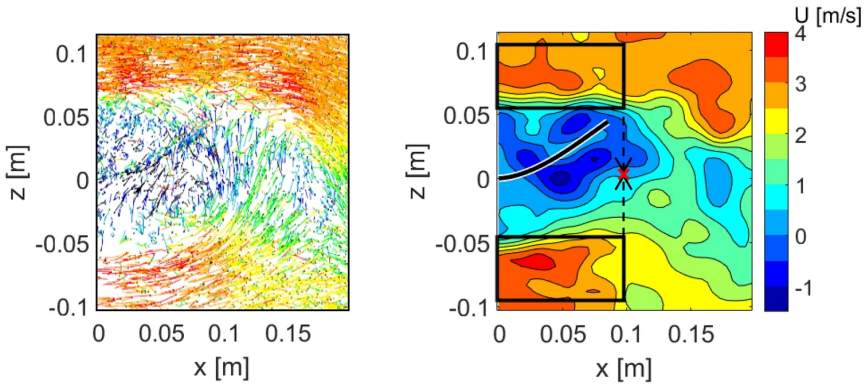
Figure 4.6: Left: particle tracks in a slide of the measurement domain color-coded by streamwise velocity. Right: instantaneous streamwise velocity reconstructed at the same time instant. Pressure evaluation in the regions highlighted by black rectangles.

4.4. RESULTS

The flow velocity fields are analysed first, before discussing the loads of Collar's triangle and the resulting structural motion. Despite the 3D flow measurement, given the oscillations feature a quasi-2D behaviour and for sake of conciseness, only 2D flow data will be presented and discussed. The latter assumption is verified on both structural and flow data. The foil deformation presents a 2.5% deviation over different locations along the span of the foil. For the flow, the streamwise velocity component is taken as reference. The standard deviation along the span reaches at most 10% of the local average velocity, which is ascribed to the inherent turbulence of the flow. Hence, spanwise averaging is considered a valid approach in this problem to enhance the data density without any loss of flow or structural information.

A view in the median x–z plane illustrates velocity vectors and contours of the streamwise component (Fig. 4.7-top row). The values shown are averaged along the y-direction, where also the foil location is indicated. The velocity field reveals the oscillatory be-

haviour of the wake as expected in the regime of Kármán vortex shedding. The foil position also reveals its oscillatory motion. However, the foil does not appear to be in phase with the wake axis oscillations. The position and phase of the vortices shed in the cylinder wake are made more evident by displaying the transverse velocity component, where a negative blob followed by a positive one indicates a counter-clockwise rotating Kármán vortex. The dominant frequency of the flow could be already inferred from the sequence, and it corresponds to that of the flapping foil, $f \approx 5.7Hz$. The latter is verified from the time evolution of the transverse flow velocity, displayed in blue in Fig. 4.8. Note that the computed Δp is also included in Fig. 4.8 and exhibits a different frequency, in particular double to that of the transverse velocity. This can be explained from the fact that low-pressure regions arise at the vortex core locations regardless of the rotation direction of the vortex, thus resulting in double the pressure dominant frequency with respect to the flow. Nevertheless, the measured flow dominant frequency agrees well with the characteristic frequency for cylinder shedding wakes in the sub-critical regime, $St \approx 0.2$ (Williamson, 1996), apparently, unaffected by the presence of the flexible foil.
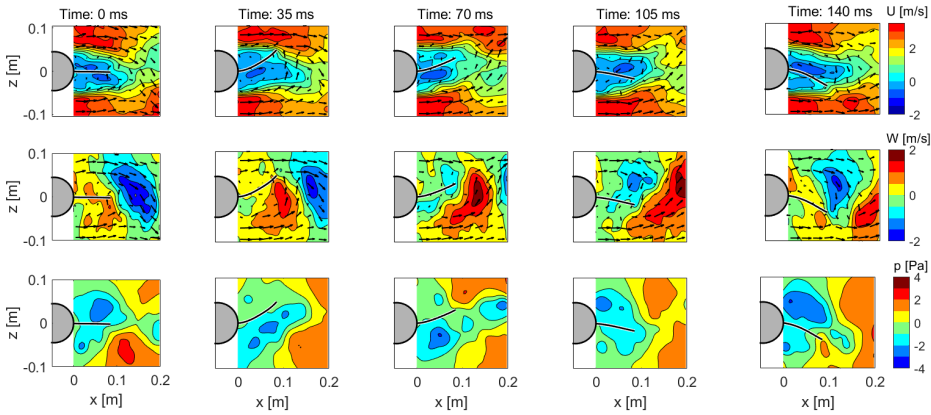
Figure 4.7: Time sequence of flow velocity and pressure after spanwise averaging. Colour contours of streamwise (top) and transverse (middle) velocity component. Bottom row: static pressure field.

Figure 4.7 (bottom row) illustrates a sequence of the pressure field time evolution. Recall that, due to the limitations of the available pressure solvers, an accurate pressure field could be calculated in the outer regions, i.e. away from the foil. Therefore, for the current visualization, the effect of the foil (imparting a small pressure discontinuity at its opposite faces) is neglected, and the pressure equation is solved in the entire measurement domain. Despite the expected errors at the vicinity of the solid interface, the pressure fields provide insights to the structure and phase of the aerodynamic forcing mechanism. The presence of low-pressure blobs, corresponding to the core of Kármán vortices, is observed, alternating from the opposite sides of the foil and travelling at the same convection speed of the vortices. During the passage of a low-pressure blob, the foil is accelerated in the direction of the vortex and continues after the vortex has passed the foil tip under the effect of inertia.

A time evolution of the computed surface pressure along the streamwise direction x
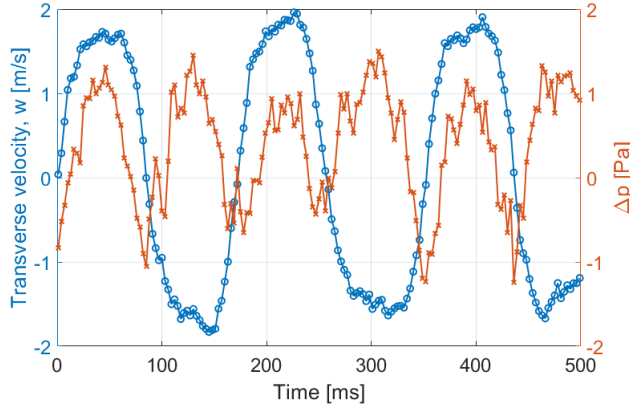
Figure 4.8: Transverse flow velocity (blue, circles) and static pressure (red, crosses) at a location downstream of the foil, averaged along the span ($x/L = 1.1, z/L = 0$).

is provided in Fig. 4.9. Note that as the foil deflects, the projection to the x-axis reduces the range to $0 < x/L < 0.9$ depending on the motion phase. Regarding the forcing, the most effective appears to occur when the low-pressure region transits from the foil mid-length ($x/L = 0.6$) to its end ($x/L = 0.9$). In this situation of maximum forcing, both the pressure load (a pulling force) and the foil velocity vector are aligned, thus resulting in a positive work performed by the flow to the foil. This mechanism is enhanced by the high-pressure regions (red orange in Fig. 4.7), which build up in the outer region when the foil is at the limit of the motion and aid to push the foil back towards the neutral position. The above effects ultimately lead to an oscillatory aeroelastic regime with pronounced periodic behaviour.
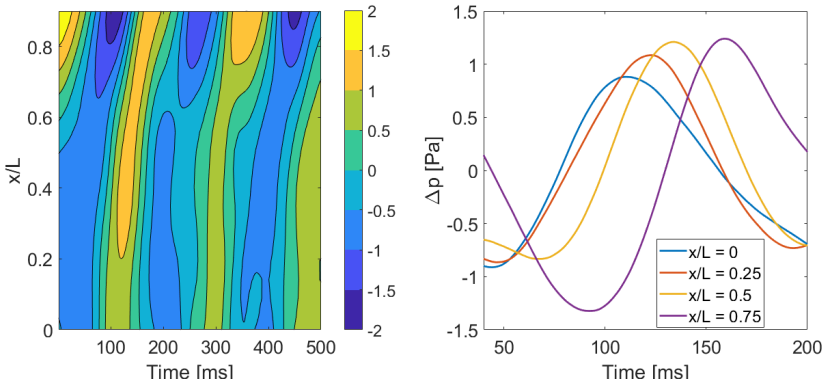
Figure 4.9: Left: time evolution map of surface pressure (in Pascals) along the normalized streamwise direction x/L. Right: time evolution of surface pressure for extracted locations $x/L = 0, 0.25, 0.5, 0.75$.

The time evolution of the foil's motion is illustrated in Fig. 4.10. Contours of position,

tiles' acceleration, and elastic force per tile are provided on the deformed shape of the foil. Position (top) and acceleration of the foil (centre) are in phase-opposition, as expected from the second derivative of an oscillatory motion. The inertia force (not shown here) is opposite to the acceleration; hence, it exhibits the same trend as the foil's displacement. Similarly, to the acceleration, the elastic force opposes to the foil position, as the deformation promotes internal stresses and moments that act against it to recover the undeformed state. This working mechanism is analogous to that of a mass-spring system in oscillation.
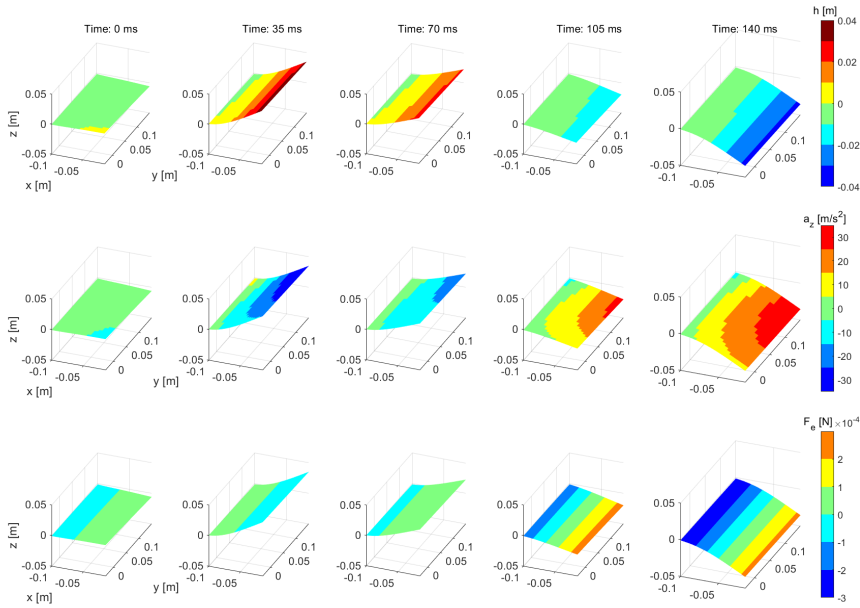
Figure 4.10: Time sequence of measured structural variables: displacement h (top), tiles' acceleration (related to the inertia forces, centre), and elastic force along z (bottom) acting on a tile of 0.5×0.5 cm^2.

Figure 4.11 illustrates the foil motion by the time evolution of three markers located at the mid-span of the foil and at 1/4, 1/2 and 3/4, respectively, of the foil's chord length. The in-phase displacement, for all positions, indicates that the foil motion is dominated by its first mode of oscillation, and a stationary wave at the frequency f_{foil} = 5.7 Hz is observed. This frequency is very close to the first natural frequency (regardless damping) of the studied configuration, $f_{1,natural}$ = 5.17 Hz. This mode of oscillations is consistent with the theory of oscillating cantilevered beams (Den Hartog, 1985), where the displacement increases more than linearly from root to tip.

4.5. DISCUSSION ON THE CLOSURE OF COLLAR'S TRIANGLE

The time-evolutions of all measured aeroelastic forces acting on tiles of 0.25 cm^2 area (0.5 cm ×0.5 cm) are presented in Fig. 4.12. The value of such forces is extracted at the three tile locations x/L = 0.25, 0.5, 0.75 (y/W = 0.5). An observation can be made of the
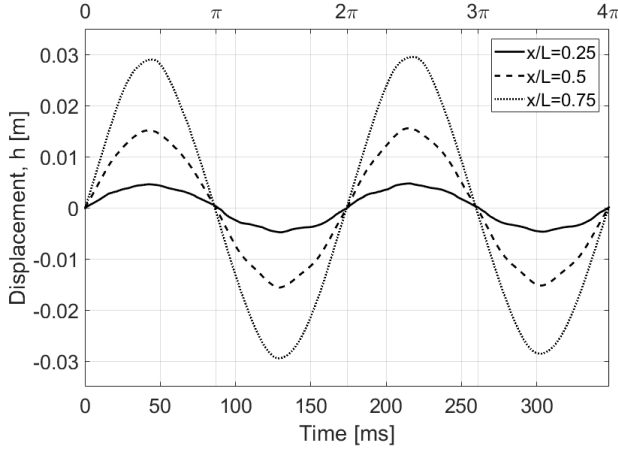
Figure 4.11: Time evolution of foil displacement at x/L: 0.25, 0.5 and 0.75, at the mid-span location ($y/W = 0.5$).

relative phase of the forces with respect to the motion of the foil. The tile's inertia force features a standing wave in-phase with the displacement h, which is consistent with the operator of second derivative between position and acceleration for an oscillatory signal. Therefore, the tile acceleration signal is in phase-opposition, (i.e. π phase-shift) to the displacement. Based on eq. 4.2, the inertia (red line in Fig. 4.12) has opposite sign to the acceleration, leading to a condition of zero phase shift (in-phase signals) between displacement and inertia force. As expected from the measurement technique, the inertia force has the lowest uncertainty of the triangle, $\epsilon_{inertia} = 6 \times 10^{-6}$ N.

The elastic force (in yellow, Fig. 4.12) should exhibit a value that is in phase opposition to the displacement and the inertia force. This behaviour is found back at $x/L = 0.75$ (Fig. 4.12-right). However, the variations in time do not feature a sinusoidal behaviour and the signal appears to be corrupted by spurious fluctuations at frequency higher than that of the primary oscillation. At points closer to the root of the foil ($x/L = 0.25$ and $x/L = 0.5$) it appears that these spurious fluctuations compromise the evaluation of the elastic force as the noise level attains the same level of the expected magnitude of the elastic force. Overall, based on error propagation through the spatial regression onto the fourth derivative of the deformation, the elastic force presents the highest uncertainty $\epsilon_{elastic} = 2 \times 10^{-4}$ N.

Finally, the aerodynamic force (shown in blue in Fig. 4.12) displays the lowest force levels among the three components and for the three locations of the foil. Differently to inertia and elastic forces, the aerodynamic force appears as a traveling wave with a different delay to the foil motion at each chord location. The latter can be also observed from the surface pressure in Fig. 4.9. This effect is explained by the convection streamwise of Kármán vortices featuring low-pressure blobs at their core. The uncertainty for the aerodynamic force resulted in $\epsilon_{aero} = 4.3 \times 10^{-5}$ N.

The condition of maximum forcing for the aerodynamic force occurs when the aerodynamic force and the foil velocity are in phase. In such condition, the alignment between the aerodynamic force and the foil velocity vectors transfers the maximum work
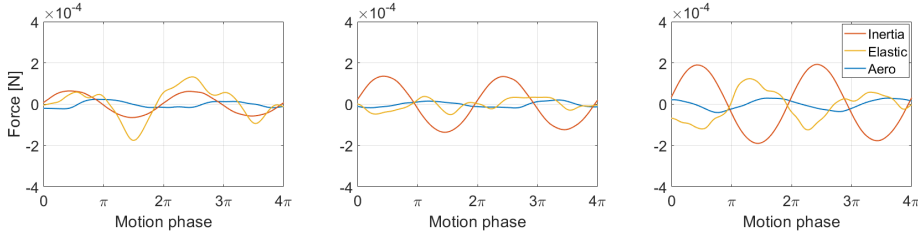
Figure 4.12: Fig. 12 Instantaneous time-evolution of aeroelastic forces at different chord locations x/L: 0.25 (left), 0.5 (centre), and 0.75 (right). Measurements at mid-span location y/W=0.5.

from the flow to the foil. Therefore, the aerodynamic force must anticipate the foil's motion (displacement) by a phase shift of about $\pi/2$ (phase quadrature). From the present experiments (Fig. 4.12) it appears that such condition is best attained around the position $x/L = 0.75$.

Once the foil reaches a steady-state oscillatory regime (of approximately constant amplitude and frequency), only a small aerodynamic force is required to maintain the system in such regime, where the sum of elastic and inertia forces conserve most of the system kinetic energy. Instead, the work produced by the aerodynamic force is dissipated by structural damping. The evaluation of structural losses, however, goes beyond the scope of the current study and is not examined further.

The closure of Collar's triangle concludes this work and is achieved by imposing the equilibrium of the aeroelastic forces. The equilibrium addresses the dominant effects along the z-component of the force vector. When uncertainties pertaining to the experimental approach and the subsequent modelling to estimate the forces are accounted for by a term ϵ_{CC}, eq. 4.1 is rewritten as:

$$F_i + F_e + F_a = \epsilon_{CC} \tag{4.9}$$

This residual was anticipated in section 4.1.4 as the Collar closure Criterion (CC), ϵ_{CC}, and quantifies how accurate the measurement of three aeroelastic forces is altogether. For the present experiments, the closure of Collar's triangle (i.e., the magnitude of the residual force, ϵ_{CC}) is evaluated for the afore-analysed tile locations. In view of the oscillatory nature of the forces, the standard deviation (STD) of the error is reported in Table 4.3 taking the inertia force as a reference for the amplitude.

Table 4.3: Collar closure criterion force and inertia force for a tile location at y/W=0.5.

	x/L = 0.25	x/L = 0.5	x/L = 0.75
STD F_i [mN]	4.4×10^{-2}	9.4×10^{-2}	13.2×10^{-2}
STD ϵ_{CC} [mN]	11.2×10^{-2}	8.7×10^{-2}	6.2×10^{-2}
STD ϵ_{CC}/ STD F_i	2.5	0.9	0.47

While the inertia force increases downstream, ϵ_{CC} increases towards the root. This is ascribed to the uncertainty of the elastic force, which appears to be maximum at the

foil's root, with the small displacements. The ratio between the Collar force and the iner-
tia force as provided in Table 4.3 can be seen as an indicator of the accuracy of the closure
of Collar's triangle of forces. It is evident that from the foil's root to approximately the half
chord (x/L = 0.5), the residual of Collar's force strongly distorts the equilibrium. As pre-
viously mentioned, this is ascribed to the large uncertainty of the elastic force associated
to the fourth spatial derivative of displacements, and the vanishing magnitude of the
inertia force close to the foil's root. Instead, towards the foil's tip (x/L ≥ 0.75), the resid-
ual tends to become a vanishing component, indicating the feasibility of Collar's triangle
closure by non-intrusive experimental means.

Aside from the uncertainty of the elastic force the hypothesis of small displacements
will require further scrutiny. When the latter assumption is not satisfied, aerodynamic
elastic and inertia forces will need to be evaluated with their full vectors and the local
orientation of the foil needs to be accounted for.

4.6. CONCLUSION

A non-intrusive measurement methodology for aeroelastic experiments based on the
Lagrangian particle tracking technique is proposed to simultaneously estimate aerody-
namic, elastic and inertial loads from a deforming model. The method relies on the
tracking of flow tracers to characterize the flow, and of surface markers to describe the
dynamics of the structure. An experiment was carried out to show the applicability of
the proposed methodology. The measurements regarded a flexible transparent foil at-
tached to a solid cylinder and interacting with the wake of the latter. Both the flow trac-
ers (neutrally-buoyant HFSB) and surface markers applied onto the panel were tracked
in time with a single optical tomographic system.

The results show the potential of evaluating the aeroelastic forces from Lagrangian
particle tracking measurements of the flow tracers and the markers on the flexible struc-
ture. The inertia forces were successfully evaluated via time-derivation of the markers'
displacements. The pressure on the foil surface was obtained extrapolating the solution
of the Poisson problem from the outer flow field to the foil. The elastic forces required
evaluation of the fourth spatial derivative of the displacement and turned out to be the
most challenging quantity to determine.

Flow analysis results show that pressure blobs associated with the Kármán vortices
determine the unsteady aerodynamic forcing. A phase shift exists between such external
loading and the inertial and elastic response.

The Collar closure criterion is introduced that considers the residual of the force
equilibrium equation as a measure of the accuracy of the overall experiment. The cri-
terion yields unfavourable results close to the foil root where displacement and acceler-
ation are vanishing. At the foil trailing edge, a consistent combination of the aeroelastic
forces is observed, indicating the feasibility of the present optical diagnostic approach
for aeroelastic systems characterisation.

5

FLUID-STRUCTURE INTERACTION OF CYLINDER-FOIL CONFIGURATION

The more sand has escaped from the hourglass of our life,
the clearer we should see through it.

Niccolo Machiavelli

In this chapter, an evaluation of the previous test case, cylinder-foil configuration,is carried out in more detail. Focus is switched from forces at the foil surface to interaction between the cylinder wake and the surface deformation. Different regimes are identified attending to the behavioral motion of the flexible structure. To further understand the coupling, the wake of the model is studied and compared to clean cylinder wake. A statistical analysis is performed on both configurations. Moreover, Proper Orthogonal Decomposition (as seen in Chapter 2) is applied and shows the difference in the most energetic modes and how these are affected by the flexible foil.

5.1. INTRODUCTION

The current chapter aims to provide an experimental characterization of the flow around a cylinder with a flexible splitter plate. In particular, we consider different aeroelastic regimes to investigate how the wake dynamics affects the motion of the flexible plate and whether the plate's motion alters the wake flow field. Lagrangian particle tracking is employed to track flow tracers and surface markers simultaneously. The behaviour of the flexible splitter plate is classified into different regimes depending on the amplitude and three-dimensional shape of the motion. Statistical analyses are performed to determine the effect of the flexible splitter plate on the dynamics of the cylinder wake.

5.2. EXPERIMENTAL APPARATUS AND PROCEDURE

The experimental setup for this study is very similar to the previous chapter, 4. A summary is provided hereafter for completeness.

5.2.1. FLOW FACILITY AND MODEL

The experiments were conducted at the Aerodynamics laboratory of TU Delft, in an open-jet open-return wind-tunnel of 600×600 mm^2 exit cross-section. A cylinder of 90 mm diameter was installed vertically with a flexible transparent foil attached along the rear mid-plane. The foil (size 105×200 mm^2 in stream and span directions) undergoes a 2D motion excited by the periodic shedding of vortices in the Kármán wake of the cylinder. The maximum amplitude of oscillations in a 2D regime is observed at a free stream velocity $U_\infty = 2.25$ m/s ($Re = 1.35 \times 10^4$), where experiments are conducted. The foil optical transparency allowed to track flow tracers at both sides of it even when looking from only one side. However, the amount of detected flow tracers behind the foil was slightly lower than in the region with direct view, as a result of incomplete light transmission through the foil. For the measurement of the foil kinematics, a regular pattern of 210 bright surface markers was applied to the foil. The markers had an average diameter $d_m = 0.8$ mm and a pitch $p_m = 1$ cm. The overall experimental setup is illustrated provided in Fig. 5.1.

Table 5.1: Physical properties of the flexible foil and tile.

Dimensions	Thickness, T (mm)	0.25
	Length, L (mm); l (mm) (tile)	95, 10
	Width, W (mm); w=l (mm) (tile)	200, 10
	Aspect ratio, L/W	0.475
Material	Density, ρm (kg/m^3)	1290
	Young modulus, E (GPa)	1.0
	Poisson ratio, v (-)	0.3
Interaction parameters	Mass ration, m* = $(\rho_m/\rho_f)\cdot$ (T/L) (-)	2.77
	Cauchy number, Ca = $(\rho_f U^2 W L^3)$/EI (-)	7.8

Figure 5.1: Experimental arrangement with cylinder and foil and system of coordinates. Illumination (by LED units) and tomographic imaging system (four CMOS cameras).

5.2.2. Flow measurement

As described in Chapter 4, the flow was seeded with neutrally buoyant sub-millimetre (mean diameter d≈350 μm) helium-filled soap bubbles, released by an in-house 200-generator seeding rake installed in the tunnel settling chamber. The nominal production rate of the flow tracers is 6Ö10^6 bubbles/s, resulting in a seeding concentration of 10 bubbles/cm^3 for a freestream velocity U_∞=2.25 m/s at the test section (seeded stream-tube of 60 × 25 cm^2). For the current experiment, only 100 generators were operated to reduce the seeding concentration to 5 bubbles/cm^3, so as to satisfy the condition on the maximum number of particles per pixel (ppp = 0.05) for 4-camera tomographic systems (Elsinga et al., 2006).

A measurement volume of 22 × 40 × 20 cm^3 was illuminated vertically (span-wise direction) by two LaVision Flashlight 300 LED banks located under the test section. In the current experiments, flow tracers were measured at both sides of the transparent foil. A mirror was installed at the top plane of the test section to increase the light intensity in the measurement volume, thus allowing to identify the tracer particles also in the region behind the foil. The imaging system consisted of four high-speed cameras (1024 × 1024 pixels, 12 bit, 20 μm pixel pitch) mounted in a tomographic configuration 90 cm away from the foil, as shown in Fig. 5.1. The cameras subtended an aperture of approximately 30 degrees. Details of the optical system used in the experiments are summarized in Table 5.2.

The image acquisition and processing were conducted with the LaVision *Davis 10.0.5* software. Sets of 5000 images were recorded in continuous mode at a rate of 1 kHz. For the calibration process, a geometrical calibration (Soloff, Adrian, and Liu, 1997) was fol-

lowed by the volume self-calibration (Wieneke, 2008) and optical transfer function determination (OTF calibration, Schanz et al., 2012). The surface markers were visually distinguished from the flow tracers based on their distinct optical characteristics. In order to track most fluid tracers (spherical bubbles) and most structural markers (2D flat bright circles), the volume self-calibration and the OTF calibration were performed separately with clean runs containing only one tracer type. Both the flow tracers' velocities and the foil markers motions were evaluated by means of the Shake-the-Box Lagrangian Particle Tracking (LPT) algorithm (Schanz, Gesemann, and Schröder, 2016). Based on the work of Bhattacharya and Vlachos (2020), particle location uncertainty is expected below 0.3 pixels for IPR-based reconstructions, and further decreases to 0.1 pixels when the particles are track over multiple time instants with the STB algorithm (Sciacchitano, Leclaire, and Schroeder, 2021).

Table 5.2: Optical system information.

Illumination	2 × LaVision Flashlight 300 LED
	2 × Photron FastCam SA1.1 (1024x1024 pixels, 5400 fps)
Cameras	1 × Photron FastCam SA5 (1024x1024 pixels, 7000 fps)
	1 × HighSpeedStar 8 (1024x1024 pixels, 7000 fps)
Imaging	3 × Objectives Nikkor 50 mm - f# 1/11.2
	1 × Objectives Nikkor 60 mm - f# 1/11.2
Acquisition frequency	1000 Hz

Figure 5.2: Imaged aeroelastic regimes: (I) low oscillations, (II) resonance, (III) chaotic, and (IV) bi-stable. White dashed line at neutral position of the foil, z = 0.

5.3. AEROELASTIC REGIMES OF FLAPPING FOIL

The behaviour of the flexible foil was studied for a range of free-stream velocities in order to explore the different aeroelastic regimes of the current configuration. Four different regimes were identified for the current foil length, L/D=1.1, similarly to De Nayer et al.

(2014) for the case L/D=2.7. The measured regimes are observed in Fig. 5.2 & 5.3 and explained in the following points:

1. Low-amplitude oscillations: the first regime is characterized by small oscillations with low amplitude, below 6 cm. The flow pressure barely overcomes the stiffness of the structure.

2. Bending resonance: the second regime encompasses large two-dimensional oscillations at a constant frequency. The sudden growth in amplitude with respect to the neighbouring velocities is related to the resonant frequency of the foil. This regime is characterized by the coalescence of two frequencies: the vortex shedding frequency in the cylinder's wake, and the natural frequency associated with the first bending mode of the foil.

3. Chaotic: When increasing further the free-stream velocity, the foil enters a regime with a chaotic motion characterized by three-dimensional deflections. The amplitude of the flapping motion is strongly reduced as seen in Fig. 5.3.

4. Bi-stable. This regime is characterized by a locked state at one of the extreme positions, where the foil solely vibrates around that location (see Fig. 5.2-IV). Eventually, fluctuations in the flow may disturb the equilibrium position strongly enough that the foil moves to the other extreme and oscillates around this new equilibrium position.
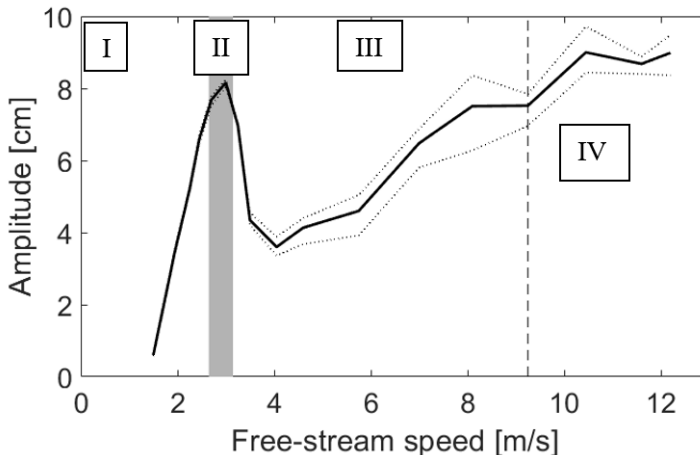
Figure 5.3: Average amplitude of the flapping foil motion at different free-stream speeds. Four different regimes are identified: (I) low oscillations, (II) resonance, (III) chaotic, and (IV) bi-stable. Dotted lines represent maximum and minimum amplitude along the foil span.

5.4. WAKE DYNAMICS

In this section, we analyse the wake dynamics for two aeroelastic regimes, bending reso-
nance (II) and chaotic (III). The effect of the flexible splitter plate is studied via compari-
son with the cylinder flow without any foil. The fluid-structure interaction in the chosen
regimes will be examined by flow wake statistics and modal decomposition. Cylinder
flows at subcritical regime exhibits a predominantly 2D wake with span-wise turbulent
fluctuations below 10% U_∞ (Coutanceau and Defaye, 1991). Therefore for sake of con-
ciseness, the statistical and POD analyses will focus on the middle x-z plane. Results
from the latter will determine the relevance of studying 3D coherent structures in future
work.

Figure 5.4: Time-averaged field (left) and standard deviation (right) for the stream-wise velocity component,
u, in m/s. Cylinder flow above, and cylinder-foil flow below for Re=33,000.

5.4.1. REGIME II: (QUASI) 1-WAY COUPLING

STATISTICAL ANALYSIS

A statistical analysis is conducted on the fine-gridded data for a total of 2000 three-
dimensional fields, measured during 2 seconds. Figure 5.4 shows the time-average and
standard deviation of the stream-wise velocity component for the two configurations,
namely without (top) and with (bottom) the foil. The downstream limit of the foil is in-
dicated by a dashed black line. In both cases, as expected a recirculation bubble is found
in the back of the cylinder, confined by the two separating shear layers at the cylinder's
top and bottom. Slight differences are seen in the recirculation region, where a stronger
backflow is present in the absence of the foil. When looking at the velocity fluctuations,
differences in the locations and strengths of the maximum fluctuations regions are no-
ticed. In the absence of the foil, maximum fluctuations regions are located downstream
of the cylinder, x = 0.75 m, and caused by oscillations of the wake. However, when the

foil is present, it obstructs the flow in proximity of the cylinder, thus causing lower velocity variations. As a consequence, the high fluctuation regions move downstream, x = 0.1 m, and decrease their strength. The effect of the foil on the cylinder near wake can be also observed in the transverse velocity component in Fig. 5.5. The time-averaged field presents two main counter-sign regions, which represent the containment of the recirculation bubble. In presence of the foil, these two regions shift downstream, thus causing a more elongated recirculation bubble. In addition, velocity fluctuations in the vicinity of the cylinder are strongly diminished by the presence of the foil. Despite the latter discrepancies concerning the flow in proximity of the cylinder, the two configurations return very similar flow statistics from x > 0.125 m, indicating that in this region the foil has only minor effects on the flow field.
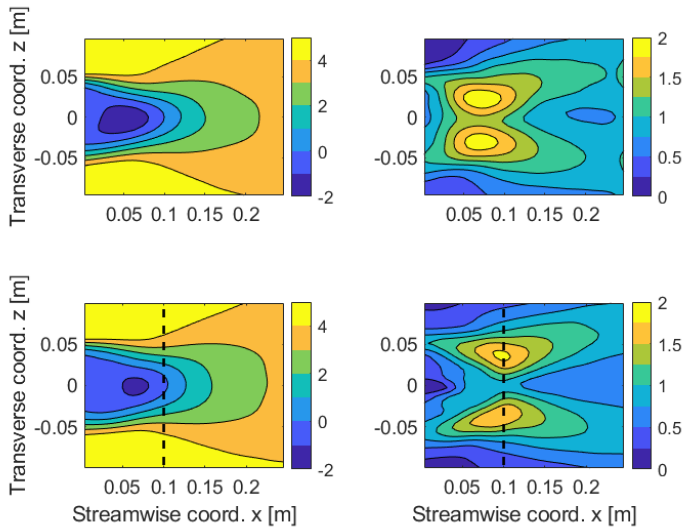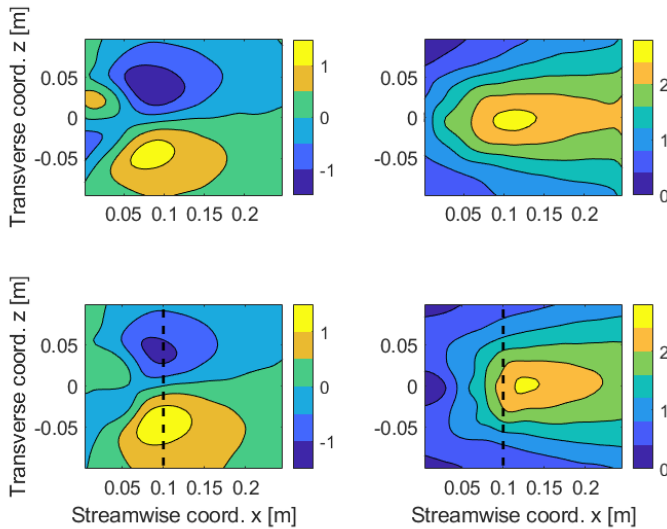

Figure 5.5: Time-averaged field (left) and standard deviation (right) for the stream-wise velocity component, u, in m/s. Cylinder flow above, and cylinder-foil flow below for Re=33,000.

The aforementioned effects are visualized in figure 5.6, too. The latter displays the histograms of the three components of the velocity throughout the measurement domain for the time length of the dataset (2000 time samples). The most notable difference is the null stream-wise velocities appearing for the cylinder-foil configuration. As seen in the time-averaged flow, the foil disrupts the backflow region, by obstructing the flow around it. As a consequence, a region of velocity close to zero is formed in proximity of where the foil is clamped. This effect is noticed also for the span-wise and transverse velocities, which show narrower distributions with more samples at velocities close to zero. Despite these discrepancies, overall the similarity between the two configurations is very high, indicating a low effect on the cylinder wake when installing the flexible foil.
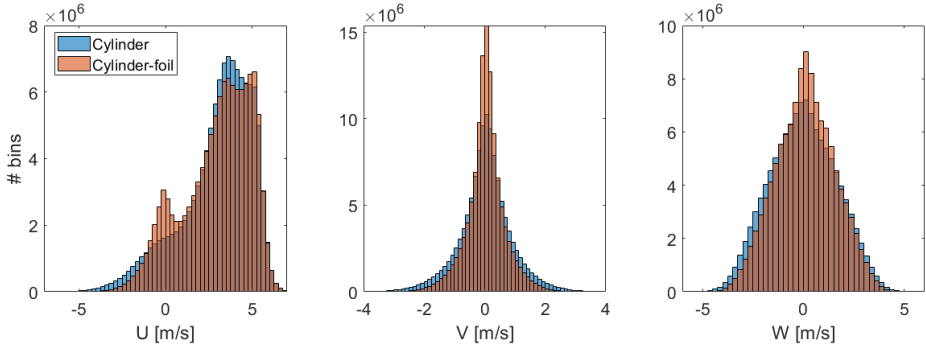
Figure 5.6: Histograms of velocity components, stream-wise (left), span-wise (centre), and transverse (right), throughout the entire measurement domain and all time samples for Re=33,000.

PROPER ORTHOGONAL DECOMPOSITION

A POD analysis was conducted to investigate the most dominant modes of the stream-wise and transverse velocity components of the mid x-z plane. Figure 5.7 displays the energy fraction of the 10 most dominant modes of both the cylinder flow, in blue, and the cylinder-foil flow, in red. Both configurations show a flow dominated by two modes, which accumulate more than 80% of the total energy. The energy trend of the modes for the two velocity components analysed is very similar between the two configurations, deviating less than 5 % from each other. This indicates that the large scale coherent motion of the cylinder flow, i.e. Kármán vortex wake, is unaffected by the presence of the flexible foil at this regime. However, the energy content is not sufficient to compare the modes between the two configurations. To investigate the spatial description of the most dominant modes, Fig. 5.8 shows the modes shapes for modes 1 – 4 for the stream-wise velocity component for the cylinder flow (above) and cylinder-foil flow (below). The rear limit of the foil is illustrated with a dashed black line.
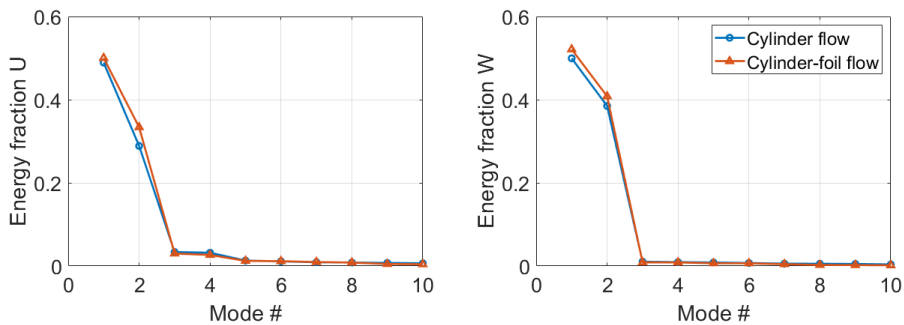
Figure 5.7: Energy distribution over the modes of the stream-wise velocity, left, and the transverse velocity, right. Cylinder flow in blue and cylinder-foil flow in red for Re=33,000.

Focusing the attention to the first pair of modes (1-2), they are similar for both configurations. The two modes appear to be orthogonal to each other and together they

describe the rollup and convection of the Kármán vortices. In the cylinder-foil configuration, two additional "blobs" appear in mode 1 in proximity of where the foil is clamped. These are ascribed to the obstruction caused by the foil, and limit the velocity fluctuations in this region. On the other hand, modes 3 and 4 reveal different phenomena for each configuration. Given their low energy contribution, they will be left out of the discussion for the sake of conciseness.
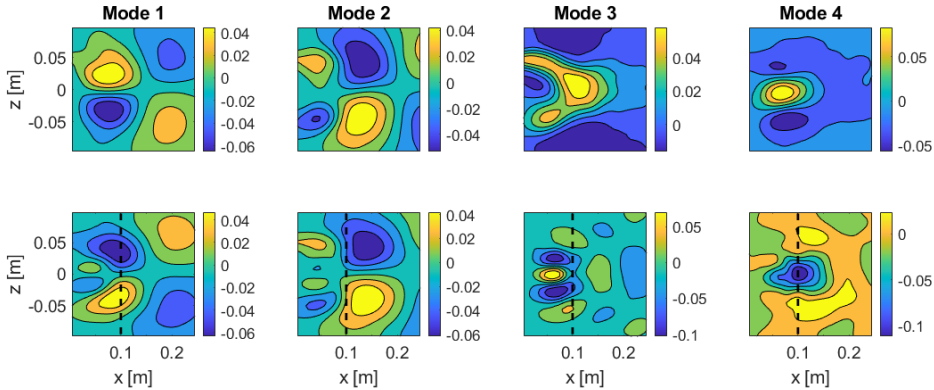
Figure 5.8: Mode shapes of POD modes 1 - 4 (from left to right) of the stream-wise velocity component u for the cylinder flow (above) and the cylinder-foil flow (below) for Re=33,000.
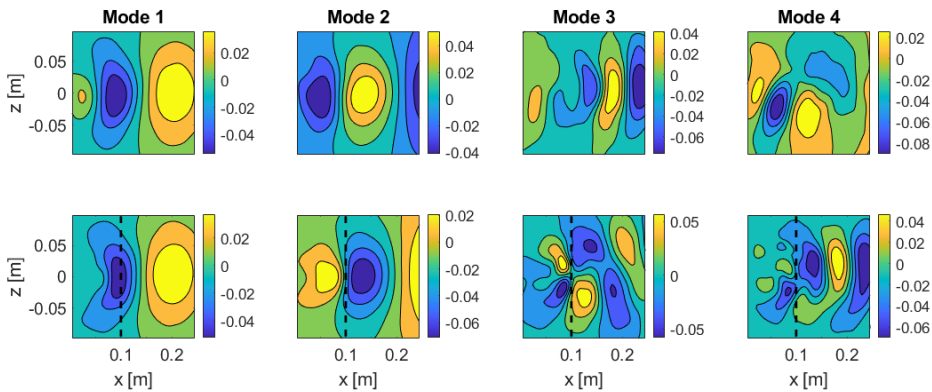
Figure 5.9: Mode shapes of POD modes 1 - 4 (from left to right) of the transverse velocity component w for the cylinder flow (above) and the cylinder-foil flow (below) for Re=33,000.

The same behaviour is observed for the transverse velocity modes depicted in Fig. 5.9. The dominant pair of modes (1-2) show the convection of the strong positive and negative regions of transverse velocity as the vortexes of the cylinder wake convect downstream. Some differences between the configurations are observed in the region where the foil is clamped to the cylinder. Here, the cylinder-foil configuration exhibits lower velocities both in mode 1 and in mode 2, because the clamped foil hinders the transverse movement of the flow. As for the stream-wise component, modes 3 and 4 are not

the same modes for the two configurations, yet they show a rather chaotic distribution of smaller scales to the first pair.

Overall, the most dominant modes of both configurations describe the same phenomena, i.e. the characteristic vortex street of a cylinder wake. Thus, in this aeroelastic regime, the flexible foil affects the flow only in the region in proximity of the cylinder, whereas the wake at x > 0.1 m is mostly unaffected. Therefore, the fluid-structure coupling mechanism is considered 1-way, because the flow clearly affects the structural motion, whereas the foil has only minor effects on the flow.

5.4.2. TIME-RESOLVED ANALYSIS

The final part of the analysis is based on instantaneous data. A time series of the transverse velocity component at a point in the wake is given in Fig. 5.10 (left) for the two configurations. The frequency content of the latter signal is displayed by the power spectral density in figure 5.10 (right). From the instantaneous signal, one can see the cylinder flow behaves predominantly periodic with a rather low standard deviation. The latter behaviour is also reflected at the strong peak of the PSD at the frequency of the cylinder shedding, and then decreasing towards higher frequencies. The addition of the flexible foil to the cylinder does not change the overall picture. The flow displays a very similar periodicity in strength and frequency. The dominant frequency of the flow corresponds to $f \approx 9.8$ Hz. The measured flow dominant frequency agrees well with the characteristic frequency for cylinder shedding wakes in the sub-critical regime, $St \approx 0.2$ (Williamson, 1996), apparently, unaffected by the presence of the flexible foil. Differences between the configurations can be spotted in the high frequency content of the signal, which decreases with the foil. Thus, the foil acts as a turbulence damper by decreasing the energy content of the smaller scales.
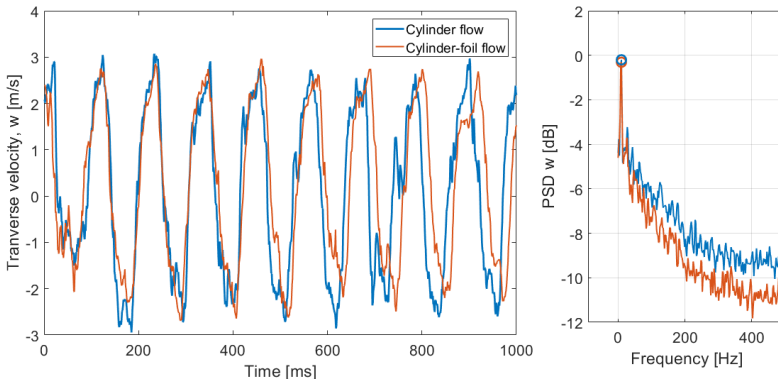
Figure 5.10: Time series of instantaneous transverse velocity (left), and its power spectral density (right), for the two configurations at Re=33,000. Signal extracted at the point x = 0.2 m, y = 0, z = 0.

The volumetric measurements allow to infer the three-dimensional effect of the foil on the wake structures. Figure 5.11 shows three-dimensional iso-surfaces of negative (red) and positive (blue) transverse velocity for the studied configurations. Velocity struc-
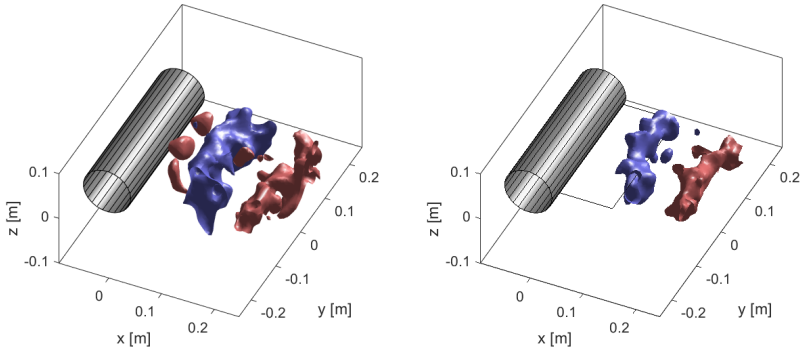
Figure 5.11: Iso-surfaces of instantaneous transverse velocity, w=-2.5 m/s in red and w=2.5 m/s in blue, for the cylinder flow (right) and cylinder-foil flow (left) at Re=33,000. Foil at equilibrium position given as reference.

tures elongated along the span are visualized, as a result of the cylinder vortex shedding. Note that the slight differences in size between the configurations structures could be due to the instantaneous sample itself. Despite that fact, the presence of the foil does not appear to affect the span coherency of the structures throughout the domain. Only the near region to the foil root presents some effect as suppression of smaller structures, in accordance to what is shown in the modes 1 and 2 of Fig. 5.9.

Figure 5.12: Time-averaged field (left) and standard deviation (right) for the stream-wise velocity component, u. Cylinder flow on the top, and cylinder-foil flow below for Re=66,000.

5.4.3. REGIME III: TWO-WAY COUPLING

The case concerning the full interaction between the cylinder wake and the flexible foil is investigated at free stream velocity $U_\infty = 11$ m/s and Reynolds Re=66,000.

STATISTICAL ANALYSIS

The time-average and standard deviation of the stream-wise, span-wise, and transverse velocity components are plotted in figures 5.12, 5.13, and 5.14 respectively, for the cylinder and cylinder-foil configurations. The cylinder flow at the current regime (Re=66000) shows a similar pattern to the previous case (Re=33000). The time-average stream-wise flow displays a recirculation region; a region of high velocity fluctuations, symmetrical with respect to z = 0, is located at the end of the recirculation bubble. The addition of the foil changes some of the aforementioned features. The backflow becomes stronger and the recirculation bubble is elongated downstream. Furthermore, the fluctuations have a single maximum at the end location of the flexible foil. The fluctuation field is completely altered with increased fluctuations along the wake. The span-wise and transverse velocity too, in figure 5.13 and 5.14, show some disagreement between the two configurations. The span-wise component displays a strong negative peak for the circular configuration that is broaden and moved downstream when including the foil. In addition, the span-wise fluctuations grow considerably just downstream of the foil trailing edge, implying some energy transfer to this component. The time-average w contours, as for Re=33000, present a negative-positive pair of regions representative of the edges of the recirculation bubble. However, the elongation of the latter for the cylinder-foil configuration causes a downstream shift of these two flow features. As a result, the peak of the transverse fluctuations is also displaced downstream, matching the location of the time-averaged features.
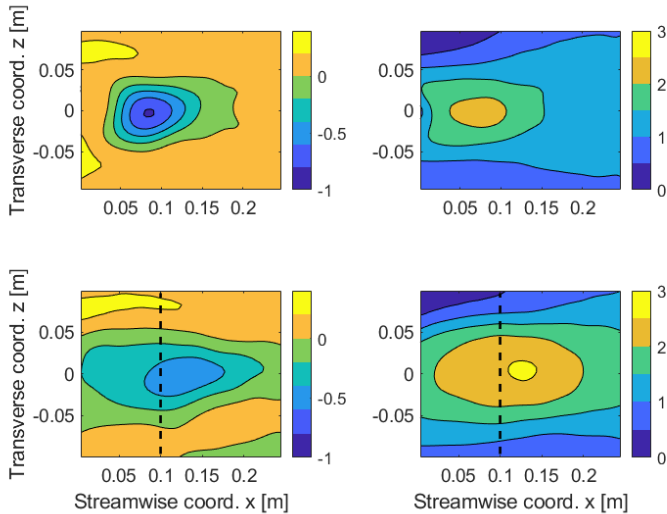
Figure 5.13: Time-averaged field (left) and standard deviation (right) for the span-wise velocity component, u. Cylinder flow on the top, and cylinder-foil flow below for Re=66,000.

Some of the discrepancies observed in the time-averaged flows are noticeable in the histograms of the velocity components, see figure 5.15. First, the stream-wise component shows an increase of the number of negative vectors when the foil is present, due to the longer and stronger backflow region. The latter has also the effect of extending the high-velocity regions at the sides of the cylinder, thus increasing the number of vectors at speeds larger than the free-stream values. Given the longer recirculation region, the histogram of transverse velocities shows a more prominent peak at null velocities. For the span-wise component, contrarily to the resonant case, the splitter foil has the effect of increasing the fluctuations, acting as an exchange of energy between the transverse and the span-wise directions; as a consequence, a broader span-wise velocity distribution is retrieved.
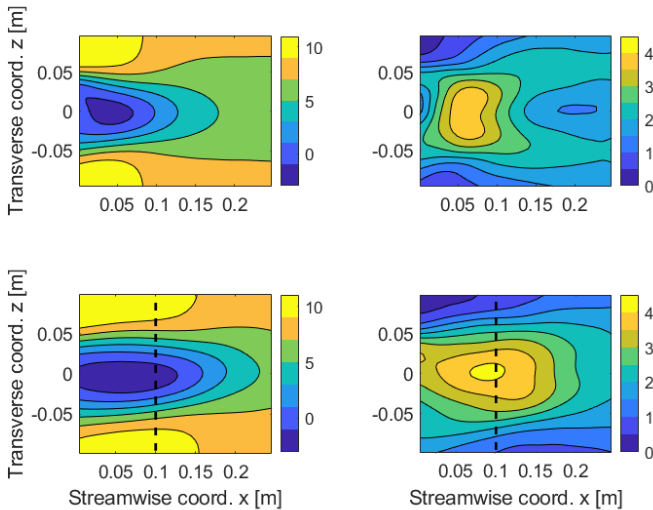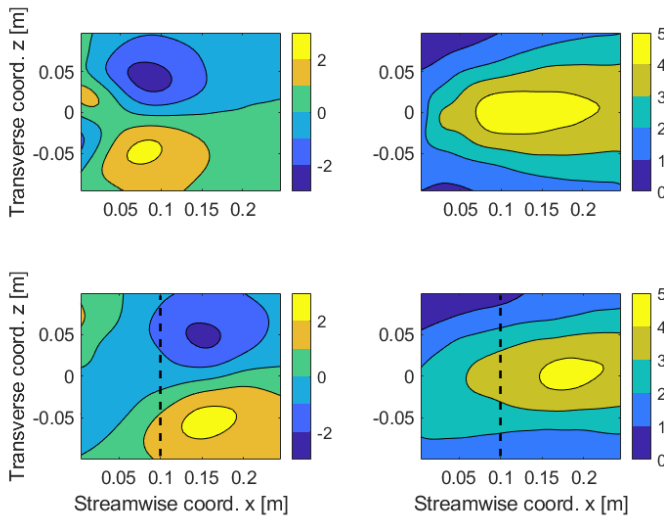

Figure 5.14: Time-averaged field (left) and standard deviation (right) for the transverse velocity component, w. Cylinder flow on the top, and cylinder-foil flow below for Re = 66,000.

PROPER ORTHOGONAL DECOMPOSITION

As for the other resonant regime, the most dominant modes were obtained from a POD analysis of the stream-wise and transverse velocity components of the mid x-z plane. Figure 5.16 displays the energy fraction of the 10 most dominant modes of both the cylinder flow, in blue, and the cylinder-foil flow, in red. Differently to the resonant regime, the distributions of modes change notably between the configurations for both velocity components. The cylinder flow still exhibits two dominant modes that capture more than 70% of the energy, which are representative of the Kármán vortex shedding. However, for the cylinder-foil case, the stream-wise component appears to have a single dominant mode and an energy distribution that decreases evenly for the remaining modes (2-10). For the transverse component, the first pair of modes accumulate 40% less energy
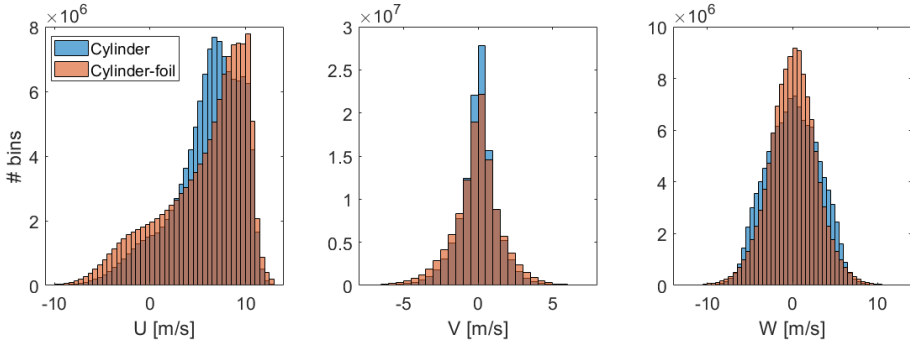
Figure 5.15: Histograms of velocity components, stream-wise (left), span-wise (centre) , and transverse (right), throughout the entire measurement domain for Re=66,000.

for the cylinder-foil flow. In the current scenario, mode shapes are necessary to identify the different modes and relate them between the two configurations.
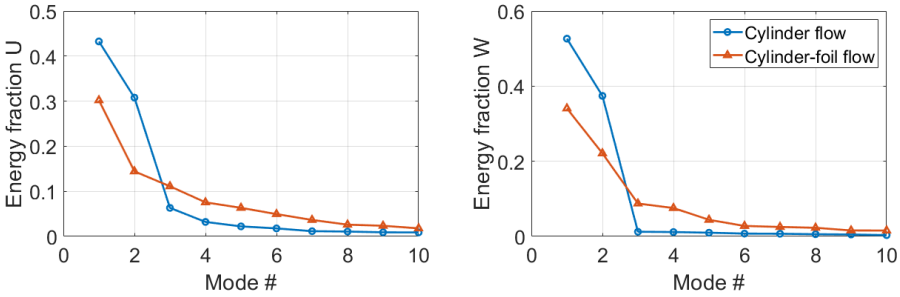
Figure 5.16: Energy distribution over the modes of the stream-wise velocity, left, and the transverse velocity, right. Cylinder flow in blue and cylinder-foil flow in red for Re=66,000.

The stream-velocity most dominant modes are displayed in figure 5.17. Mode pair 1-2 for the cylinder flow show alternating positive-negative regions originating from the convection of the shedding vortexes. These orthogonal modes appear to be in quadrature and reflect the same phenomena, i.e. Kármán street. The latter modes are very similar to the cylinder modes of the resonant regime, $Re = 33000$, as the flow is yet in the subcritical regime, $Re < 3 \times 10^5$ (Coutanceau and Defaye, 1991). On the other hand, when the foil is added, the first dominant modes do not conform a coherent pair anymore. Mode 1 seems to show the same alternating regions originated from the shedding vortexes. However, the mode features are bigger and they are no longer fully symmetric with respect to the cylinder. Mode 2 distinguishes a big structure around the foil downstream of the cylinder, related to the recirculation bubble. Moreover, modes 3 and 4 of the cylinder-foil resemble the first pair of the cylinder flow, showing similar alternating structures linked to the cylinder shedding. The latter structures in mode 3 are considerably distorted in the neighbouring region of the foil, and for mode 4, the symmetry is noticeably affected.
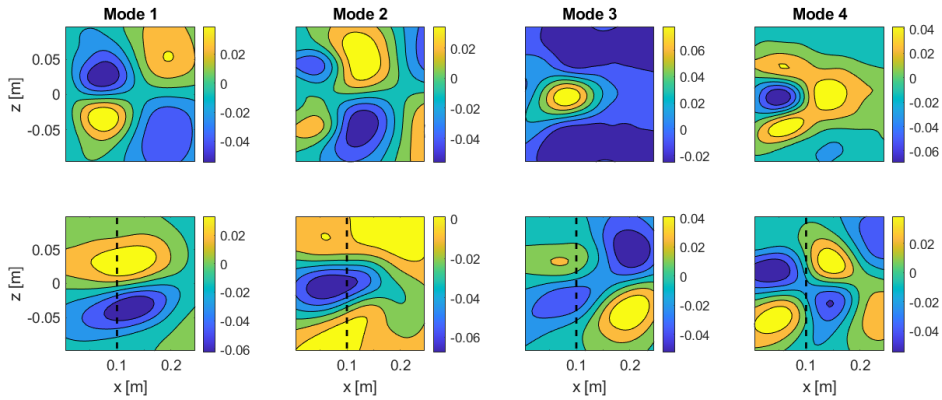
Figure 5.17: Mode shapes of POD modes 1 - 4 (from left to right) of the stream-wise velocity component u for the cylinder flow (above) and the cylinder-foil flow (below) for Re=66,000.
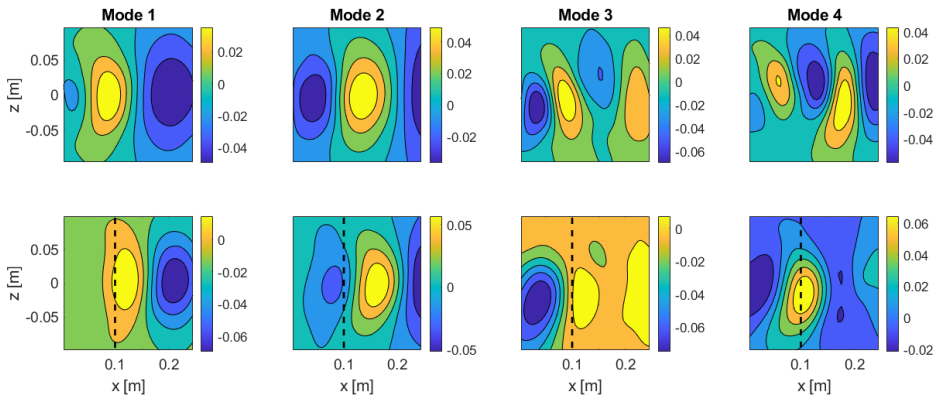
Figure 5.18: Mode shapes of POD modes 1 - 4 (from left to right) of the transverse velocity component w for the cylinder flow (above) and the cylinder-foil flow (below) for Re=66,000.

Figure 5.18 shows the most dominant modes for the transverse velocity component. In contrast to the stream-wise component, the phenomena described by the most dominant pair coincides for both configurations, yet with slight differences. The latter mode shapes, which are perpendicular to each other, exhibit alternating positive and negative regions produced by the shedding vortexes. For the cylinder-foil case, the intensity of the modes is strongly attenuated at x/L<1, indicating that the presence of the foil greatly affects the flow in this region. On the other hand, modes 3 and 4 seem to reflect different phenomena for each configuration. While for the cylinder flow the latter modes show higher harmonics of the first pair, the cylinder-foil modes display irregular shapes not straightforward to interpret.

TIME-RESOLVED ANALYSIS

Finally, a time series of the transverse velocity component at a point in the wake and its frequency content is displayed in figure 5.19. Similarly to the previous case, the cylinder flow (in blue) shows a strongly periodic signal with a dominant frequency at f = 17.6 Hz, associated to the Kármán vortex street (Williamson, 1996). However, for the cylinder-foil configuration, the presence of the foil breaks the clear periodicity of the signal, implying a considerably lower peak on the Kármán vortex frequency. The loss of energy at the latter frequency is distributed along the spectrum to the smaller scales, opposite to the effect of the foil at lower Reynolds.
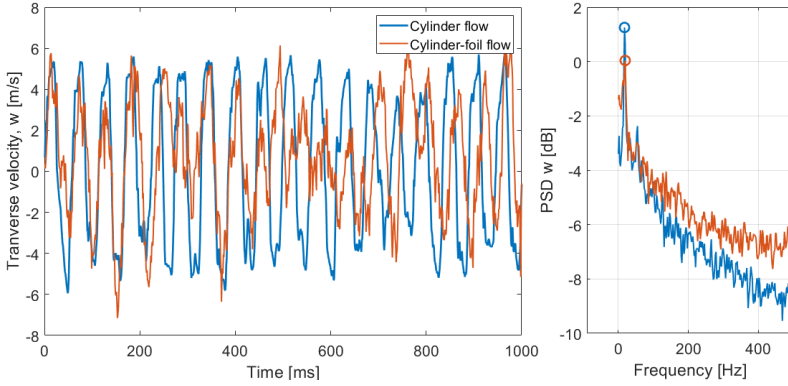
Figure 5.19: Time series of instantaneous transverse velocity (right), and its power spectral density (left), for the two configurations at Re=66,000. Signal extracted at the point x = 0.2 m, y = 0, z = 0.
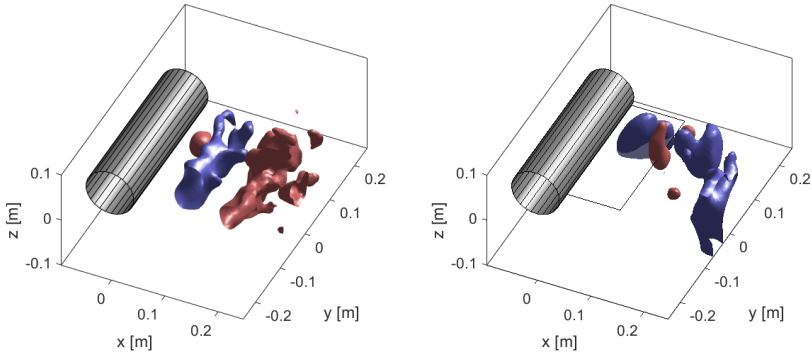
Figure 5.20: Iso-surfaces of instantaneous transverse velocity, w=-4.5 m/s in red and w=4.5 m/s in blue, for the cylinder flow (right) and cylinder-foil flow (left) at Re=66,000. Foil at equilibrium position given as reference.

Regarding the three-dimensional description of the flow, figure 5.20 shows iso-surfaces of negative (red) and positive (blue) transverse velocity for the cylinder flow (right) and cylinder-foil configuration (left). As for lower Reynolds, the cylinder flow displays long

structures parallel to the cylinder, caused by the span-wise vortexes from the shedding. For the current case, the presence of the foil has a significant impact on the instantaneous flow. The latter does not present span-wise coherence anymore, resulting in an apparently random distribution of structures. Although, the representation comprises the information a single time sample, the phenomenon by which the foil disrupts the cylinder shedding is also supported by the time-series in figure 5.19. Overall, the presence of the foil affected extensively the wake dynamics, changing the energy distribution of the underlying phenomena. Therefore, the fluid-structure coupling mechanism is considered 2-way because the flow affects the foil's motion, which in turns modifies the flow field.

5.5. CONCLUSIONS

The present chapter describes an experimental study on the flow around a flexible foil attached to a cylinder. LPT is performed on surface markers and flow tracers to measure the effect of the flexible foil on the flow around it, i.e. the cylinder wake. Several regimes of foil motion were imaged and identified in the range of free stream velocities $10^4 < Re < 10^5$. Based on the amplitude and the span-wise coherence of the plate motion, the regimes were classified into 4 categories: low oscillations, resonance, chaotic, and bi-stable. A statistical analysis was carried out for two aeroelastic regimes, the resonant and the chaotic. Proper Orthogonal Decomposition was applied to study the most dominant modes from each flow. Based on the latter analyses, two different coupling mechanisms were identified pertaining to the different aeroelastic regimes. For the resonant regime, the presence of the trailing foil did not disrupt the predominant two-dimensional motion. This regime occurs when the frequency of the vortex shedding coincides with the first natural frequency of the foil, corresponding to the first bending mode. Overall, the results showed a one-way coupling between the flow and the foil, meaning that the motion of the foil was driven by the dominant features of the flow, whereas the flow was mostly unaffected by the presence of the foil. Slight differences between the clean cylinder flow and the cylinder-foil flow, especially at the root of the foil, can be explained by the weak structural damping of the foil. Conversely, the chaotic regime is an example of full interaction, i.e. 2-way coupling between flow and structure. The cylinder flow at that freestream speed displayed a predominant two-dimensional flow, characteristic to sub-critical cylinder flow below $Re < 3 \times 10^5$. The results showed that the addition of the foil completely disrupted the cylinder wake by enhancing the span-wise flow oscillations and so, the three dimensional features of the wake. The present work focused solely on the middle x-z plane and spotted relevant mechanisms by which the cylinder-foil configuration enhances flow three-dimensionality. Next steps must analyse further the effect of the flexible foil on the 3D wake structures.

6

TIME SEGMENT ASSIMILATION (TSA)

Excellence endures and sustains.
It goes beyond motivation into the realms of inspiration.

Azim Premji

As introduced in Chapter 2, reconstructing accurate velocity fields from sparse data requires methods to grid the information of tracked particles. The coming chapters deal with two different, yet similar, data assimilation techniques: VIC-TSA, in this chapter, and VIC+ approaches adapted for FSI problems, in Chapter 7.

Similar to the VIC + technique, VIC-TSA makes use of the vortex-in-cell paradigm to produce estimates of the flow state at locations and times other than the measured ones. The working principle requires time-resolved measurements of the particles' velocities during a finite time interval. The work investigates the effects of the assimilated length on the spatial resolution of the velocity field reconstruction. The working hypotheses of the VIC-TSA method are presented here along with the numerical algorithm for its application to particle tracks datasets. The VIC-TSA spatial resolution is evaluated first via a synthetic test case; a 3D sine wave lattice is reconstructed at different values of the particles concentration. Large-scale PIV experiments in the wake of a circular cylinder at $Re_d = 27,000$ are used to evaluate the method's suitability to real data, including noise and data outliers.

6.1. INTRODUCTION

The present section discusses the VIC-TSA data assimilation principle. A first-principle analysis based on geometry and kinematics lays the foundations of the operation regimes for this technique. Furthermore, the mathematical background and the numerical algorithm are presented and discussed. The features and performances of the VIC-TSA technique are based on the analysis of a simplified synthetic PTV experiment, using a steady 3D lattice of sinusoids, following the approach of the 4th PIV challenge (Kähler et al., 2016). The main parameter governing the behaviour of this method is the time interval (time-segment) considered for the data assimilation. In the present work, the effect of the time-segment length on the spatial resolution is also examined from the analysis of experimental data obtained with large-scale PIV measurements in the wake of a circular cylinder at $Re_D = 27,000$.

6.2. WORKING PRINCIPLE OF TSA

The working principle of VIC-TSA is based upon two concepts:

1. Increasing the amount of data used for CGR, by including measured velocity data over a finite time interval (particles tracks).

2. Seeking for a flow solution that satisfies the vorticity transport equation over a finite time interval

The first concept is elaborated in the subsection below. The second one is the subject of Section 6.3.

6.2.1. EFFECTIVE INTER-PARTICLE DISTANCE FOR MULTI-FRAME DATA

Particle tracers immersed in the fluid flow are assumed to be homogeneously distributed in space. Their concentration C is defined as the number of particles present in a unit volume. The concentration of particle tracers directly determines the length-scales of the flow that can be instantaneously resolved.

Consider the flow schematically depicted in Fig.6.1: three tracer particles $[p_1, p_2, p_3]$ travel along their respective trajectories $[\Gamma_1, \Gamma_2, \Gamma_3]$ (solid blue lines). Their position at a given time instant t_0 are indicated by a filled red circle. Provided that the measurement of the particles position is obtained in time-resolved mode (e.g. by means of high-repetition rate PIV), the sampled positions at N_t+1 consecutive times $[t_{-N_t/2}, \ldots, t_{-1}, t_0, t_1, \ldots, t_{N_t/2}]$ separated by the sampling time interval Δt_s are shown by hollow circles. We denote the time-segment length encompassed by the $N_t + 1$ samples as $T = N_t \cdot \Delta t_s$. The array of $N_t + 1$ positions for each particle is denoted as a track $\Im$ (represented by solid black lines in Fig. 6.1-right). Furthermore, let us denote the average distance among neighboring particles by $\overline{r}$ and the minimum distance among neighbouring tracks by $\tilde{r}$. The condition $\tilde{r} \leqslant \overline{r}$ is always satisfied. Moreover, the ratio $\tilde{r}/\overline{r}$ decreases when the track length L (viz time-segment length T) increases.

For the Cartesian Grid Reduction (CGR) of the flow velocity from sparse tracers, the spacing of the Cartesian grid depends fundamentally upon the mutual distance among neighbouring tracer particles, in turn depending upon the seeding concentration. A sec-
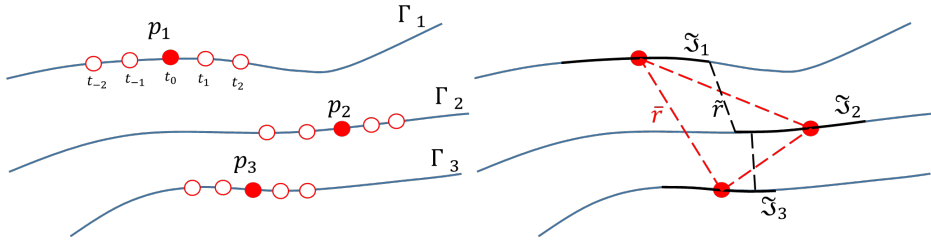
Figure 6.1: Left: schematic of tracer particles sampled five times in their motion along trajectories. Samples at time t_0 are represented by filled red circles. Other samples along the time-segment are marked by hollow circles. Right: particle tracks $\Im$ (solid black lines overlaying the trajectories) and distance between neighbouring particles $\bar{r}$ at time instance t_0 (dashed red) and minimum distance between tracks $\tilde{r}$ (dashed black).

ond parameter is the scheme used to interpolate or reconstruct the velocity field between the scattered data points. As explained in Chapter 2, the VIC + data assimilation method (Schneiders and Scarano, 2016) makes use of the instantaneous velocity and acceleration for the assimilation of the instantaneous volumetric velocity field, to retrieve smaller flow scales than the inter-particle distance. In the above work, the criterion $h = 1/4\bar{r}$ is proposed, where h is the grid spacing. In the present work, the attention focuses on the distance between particle tracers during a finite time interval of length T, that translates into the distance between tracks $\tilde{r}$. The latter depends not only upon the inter-particle distance, but also on the length of the path L traveled during T.

The tracks distance has the following property with time: if a track length is considered such that $L << \tilde{r}$ (defined here as *impulsive regime*), then $\tilde{r} \approx \bar{r}$ and little-to-no improvement can be expected in the CGR process compared with instantaneous reconstruction methods. If $L \approx \tilde{r}$ (*adjacent tracks regime*), then $\tilde{r} < \bar{r}$, and an improvement is expected in terms of spatial resolution that should be proportional to $\tilde{r}/\bar{r}$. It is conjectured here that the equivalent increase in volumetric concentration may scale as $\tilde{r}/\bar{r} > 3$. Finally, any further increase in L beyond $\bar{r}$ (*stringy tracks regime*) is expected to yield diminishing benefits since no substantial decrease of $\tilde{r}$ will occur.

The working hypothesis of the time-segment assimilation stems from the above considerations. The dependency of spatial resolution is shifted from the particles' distance to the tracks' distance. As a consequence, the duration of the assimilated time-segment T becomes the parameter that governs such shift. The three resulting regimes are illustrated in Fig. 6.2.
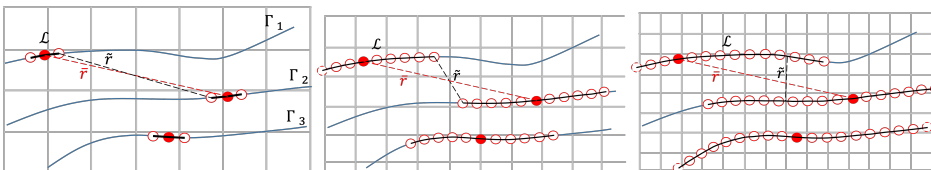
Figure 6.2: Particles and track distance in the impulsive (left), adjacent tracks (middle) and stringy tracks (right) regimes. The time-segment length T and corresponding track length L (solid black) increase from left to right. Grey raster indicative of CGR resolution (based on $1/4\tilde{r}$).

With a short time-segment (for instance given by only three time samples, as in Fig. 6.2-left), the average tracks' distance differs very little from the particles' distance and the spatial resolution of CGR is expected to remain similar to that of methods based on the instantaneous flow properties. On the other side for extremely long tracks as in the stringy tracks regime (Fig. 6.2-right), the distance between neighbouring tracks has already reached the minimum limit of distance between trajectories. The spatial resolution of CGR is expected to approach that obtained with an experiment where the tracers concentration corresponds to particles' distance of $\tilde{r}$. The intermediate condition of adjacent tracks regime is identified as a potential optimum considering the computational efficiency of the VIC calculations, where the track length is increased until most benefits of reducing the tracks distance are included. The criterion for selecting the time-segment length that corresponds to the adjacent tracks regime reads is as follows:

$$\tau^* = \frac{TU}{\overline{r}} \approx 1, \tag{6.1}$$

where U is a reference velocity of the flow, T is the length of the time-segment, and $\overline{r}$ is the average inter-particle distance between the particles in the domain. The following sections aim to prove the stated rationale: the accuracy of the flow reconstruction with TSA depends upon the above introduced regimes.

The above discussion established a criterion for selecting the optimal time-segment length for reducing the effective inter-particle distance $\tilde{r}$. Increasing the time-segment length further does not further reduce $\tilde{r}$, but does require the solution resulting from VIC-TSA to satisfy the flow governing equations over a longer time duration.

Here, the optimum time duration for VIC-TSA is associated with the flow timescales. When taking an integration time similar or larger than the expected flow timescale, the solution is consequently required to behave coherently over this time duration.

6.3. TSA ALGORITHM

The aim of the VIC-TSA technique is to achieve a velocity field at the middle of the time-segment that minimises the difference between the measured particles velocity and the VIC computation along the entire time-segment. The current implementation was introduced by Schneiders and Scarano (2018) and is recalled here for completeness. The input to the algorithm is based on time-resolved 3D tracks data, as issued for instance from tomographic PTV (Novara and Scarano, 2013) or Shake-the-Box analysis (aka Lagrangian particle tracking, Schanz, Gesemann, and Schröder, 2016). The set of particle tracks is referred to as $\Im$ and it entails spatially scattered measurements of particles position $\mathbf{x}_p$ and velocity $\mathbf{V}_p$ sampled N_t times along their trajectories, at regularly spaced time interval Δt_s. Analogous to Schneiders and Scarano (2016) and Saumier, Khouider, and Agueh (2016), the incompressible and inviscid vorticity transport equation is chosen as governing equation for the flow evolution, with appropriate boundary conditions:

$$\begin{cases} \frac{\partial \omega}{\partial t} = (\omega \cdot \nabla) U - (U \cdot \nabla) \omega, \\ \omega(x, t_1) = \omega(x, t_0), x \in \Omega, t \in [t_0, t_1], \end{cases} \tag{6.2}$$

where $\omega = \nabla \times \mathbf{U}$ is the vorticity. The initial vorticity field, $\omega(\mathbf{x}, t_0)$, is numerically integrated in time using a vortex-particle discretization (Vortex-in-Cell, Christiansen, 1973).

Within the vortex-in-cell (VIC) framework, velocity is calculated from vorticity at each integration time instant by solution of a Poisson equation,

$$\nabla^2 \mathbf{U} = -\nabla \times \omega \tag{6.3}$$

In the solution of the above equation, it is assumed that boundary conditions can be selected that make the problem well posed. In case no boundary conditions can be defined *a-priori*, they can be considered as additional unknowns and increase the degrees of freedom in the optimization procedure. The above assumptions have been discussed in Schneiders and Scarano (2016)) and Jeon et al. (2019).

Solving 6.2 and 6.3 for the time-segment T yields the velocity temporal evolution in this measurement time-segment. At every measurement time instant t_n, the computed velocity field $\mathbf{U}_h$ can be evaluated at the instantaneous particle location $\mathbf{x}_p$ to yield the instantaneous disparity $\mathbf{J}_p$ relative to a single particle:

$$J_{p,n} = \mathbf{V}_p(x_p, t_n) - \mathbf{U}_h(x_p, t_n) \tag{6.4}$$

When the operation is performed for the entire particle ensemble and across the time-segment T, one obtains the total disparity:

$$J(T) = \sum_{p,n} \sqrt{J_{p,n}^2} \tag{6.5}$$

that is referred in the remainder as the cost function $\mathbf{J}$, which indicates the quality of the numerical simulation, considering the measurements as a reference. Therefore, $\mathbf{J}$ is at the basis of the optimization algorithm.

In the present work, the boundary conditions are kept fixed, based on an *a-priori* estimation and only the initial vorticity field is taken as degree of freedom. The optimization problem is defined accordingly as $arg[\ min\omega J(\omega(t_0), \mathbf{V}_p)]$.

The sampling frequency adopted in experiments is usually high enough to temporally resolve the relevant timescales of the flow problem. An illustration of the numerical process is given in Fig. 6.3 the process begins by initializing the velocity field at the time t_0. This is achieved by interpolating the tracks data $\mathbf{V}_p$ onto a Cartesian grid, yielding $\mathbf{U}_h$. The vorticity field ω_h is thus estimated by finite-difference at time t_0. The vorticity field along the time-segment is computed using the Vortex-in-Cell framework, similarly to the time super-sampling technique (Schneiders, Dwight, and Scarano, 2014). In Fig. 6.3, the sparse and gridded variables are typed in black and red, respectively.

An iterative problem is built upon these steps to minimize the cost function $\mathbf{J}$ (grey line arrow in Fig. 6.3) by tuning the optimization variable, the gridded vorticity, in every iteration. The problem is solved using the limited-memory Broyden–Fletcher–Goldfarb–Shanno method (L-BFGS, Liu and Nocedal, 1989), an approximation of the BFGS, based on a quasi-Newton method, with a limited amount of memory.

The resulting method remains computationally intensive: VIC-TSA requires approximately 500 and 20 times more CPU time compared to linear interpolation and the VIC + algorithm, respectively. The computational effort increases linearly with the length of the time-segment and with the third power of grid resolution.
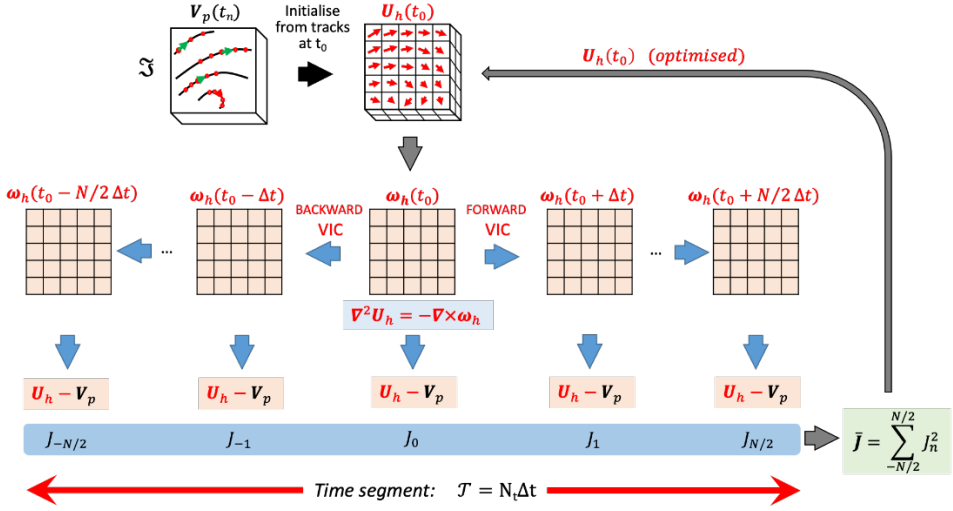
Figure 6.3: Schematic of Time-Segment Assimilation (TSA) reconstruction framework. Velocity and vorticity are initialised (black arrow) from tracks data at the centre of the time-segment (t_0) by interpolating tracks data from the measurements. Time marching by vortex-in-cell (blue arrows) along the chosen time-segment. The cost function J is evaluated from the differences between the computed velocity and the tracks data. The cost function is minimised iteratively (grey line arrow) yielding the optimized velocity field at t_0.

6

6.4. NUMERICAL ASSESSMENT

A synthetic flow field is generated for the numerical assessment of the VIC-TSA technique. The field is described by the steady 3D sine wave lattice shown below,

$$
\begin{cases}
u = A sin\left(\frac{2\pi x}{\lambda}\right) sin\left(\frac{2\pi y}{\lambda}\right) \\
v = A cos\left(\frac{2\pi x}{\lambda}\right) cos\left(\frac{2\pi y}{\lambda}\right) \\
w = A
\end{cases}
\tag{6.6}
$$

where x, y and z are the Cartesian coordinates, A = 2 m/s is the velocity amplitude of the waves along x and y and λ = 0.2 m is their wavelength. The velocity is considered uniform along z.

Sine-based velocity distributions have been extensively used in previous works for steady numerical assessments in 2D (Willert and Gharib, 1991; Scarano and Riethmuller, 2000) and in 3D (4th PIV Challenge, Kähler et al., 2016; Schneiders and Scarano, 2018). The analysis is based on the sinusoid reconstruction, with attention to the modulation of the peak value, as the resolution of the measurement technique deteriorates. The current approach considers a simulated volume of size $0.4 \times 0.4 \times 0.8$ m^3, where randomly distributed particle tracers at a uniform concentration are generated and propagated according to the underlying velocity field. No particle reconstruction errors are simulated. The particle motion is calculated using a fourth-order Runge–Kutta method. The concentration is maintained constant by introducing at the inlet side as many particles as those exiting.

A spatial response analysis is carried out for the mentioned velocity field varying the particles concentration C, and the number of samples N_t composing the assimilated time-segment. The VIC-TSA method is applied with the shortest duration of observation, three snapshots (central scheme in time), a longer segment, $N_t = 11$, and a significantly longer segment, $N_t = 31$. The non-dimensional time length of these segments gives an estimation of the regime of the cases explained in Sect. 6.2. For a time separation between samples $\Delta t_S = 0.001$ s, a convection velocity of the particles A = 2 m/s and an average inter-particle distance $\overline{r} = \sqrt{3/4\pi 1/C} \in (0.03, 0.08)$ m, the non-dimensional time τ^* yields $\tau^* \in (0.05, 0.77), (0.08, 1.22), (0.13, 2.01)$ for $N_t = 3, 11, 31$, respectively. For the current analysis, the grid spacing used for the TSA reconstruction is kept constant for the different cases, h = 0.01 m.

A first qualitative analysis of the spatial response is given in Fig. 6.4, where the u velocity component is displayed. The analysis compares the results when the average inter-particle distance is varied ($\overline{r} = 0.08, 0.05, 0.03$). The upper row illustrates the tracers captured in a slice of the domain of 0.2 m height. The reference velocity field is shown at the right of the figure and it presents the sine waves pattern of Eq. 6.6. A general trend is observed, whereby more peaks are retrieved and with higher values as the assimilation is performed over a longer time. It is remarked here that the technique reconstructs a coherent velocity pattern a low densely seeded flows by using long assimilation times ($\overline{r} = 0.08$ for 31 samples). Such feature is particularly interesting for experiments conducted at low seeding density, as it is the case when helium-filled soap bubbles (HFSB) are used as flow tracers in wind tunnels.

Figure 6.5-left shows the amplitude modulation evaluated with three values of the time-segment duration. The spatial response of a top-hat moving average filter (solid black line) over a cubic element containing 5 tracer particles is also shown for reference. The latter can be representative of the cross-correlation analysis as used in tomographic PIV. The horizontal axis represents the normalized wavenumber r^*, computed as the ratio between the average inter-particle distance and the flow wavelength $r^* = \overline{r}/\lambda$ (lower axis), or between the linear size of the cubic element used as linear filter and the flow wavelength (l^* on the upper axis).

The effect of spatial modulation by decreasing the seeding density is evident for all curves. The most important observation is that the - 3 dB roll-off point (or critical inter-particle distance r_c^*) is progressively delayed when a longer sequence is considered. For a sequence with only three frames, the peak value is halved at $r_c^* = 0.2$. In comparison, for a sequence with 31 frames, one obtains $r_c^* = 0.35$. Such shift corresponds to a fivefold increase of particle concentration.

The present results should, however, be taken with a word of caution, considering that for a steady velocity field, the temporal integration of information yields additional spatial information. Further work should be devoted to defining appropriate analytical test cases that also include the unsteady development of the flow. The experimental section in the present work deals with such unsteady conditions, in absence, however of a reference velocity field as in the present case.

Given the affinity of the TSA-VIC technique with the VIC + method, results from the study of Schneiders, Scarano, and Elsinga (2017) are reported here for comparison. To some surprise, VIC + data feature a flatter behaviour compared to TSA-VIC for sequences
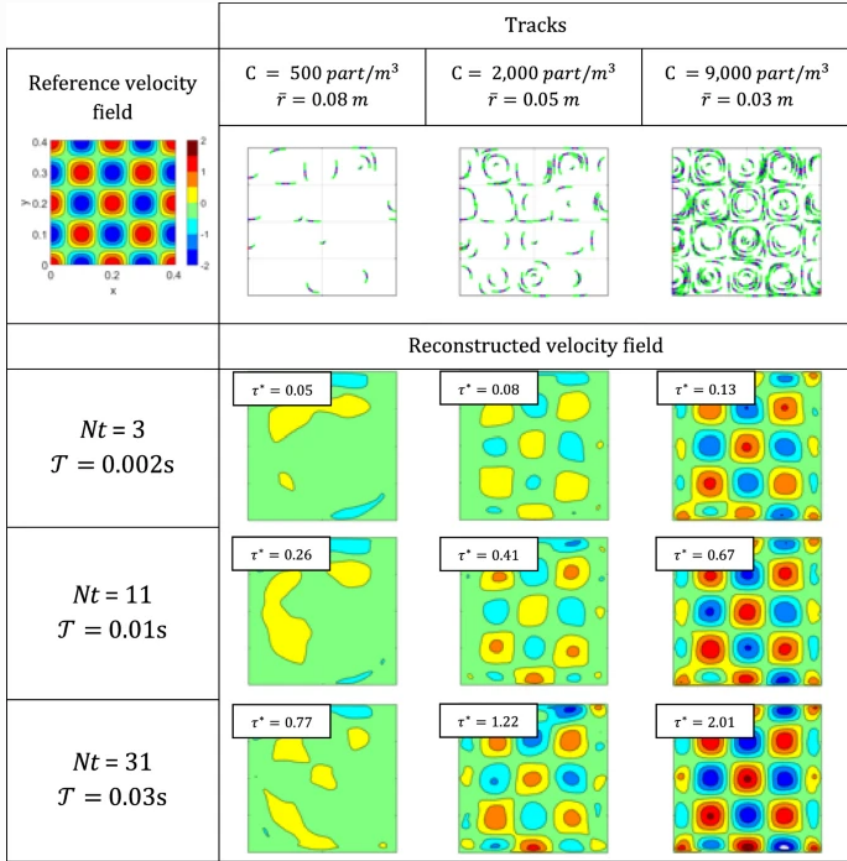
Figure 6.4: Synthetic velocity field (u-component in the top-left corner) and simulated tracks with 3 (magenta), 11 (blue) and 31 (green) exposures (Top row) for increasing value of tracers concentration (left to right). Reconstructed velocity field for time-segment length of 0.002, 0.01 and 0.03 s. The indication of reconstruction regime is given by τ^*.

of 3 to 11 frames. This effect is ascribed to a more accurate optimisation by the use of radial basis functions in the VIC + algorithm. Radial basis functions have not been implemented in the present work for computational affordability and the TSA-VIC algorithm is currently based on the discrete finite-differences method.

The TSA-VIC algorithm requires the numerical evaluation of Eq. 6.2, whereby time marching is required. To this purpose, the effect of the internal time integration on the reconstructed velocity field is evaluated for the chosen values of the time-segment at a seeding particles concentration of C = 3000 particles/m^3 and for a normalized inter-particle distance r^* = 0.2.

Figure 6.5-right shows the amplitude modulation of the reconstructions for the normalized time marching frequency, $d_t^* = \Delta t_{march}/\Delta t_s$. The CFL (Courant–Friedrichs–Lewy) number computed from the reference velocity A = 2 m/s and grid spacing h = 0.01 m is
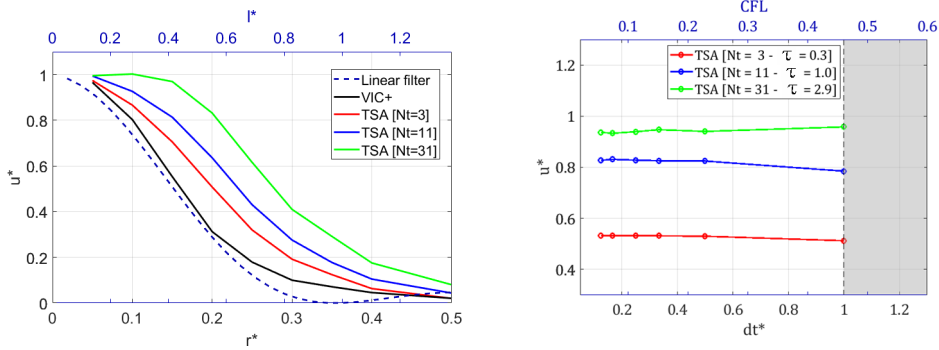
Figure 6.5: Amplitude modulation for the TSA technique (time-segments with 3, 11 and 31 samples). Left: effect of seeding concentration and comparison with linear filter (moving average) and VIC + results from Schneiders, Scarano, and Elsinga (2017). Right: marching time step during the VIC computations.

given as top x-axis (Ferziger, Perić, and Street, 2019). In the inquired range (CFL < 0.5), the result appears to be independent of the choice on the internal time separation.

Finally, the spatial response to the choice of the computational grid is examined. Figure 6.6 compares the results obtained with a fine grid (h = 0.01 m) with those returned using a too coarse grid (h = 0.05 m). The latter results in the amplification of numerical errors, especially when a long-time interval is considered. Such effects can also be observed in Fig. 6.5-left for small values of r^*. The grid spacing considered in Fig. 6.6, however, well beyond the 1/4 criterion suggested in Schneiders and Scarano (2016). Nevertheless, the present result needs to be retained in mind as caveat, when exploring ways to assimilate data with VIC-TSA over a coarse grid.

6
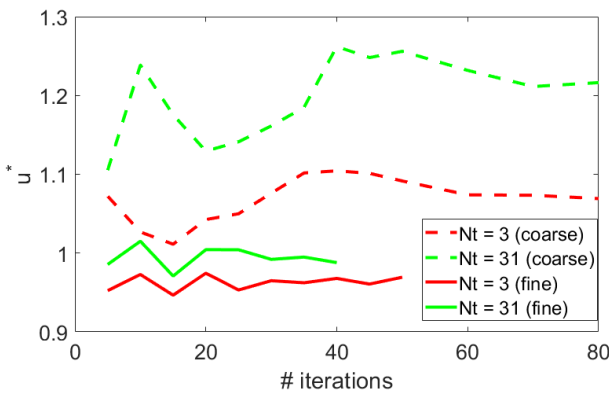
Figure 6.6: Amplitude response convergence history as a function of the reconstruction grid.

6.5. CYLINDER WAKE EXPERIMENT

The experimental case considered for VIC-TSA analysis is the Kármán wake behind a circular cylinder. This easily reproducible experiment is a common benchmark for measurement techniques dealing with unsteady flows. Yet, the large range of length- and timescales, from the Kármán vortices to the shear layer turbulence, poses a challenge to the spatial resolution of field measurement techniques.

6.5.1. EXPERIMENTAL APPARATUS AND PROCEDURES

The experiments are conducted in a large low-speed wind tunnel, the open jet facility (OJF) at the laboratories of the aerospace engineering faculty of TU Delft. The OJF features an exit cross section of 2.85×2.85 m^2. A 2-m-long cylinder diameter D = 10 cm is installed vertically and immersed in the free-stream flow at 4 m/s. The resulting value of the Reynolds number is 27,000. The domain of interest is the near wake of the cylinder. The measurement covers a domain of 5D(X) × 6D(Y) × 3.8D(Z). For the measurements over such an extended region, sub-millimetre helium-filled soap bubbles are used as flow tracers (Scarano et al., 2015). A HFSB seeder hosting 204 generators with cross-sectional area of 0.6×0.9 m^2 is placed in the wind tunnel settling chamber. After the wind tunnel contraction, a seeded stream-tube of approximately 50 cm diameter is produced with particles concentration of about 1 bubble/cm^3. Figure 6.7(top-left) illustrates the HFSB generator used for the experiment.

   Illumination is provided by two LaVision LED-Flashlight 300 (72 elements, white light) directed along the span of the cylinder. The pulsed width is 50 mus (one tenth of the pulse separation time $\Delta t_s = 0.5$ ms, at a repetition rate of 2 kHz). A high-speed tomographic PIV system is employed to record the light scattered by the HFSB tracers with three LaVision HighSpeedStar 6 CMOS cameras (1024 × 1024 px, 5400 frames/s, 12-bit, 20 μm pixel pitch) equipped with Nikon 50 mm focal length objectives, set at numerical aperture $f_\#$ = 22. The cameras subtend a tomographic angle β = 65 degrees. The main components of the PIV system and measurement parameters are summarized in Table 6.1.

Table 6.1: PIV system components and measurement parameters.

Seeding	HFSB, 0.4 mm diameter, neutrally buoyant
Recording devices	3 × HighSpeedStar 6 (1024 × 1024 px, 20vμm pixel size)
Illumination	2 × LED Flashlight 300 (white light, 72 elements)
Imaging	M = 0.05; Resolution: 5 pixels/mm
Measurement domain	0.5(X) × 0.6(Y) × 0.38(Z) m^3
Acquisition rate	f = 2,000 frames/s
Number of samples	N = 3×2,000

   Three sequences of 2000 frames are acquired at a rate of 2 kHz. The particles' motion between subsequent exposures is approximately Δ X = 2 mm in the free stream. Considering a shedding frequency based on a Strouhal number of 0.2, each sequence captures approximately eight shedding cycles. Synchronization of illumination and image recording is performed with a LaVision programmable timing unit (*PTU 10*). Data
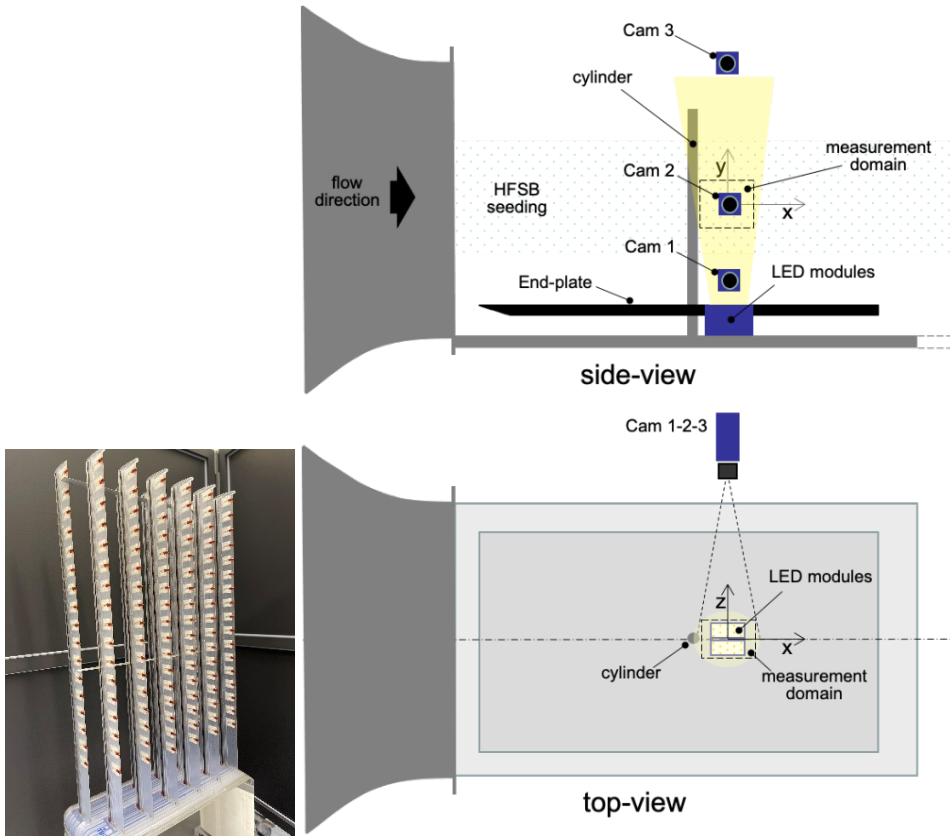
Figure 6.7: (top-left) Illustrates the HFSB generator used for the experiment. HFSB generator (top-left) and schematic views of the experimental set-up in the OJF.

recording, storage, and Shake-the-Box analysis operations are performed with the *DaVis 10* software.

6.5.2. DATA PROCESSING AND TSA ANALYSIS

The images are pre-processed with a time–frequency domain high-pass filter (Sciacchitano and Scarano, 2014) to reduce background illumination. Raw and pre-processed recordings are illustrated in Fig. 6.8. An image-to-object geometrical mapping function is obtained recording the image of a calibration plate with controlled translation across the measurement domain. The residual errors are reduced to below 0.1 pixels using the volume self-calibration algorithm (Wieneke, 2008). Subsequently, an optical transfer function calibration (Schanz et al., 2012) is performed prior to the interrogation of the recordings sequence.

The tracers motion is evaluated with the Shake-the-Box algorithm (Schanz, Gesemann, and Schröder, 2016). Approximately 40,000 tracers are detected in every recording. The use of three cameras and the tracks acceptance criterion yields on average
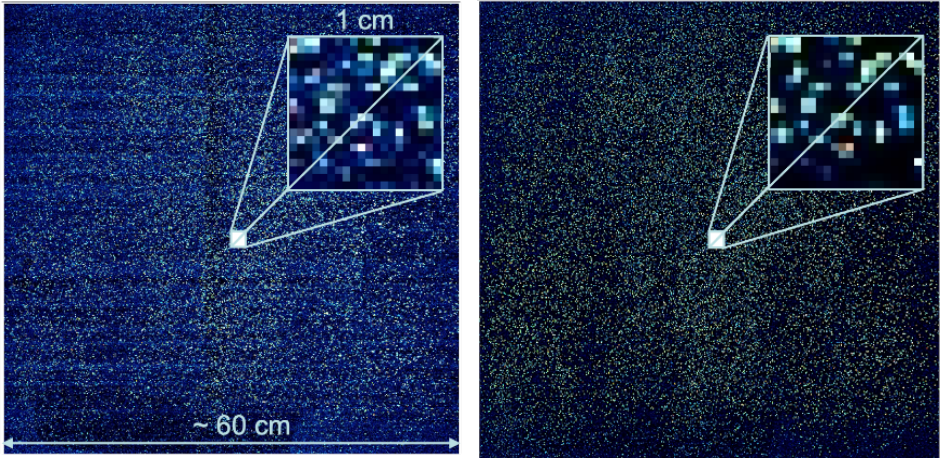
Figure 6.8: Raw (left) and pre-processed (right) particle image recording. The zoomed detail corresponds to a volume of approximately 20 cm^3 (flow direction bottom to top, cylinder at the image bottom edge).

6

12,000 measurements at every time instant. The resulting tracks concentration is C_{tracks} = 0.12/cm^3 and the corresponding average distance among neighboring tracers on the detected tracks is 1.25 cm (discussed as $\bar{r}$ in Sect. 6.2). Table 6.2 summarises the parameters used for the particles motion analysis. An illustration of particle tracks with color-coded instantaneous velocity is given in Fig. 6.9-left. The instantaneous vorticity field reconstructed with VIC# (Jeon et al., 2019) is shown in 6.9-right. Recalling the above discussion, the condition of adjacent tracks (T_{AT}) is therefore attained when the time-segment length for assimilation is T 6 ms (13 exposures). The VIC-TSA analysis is performed in the range T = [1, 2, 4, 7, 11, 17] ms (N_t = 3, 5, 9, 15, 23, 35 exposures).

Table 6.2: Particles motion analysis parameters.

Tracking algorithm	Shake-The-Box
Domain size	0.5(X) × 0.6(Y) × 0.38(Z) m^3
Minimum particle intensity	30 counts
Maximum triangulation error	1 pixel
Minimum track length	4 consecutive frames
Detected particles/frame	40,000
Accepted tracks	12,000
Concentration of tracks	0.12/cm^3
Number of fields	N = 3 × 2000

The internal time marching for the VIC algorithm is chosen as Δt_{march}=0.5 ms, which complies with the CFL conditions (CFL = 0.25) and corresponds to the time separation between recorded samples. The relevant parameter of the VIC-TSA analysis is reported in Table 6.3.
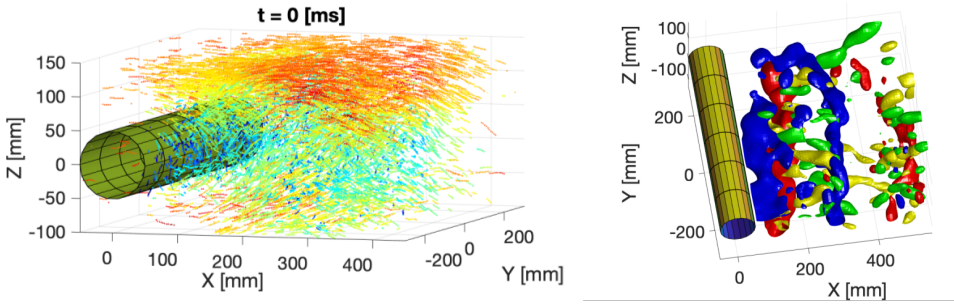
Figure 6.9: Left: visualization of tracks reconstructed with STB in the three-dimensional domain (colour-coded by streamwise velocity component). Only a slab of 100 mm depth is shown for clarity. Right: vortex structure visualization by $\lambda 2$ criterion iso-surfaces (colour-coding by spanwise vorticity). Reconstruction obtained by VIC# and filter length of 2 ms (5 exposures).

Table 6.3: VIC-TSA analysis parameters.

Algorithm	VIC-TSA
Domain size	$0.5(X) \times 0.6(Y) \times 0.38(Z)$ m^3
Grid spacing	8 mm
Time-segment length	1,2,4,7,11,17 ms, 3, 5, 9, 15, 23, 35 frames
Time step for integration	0.5 ms (same as recording time)
Number of iterations	$k = 20$ ($\mathbf{J}_k < 0.1\mathbf{J}_0$)
Output mesh	$63(X) \times 76(Y) \times 42(Z)$ (200, 000 vectors)
Duration of measurement	1 s (8 shedding cycles)

6.5.3. VORTICITY ANALYSIS

The ability to describe the range of flow scales can be examined from the measurement of the instantaneous vorticity distribution. According to the discussion presented in Fig. 6.5-right, the limit condition where spatial scales are resolved is when u^* is just above 0.5. First, a planar visualisation of instantaneous velocity and primary vorticity (along the cylinder axis) illustrates the behaviour of the reconstruction when τ^* varies from the *impulsive* to the *stringy* regime. In Fig. 6.10 (top-left), the time-segment of 1 ms corresponds to $\tau^* = 0.15$ (impulsive regime). This condition approximates that of the velocity-acceleration assimilation method (VIC +, Schneiders and Scarano, 2016). Although the overall oscillatory motion is captured with the distribution of the velocity vectors, the blobs of fluctuating vorticity are comparatively less intense, when compared to the analysis performed with a longer time-segment (e.g. bottom-right corresponds to $\tau^* = 2.8$).

A quantitative analysis of the effect of τ^* on the spatial response of the reconstruction method is presented in Fig. 6.11. The standard deviation of the axial vorticity (ω_y) dominates over the other two components. This is consistent with the alignment of the mean shear with the cylinder axis leading to the formation of spanwise vortices. The values of streamwise vorticity ω_x exceed those of ω_z given the formation of secondary vortices along the streamwise direction (ribs or fingers, Williamson, 1996). The analysis performed with VIC-TSA by varying τ^* indicates that the amplitude of vorticity fluctuations
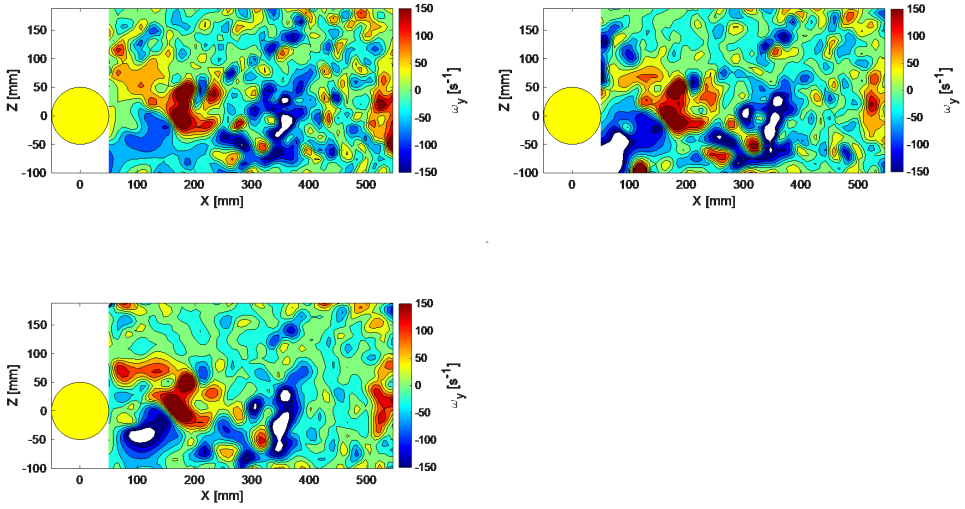
Figure 6.10: Instantaneous vorticity distribution (colour contours). T = 1 ms (top-left), 7 ms (top-right), 19 ms (bottom), ($\tau^* = 0.3, 2, 6$).

6

increases monotonically with the length of the time-segment (Fig. 6.11-left). However, diminishing benefits are found as $\tau^* > 2$. It may be concluded that the condition $\tau^* = 2$ corresponds to a practical optimum (also considering the computational effort required for the VIC time marching and the numerical optimisation process) for the choice of the time-segment in the VIC-TSA technique. Moreover, the comparison between the *impulsive* ($\tau^* < 0.1$) and *stringy* ($\tau^* > 2$) regimes yields an overall increase in approximately 30% for the vorticity fluctuations in the present experiment. Compared to the velocity reconstruction based on linear interpolation (shown in blue in Fig. 6.11), the VIC-TSA reconstructs vorticity from 25 to 50% higher than the linear method. An additional comparison is made with tomographic PIV. In this case, the recordings are reconstructed with the sequential MART method (SMTE, Lynch and Scarano 2015 Lynch and Scarano, 2015) and the cross-correlation analysis is performed with interrogation boxes of 52 × 52 × 52 voxels with 75% overlap, yielding the same grid spacing of 8 mm. The amplitude of the vorticity fluctuations is higher than that obtained with the linear interpolation, which apparently contradicts the analysis of Schneiders and Scarano (2018), where for a given set of particles in 3D space, linear interpolation yields a higher spatial resolution than the cross-correlation analysis. However, in the present case, the linear interpolation is performed using only the velocity vectors of the accepted tracks, whereas the cross-correlation interrogation may also include particles not reconstructed with IPR. Overall, the level of vorticity fluctuations is similar to that of VIC-TSA with very short time-segment.

A question that may arise is whether the increase in vorticity fluctuations amplitude is not to be ascribed to an overall increase in the reconstruction noise by larger values
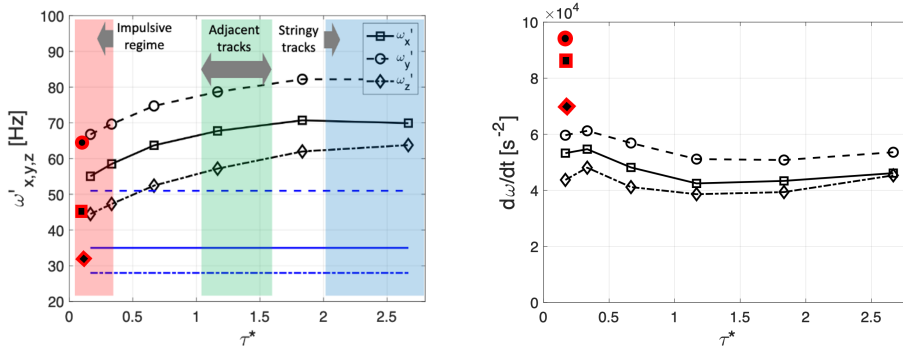
Figure 6.11: Left: standard deviation of vorticity fluctuations. Black lines and symbols pertain to VIC-TSA. Blue lines (with same line coding) correspond to values obtained with linear interpolation on the same data mesh. Red–black labels correspond to results obtained with tomographic PIV. Impulsive, adjacent and stringy regimes indicated by red, green and blue areas, respectively. Right: temporal derivative of vorticity from VIC-TSA and by tomographic PIV (red–black labels).

of τ^*. An indication can be found in figure 6.11-right, where the time derivative of the vorticity is shown. Here, the time derivative of vorticity appears little affected by the variation in τ^*, indicating that the increase in vorticity fluctuations amplitude with the longer time-segment shall not be ascribed to noise. Results from tomographic PIV exhibit comparatively larger values. The measurement noise associated with two-pulse systems can be lowered with multi-frame methods as discussed in Raffel et al. (2018).

The three-dimensional instantaneous flow organization is presented by iso-surfaces of the vorticity components in Fig. 6.12. The illustration shows the unsteady flow organisation dominated by spanwise rollers forming the Kármán street, producing vorticity fluctuations of highest amplitude. These vortices are approximately aligned with the cylinder axis and are shed with alternating sign of vorticity (red for counterclockwise and blue for clockwise). Additional to the Kármán vortices, secondary elongated structures are formed that interconnect the primary rollers from the outer side of the wake where low-speed fluid is ejected under the effect induced by the primary vortices. These structures develop along the streamwise (X) and the vertical (Z) direction and are produced in the region of flow subject to positive strain between two Kármán rollers. Such organisation is most often observed at flow regimes with lower Reynolds number ($Re_D < 1000$, Prasad and Williamson, 1997; Kanaris, Grigoriadis, and Kassinos, 2011, among others) where these structures are reported as fingers or ribs. They become less coherent in the high-Reynolds regimes, yet the mechanism of ribs interconnecting the Kármán rollers is reported in works conducted at $Re_D = 3900$ (Parnaudeau et al., 2008). In figure 6.12, these structures are identified by considering the vorticity components along X and Z and they are colour-coded using the sign of ω_x (yellow for counterclockwise and green for clockwise). In the present context, Fig. 6.12 is used to elucidate the overall effect of the time-segment length used for the VIC-TSA data reduction. The first column shows the reconstruction obtained with $T = 1$ ms ($\tau^* = 0.3$), where the main rollers are identified along with the secondary structures. The overall vorticity distribution is visibly scattered

and the secondary structures do appear, but mostly interrupted. When entering the adjacent tracks regime ($\tau^* = 2$) in the middle column of Fig. 6.12, the vorticity distribution appears more coherent with a clear distinction between the primary rollers and the ribs. Moving further to $T = 19$ ms ($\tau^* = 6$), one can observe an overall increase in vorticity coherence. Although, the analysis shown in Fig. 6.11 does not yield an important increase in vorticity fluctuations beyond $\tau^* = 2$, the flow reconstruction shows well-connected ribs and vorticity with peak fluctuations at a scale of 1–2 cm.
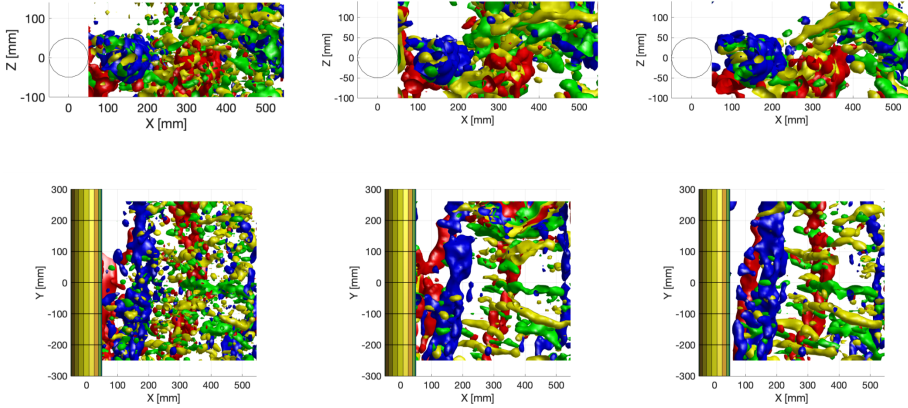
Figure 6.12: Instantaneous vorticity estimation for T = 1 (left), T = 7 (middle) and T = 19 ms (right). Correspondingly $\tau^* = 0.3, 2, 6$. Upper row is axial view (X–Z plane) and lower row is normal view (X–Y plane). Red and blue iso-surfaces for y-vorticity ($\omega_y = \pm 150 \ s^{-1}$). Yellow and green iso-surfaces for x and z vorticity, respectively (colour-coded by x-vorticity).

6.6. CONCLUSIONS

A data assimilation technique has been introduced that considers data distributed over a finite time-segment to reconstruct the optimal 3D vorticity and velocity fields described within such segment. The technique is coupled to the Vortex-in-Cell paradigm to produce a dense reconstruction of the velocity field based on spatially sparse measurements of tracers' trajectories. A first-principle analysis indicates the potential of VIC-TSA in terms of spatial resolution, by identifying three main data reduction regimes, namely impulsive, adjacent tracks and stringy.

A numerical analysis that follows the approach presented in the literature is carried in a 3D lattice of sinusoids, where the velocity amplitude modulation is inspected for varying conditions of tracers concentration, sinusoids wavelength and, most importantly, time-segment length. The cut-off of amplitude reconstruction is delayed when the time-segment increases, consistently with the hypotheses formulated in the first-principle analysis.

Experiments are conducted with large-scale PIV, where the wake of a circular cylinder at $Re_D = 27{,}000$ is measured using helium-filled soap bubbles and a tomographic

imaging system comprising three high-speed cameras. The tracers motion analysis is delivered using the Shake-the-Box algorithm, and the database of particle trajectories is examined using VIC-TSA. The statistical analysis of vorticity fluctuations reveals that the modulation of vortex structures reconstructed by VIC-TSA decreases as the time-segment is made longer. An optimum trade-off between spatial resolution and computational burden is identified with the criterion $\tau^* = 2$, i.e. twice the value of adjacent tracks regime. The topology analysis of the vortex structure confirms the salient features of the Kármán wake with sub-structures being resolved at a scale comparable to the average inter-particle distance.

6

7

VIC+ APPROACHES FOR SOLID BOUNDARIES

Real men don't dance to other people's tune,
instead, they play for others to dance.

Michael Bassey Johnson

Chapter 6 dealt how to include temporal information when reconstructing velocity fields. Other challenge for FSI experiments, as introduced in Chapter 1, is the fluid-solid inter-phase, where information is difficult to measure yet critical for accurately characterizing the interaction. Two different approaches based on the computational fluid-structure interaction frameworks are proposed in this chapter, to handle generic solid body intrusions within the densely interpolated LPT data. The introduced variants of the state of the art physics-driven data assimilation methods are assessed with a high fidelity numerical test case of flow over periodic hills. The proposed approaches show superior accuracy to the traditional VIC+ method especially in close proximity of the solid surface. An experimental application of the introduced methods is demonstrated to compute the pressure distribution over an unsteadily moving elastic membrane surface, revealing the time-resolved interaction between the flow structures and the membrane deformations.

7.1. INTRODUCTION

Although VIC+ and its variants are proven to successfully increase the spatial resolution of LPT data on uniformly structured computational grids, their applicability is restricted to purely fluidic domains. However, most practical engineering applications involve dynamic fluid-structure interactions which contain non-uniform solid boundaries that might deform unsteadily. Thus, computation of fluid information in presence of curved walls or solid objects (stationary or moving) introduces significant drawbacks in terms of numerical accuracy and appropriate surface definition for implementation of adequate boundary conditions. Without proper definition of solid boundaries, accurate determination of fluid properties along the structural surfaces becomes significantly problematic as boundary conditions and the information transfer between fluid and solid domains are strongly dependent on the interface description (Dowell, 2014). More recently proposed methods for managing non-uniform solid intrusions, separate the computational domain in to multiple regions. In these approaches, the incapacity of available data assimilation algorithms to capture near surface information yields loss of valuable information (Saiz, Sciacchitano, and Scarano, 2022). Although these methods provide accurate results in comparison with the extrapolation techniques, the improvements are associated with increased levels of complexity and computational cost. Therefore the current study introduces two approaches for providing VIC+ algorithm with the capability of performing data assimilation in presence of solid boundaries by implementing the well known computational fluid-structure interaction (FSI) frameworks of Arbitrary Lagrangian–Eulerian (Noh, 1963) and immersed boundary treatment methods (Peskin, 1982).

Two main approaches, named ALE-VIC+ and ImVIC+, are proposed to handle the solid boundary effects for VIC+ applications. Accordingly, section 7.2.1 gives brief background information on the boundary treatment approaches utilized in computational fluid dynamics simulations (CFD) which form the basis for the proposed methods. Then, sections 7.2.2 and 7.2.3 discuss the numerical implementation those approaches within the frameworks of ALE-VIC+ and ImVIC+ respectively.

7.2. NON-UNIFORM BOUNDARY TREATMENTS FOR VIC+

7.2.1. TREATMENT OF NON-UNIFORM BOUNDARY DEFORMATIONS IN CFD

The ALE-VIC+ approach utilizes the Arbitrary Lagrangian–Eulerian developed for computational FSI simulations, accompanied with boundary fitted coordinate systems and mesh adaption procedures (figure 7.1, bottom-left). In ImVIC+ method, instead, the immersed boundary treatment is utilized to satisfy the appropriate boundary conditions while preserving uniform mesh formations (figure 7.1, bottom-right).

ARBITRARY LAGRANGIAN–EULERIAN METHOD

In order to avoid the individual shortcomings of Eulerian and Lagrangian perspectives while leveraging from their respective advantages, a technique referred as the Arbitrary Lagrangian–Eulerian (ALE) method was introduced by Noh (1963), where both approaches are utilized in a coupled manner to handle appropriate fluidic and structural domains simultaneously. As the necessity of a coupled method emerges from the motion of bound-
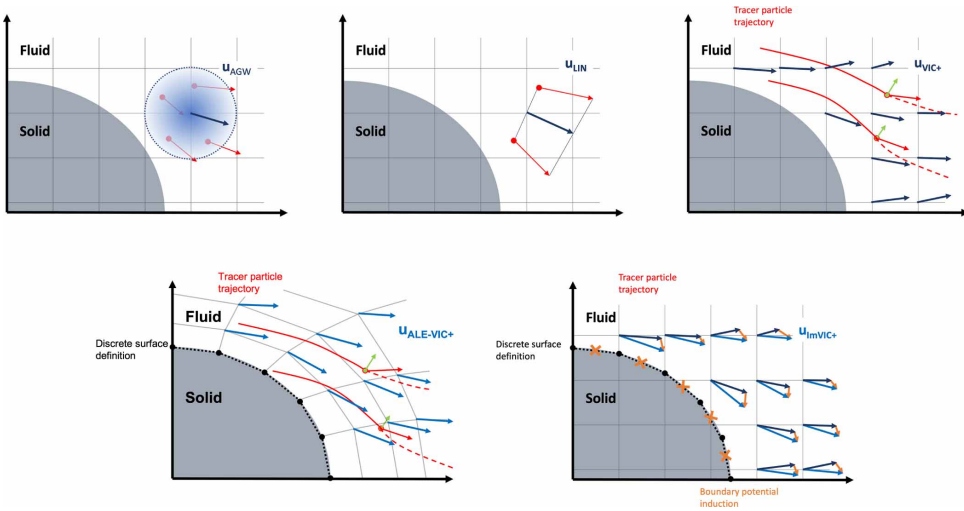
Figure 7.1: Velocity reconstruction from LPT measurements of velocity (red vectors) and acceleration (green vectors) with AGW (dark blue vectors, top-left), linear interpolation (dark blue vectors, top-middle), VIC+ (dark blue vectors, top-right), ALE-VIC+ (light blue vectors, bottom-left) and ImVIC+ (light blue vectors, bottom-right).

aries enclosing the fluidic domain, the corresponding mesh formations are required to be modified accordingly. Hence, a natural approach can be considered as completely regenerating the grid structure at each time step. However, this process generally requires considerable user interaction and immense computational resources (Luke, Collins, and Blades, 2012). Instead, grid deformation algorithms provide a valuable solution categorized under two main groups of physical analogy (Löhner and Yang, 1996; Farhat, Lesoinne, and Le Tallec, 1998; Helenbrook, 2003) and interpolation based schemes (Liu et al., 2006; Jones and Samareh-Abolhassani, 1995, Wang and Przekwas, 1994). Utilizing these various methodologies, there exists multiple applications of the ALE method for vortex simulations based on the VIC model, for cost-effective high-fidelity numerical simulations of FSI problems. In this regard, Cottet and Poncet (2004) performed conformal mapping of the fluidic domain for three dimensional direct numerical simulations of wall bounded flows where the grid structure in close proximity of a sphere was fitted to the surface of the solid object for application of a hybrid particle-mesh vortex method. Furthermore, Kudela and Kozłowski (2009) employed a boundary fitted coordinate system for flow simulations around arbitrary shaped objects using the VIC framework during which fourth order interpolation kernels used by Cottet, Koumoutsakos, et al. (2000) are modified for particle-mesh switching of vorticity distributions in the near wall regions.

IMMERSED BOUNDARY TREATMENT IN CFD

The VIC framework introduced by Christiansen (1973) allows the fast Fourier transform (FFT) based Poisson solvers to be employed over a predefined computational grid (Wu, JaJa, and Balaras, 2013) allowing higher fidelity and resolution capabilities, while pre-

serving the computational efficiency. As the fast Poisson solvers are utilized to characterize the rotational component of velocity vectors, physical intrusions within the flow field are required to be handled employing additional velocity or forcing terms. Therefore, the need for boundary fitted coordinate systems and introducing transformation operations between computational and physical coordinate systems is obliterated. Accordingly, Walther and Morgenthal (2002) and Cottet and Poncet (2004) implemented integral boundary equations on the VIC method in order to impose no-through and no-slip boundary conditions by means of surface singularities. However, defining no-through boundary condition over the penetrating velocity components results in an integral boundary equation which corresponds to an ill-posed Fredholm integral equation of first kind. Instead, the vortex sheet strengths are determined via the tangential velocity components yielding a Fredholm integral equation of second kind (Beale and Greengard, 1994). Furthermore, in order to obtain a unique solution for multiply connected regions, Kelvins theorem of circulation conservation or Kutta condition is introduced as an additional constraint (Morgenthal and Walther, 2007).

7.2.2. ARBITRARY EULERIAN–LAGRANGIAN APPROACH FOR VIC+

The ALE-VIC+ (figure 7.2, black) comprises of two main steps in which a computational grid is generated according to the surface information and the flow governing equations within the VIC framework are solved over the generated boundary fitted coordinates. Then the problem closure is described by the definition of a cost-function for the optimization procedure.
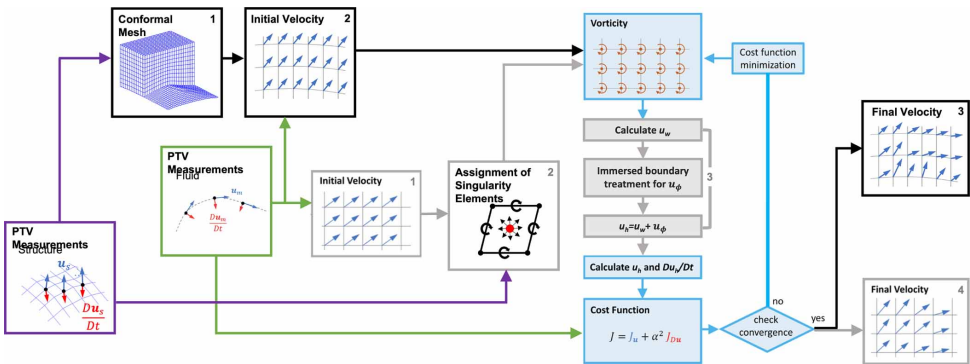
Figure 7.2: Dense flow field interpolation (VIC+) with generic solid boundary treatments; ALE-VIC+ implementation (black boxes) & ImVIC+ implementation (grey boxes). The LPT measurements for the flow is provided (green box) and an initial velocity estimate made (black-2 & grey-1) to be introduced into VIC+ iterative procedure (blue boxes). In case of ImVIC+, the velocity fields are corrected with immersed boundary treatment (grey-3).

BOUNDARY FITTED COORDINATE SYSTEM ADAPTATION

Depending on the availability of the surface information, two different approaches can be followed to reconstruct the corresponding boundary shapes. If the immersed boundary shape is known a priori, it is directly provided as an input to the grid generation

schemes along with the appropriate volume dimensions for the boundary fitted coordinate system to be created. In case where the unsteady motion of the solid boundary is captured by means of optical measurement methods, the captured structural motion is instantaneously provided to the grid generation algorithms. After an initial boundary fitted grid structure is generated, the mesh is deformed according to the boundary motion so that the exact interaction between the fluidic and solid domains can be expressed in a time-resolved manner. In order to achieve a continuous boundary conformation, the choice of deformation scheme is determined as RBF based mesh deformations (De Boer, Schoot, and Bijl, 2007) due to their proven mesh deformation accuracy and cost-efficiency (Smith, Cesnik, and Hodges, 2000; Beckert and Wendland, 2001).

The formulations employed for RBF based mesh deformation method utilized are described by De Boer, Schoot, and Bijl (2007) where a comparative study over many variants of RBFs was conducted using two different mesh quality metrics based on mesh size preservation and mesh skewness. Among 14 different RBFs with compact and global supports, thin plate spline and CP C2 RBFs stood out by keeping the size alterations and skewness to a minimum whilst not compromising mesh adaptation efficiency. According to the presented results, CP C2 RBF is utilized to update the computational grid due to a superior performance of mesh deformations especially in close proximity of the immersed boundary surface.

VIC+ ON BOUNDARY FITTED COORDINATES

The flow governing equations on the updated conformal grid are solved, by performing a one-to-one mapping between the physical and a computational coordinate systems. The mapping relates to the transformation variables necessary for accurate description of mathematical operators constructing the link between the two grids. The physical coordinate system is selected as the Cartesian one since the flow field properties are obtained from the PTV/LPT measurements are already defined on a Cartesian coordinate system. Hence, the computational grid locations in any mesh form can be expressed as functions of the physical coordinates,

$$x_C = x_C(x_P, y_P, z_P) \, y_C = y_C(x_P, y_P, z_P) \, z_C = z_C(x_P, y_P, z_P) \tag{7.1}$$

where subscripts P and C, refer to the physical and computational coordinates respectively. Therefore, the flow governing equations within the VIC+ method are described on the computational coordinates by transforming the vector variables utilizing the chain rule and a transformation matrix that defines the link between the two coordinate systems.

$$\mathbf{T} = \frac{\partial(x_C, y_C, z_C)}{\partial(x_P, y_P, z_P)} = \begin{bmatrix} \frac{\partial x_C}{\partial x_P} & \frac{\partial x_C}{\partial y_P} & \frac{\partial x_C}{\partial z_P} \\ \frac{\partial y_C}{\partial x_P} & \frac{\partial y_C}{\partial y_P} & \frac{\partial y_C}{\partial z_P} \\ \frac{\partial z_C}{\partial x_P} & \frac{\partial z_C}{\partial y_P} & \frac{\partial z_C}{\partial z_P} \end{bmatrix} \tag{7.2}$$

The two governing equations of the VIC framework described as the velocity(u)-vorticity(ω) formulation in equation 7.3 and the vorticity transport equation in equation 7.4,

$$\nabla_P^2 \mathbf{u} = -\nabla_P \times \omega \tag{7.3}$$

$$\frac{\partial \boldsymbol{\omega}}{\partial t} = (\boldsymbol{\omega} \cdot \nabla_P)\,\mathbf{u} - (\mathbf{u} \cdot \nabla_P)\,\boldsymbol{\omega} \tag{7.4}$$

The viscous terms are neglected in equation 7.4. As the inviscid Navier–Stokes equations are considered to be valid due to fact that on large scale applications with HFSB tracers, particle concentrations near the walls are significantly reduced and the tracers are observed to be too large for entering the viscous sublayers (Faleiros et al., 2018). Vector operators (∇_P, $\nabla_P \times$ and ∇_P^2 referring to the gradient, curl and Laplacian respectively) can be expressed on the computational coordinates through equations 7.5–7.7,

$$\nabla_P = \left[\frac{\partial}{\partial x_P}\,\frac{\partial}{\partial y_P}\,\frac{\partial}{\partial z_P}\right]^T = \nabla_C^T \times \mathbf{T} \tag{7.5}$$

$$\nabla_P \times = \begin{bmatrix} 0 & -\frac{\partial}{\partial z_p} & \frac{\partial}{\partial y_p} \\ \frac{\partial}{\partial z_p} & 0 & -\frac{\partial}{\partial x_p} \\ -\frac{\partial}{\partial y_p} & \frac{\partial}{\partial x_p} & 0 \end{bmatrix} = \left(\nabla_C^T \times \mathbf{T}\right) \times \tag{7.6}$$

$$\nabla_P^2 = \nabla_P^T \mathbf{I} \nabla = \frac{1}{\mathbf{J}_T}\nabla_C^T \mathbf{I} \nabla_C \tag{7.7}$$

in which $\mathbf{J}_T$ is the Jacobian of the transformation matrix and I is the identity matrix. Hence the velocity-vorticity relation in equation 7.3 with $\mathbf{u} = [u_{x_P} u_{y_P} u_{z_P}]$ and $\boldsymbol{\omega} = [\omega_{x_P} \omega_{y_P} \omega_{z_P}]$ reads,

$$\nabla_P^T \mathbf{I} \nabla \mathbf{u} = \frac{1}{\mathbf{J}_T}\nabla_C^T \left(\frac{1}{\mathbf{J}_T}\mathbf{C}^T \mathbf{I} \mathbf{C}\right)\nabla_C \mathbf{u} = \left(\nabla_C^T \times \mathbf{T}\right) \times \boldsymbol{\omega} \tag{7.8}$$

where C is the cofactor of the transformation matrix. Thus, the corresponding vorticity transport equation described by equation 7.4 is derived as follows.

$$\frac{\partial \boldsymbol{\omega}}{\partial t} = \left(\boldsymbol{\omega} \times \left(\nabla_C^T \times \mathbf{T}\right)\right)\mathbf{u} + \left(\boldsymbol{\omega} \times \left(\nabla_C^T \times \mathbf{T}\right)\right)\mathbf{u} \tag{7.9}$$

COST-FUNCTION COMPUTATION AND ADJOINT GRADIENT OPTIMIZATION

As the orientation of velocity and acceleration vectors are preserved on the Cartesian descriptions, the resultant flow properties of velocity and material acceleration values at the original particle locations are used for calculating the error between the dense flow field interpolation and the measurement data. Following the exact procedure of adjoint gradient computation introduced for VIC+ with, additional modifications are implemented to take into account the link between the physical and computational grid structures. Hence, the adjoint gradient for the proceeding steps of the optimization procedure is computed and the optimization procedure is performed until a specified convergence criteria of $J_F/J_I = 10^{-3}$ of the initial value of the cost function is achieved.

7.2.3. IMMERSED BOUNDARY TREATMENT FOR VIC+

Implementation of the immersed boundary treatment for VIC+ method is based on the theory of vector decomposition provided via the Helmholtz theorem (Fig. 7.2, gray). First, surface singularity elements are distributed over the solid boundary surface to satisfy the appropriate boundary conditions throughout the data assimilation procedure. The VIC method allows rotational component of the flow behavior to be characterized by means of distributed vortices and their respective velocity induction over a prescribed domain. Hence, the potential flow component of the velocity field due to the presence of a non-uniform surface intrusion is discretized by superimposing an additional velocity field due to the introduced surface singularity distribution. Then the problem closure is provided by the definition of a cost-function for the optimization procedure.

SOLID BOUNDARY CHARACTERIZATION AND SINGULARITY ATTACHMENT

The numerical implementation of boundary integral equations for adequate description of boundary conditions over the interface surfaces is performed using the panel method introduced by Hess and Smith (1967). Considering that the structural information is obtained by means of either one of the aforementioned approaches described for ALE-VIC+, the solid boundary surface is characterized by means of quadrilateral panels each equipped with singularity elements of sources and doublets to introduce a scalar potential influence of the physical intrusion (Fig. 7.3). With singularity elements attached, the potential inductions of the quadrilateral panels are computed over the complete computational domain employing the formulations provided by Katz and Plotkin (2001).
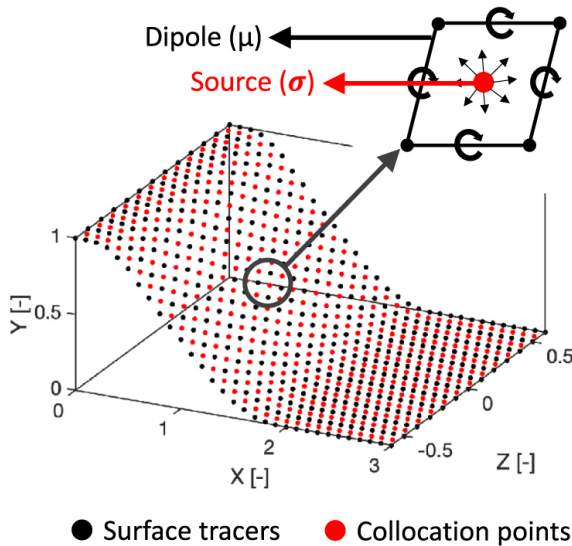
Figure 7.3: Surface description for the periodic hill structure with surface tracers (black dots) and collocation points (red dots) for the corresponding quadrilateral panels.

VIC APPLICATION FOR ROTATIONAL COMPONENT CALCULATION

The initial estimation for the velocity field information is provided in terms of a freestream velocity value. Hence, the computational grid locations are equipped with pointwise vortices and the vorticity distribution over computational domain is utilized to compute the velocity distribution using the velocity-vorticity relation for the rotational velocity vector component in equation 7.10.

$$\nabla^2 \mathbf{u}_\omega = -\nabla \times \boldsymbol{\omega} \tag{7.10}$$

DETERMINATION OF POTENTIAL FLOW COMPONENT

The calculated velocity field penetrates the physical boundaries. Thus, to satisfy the no-through boundary condition over the solid boundaries, the normal velocity components to each panel are equated to the relative source strengths (σ_i) of the corresponding panels. Hence, the strengths of the dipoles (μ_i) are reduced for ensuring numerical uniqueness (Tarafder, Saha, and Mehedi, 2010).

$$\sigma_i = \mathbf{n}_i \cdot \mathbf{V}_i \tag{7.11}$$

Furthermore, since the self induced scalar potential should vanish at collocation points over a surface of singularities (Lewis, 1991), the dipole strengths are calculated by constructing a linear system of equations imposing that total sum of potential induction at the central locations of the quadrilateral panels equals to zero.

$$\sum_{i=1}^{N} a_i \mu_i + \sum_{i=1}^{N} b_i \sigma_i = 0 \tag{7.12}$$

In order to establish a unique solution, the corresponding vortex rings (dipoles) are imposed to comply with the conversation of circulation while their strengths are being determined. The resultant overdetermined linear system is solved employing a least squares method (Soifer, 2012).

$$\mathbf{u}_\phi = (u_\phi, v_\phi, w_\phi) = \left(\frac{\partial \phi}{\partial x}, \frac{\partial \phi}{\partial y}, \frac{\partial \phi}{\partial z} \right) \tag{7.13}$$

Moreover, the scalar potential field induced by the surface singularities is differentiated in three dimensions to obtain the velocity vector components, which are then superimposed to calculate the resultant velocity field distributions.

$$\mathbf{u} = \mathbf{u}_\omega + \mathbf{u}_\phi \tag{7.14}$$

Then, the corresponding velocity and vorticity fields are utilized to calculate the material derivative distributions over the computational domain in accordance to the inviscid Navier–Stokes formulation.

The cost function for the optimization procedure is evaluated based on the errors of velocity and material acceleration values at the original particle track locations in comparison to the measured data. For the optimization procedure, it is assumed, due to the dependence of the potential flow component to the rotational elements, that the errors directly relate to the vortex-in-cell base which is dictated by the vorticity distributions. Hence, for each step of the optimization procedure, the gradient is calculated in terms of the vorticity strengths and the corresponding potential flow component is calculated to correct the velocity field distributions in order to satisfy the physical boundary condition of no penetration through the solid surfaces.

7.3. NUMERICAL ASSESSMENT

7.3.1. TEST CASE AND DATA PROCESSING

Validation studies of the proposed ALE-VIC+ method are performed with a direct numerical simulation (DNS) of flow over periodic hills. The simulations are conducted with a computational domain composed of two consecutive hill forms connected over a region of $144\ h^3$, where h represents the non-dimensional heights of the hills. Hence, the length dimensions of the domain in Cartesian coordinates are provided over normalized values with h. The numerical simulations are performed with periodic boundary conditions for inflow and outflow boundaries while the non-uniform surface contours of the hills are treated by means of an immersed boundary method to account for their influence over the fluidic domain imposing the no-slip boundary condition over the intruding hill surface (Chen et al., 2014). The inflow conditions are initialized with a non-dimensional velocity distribution of u = 1 which corresponds to a hill height based Reynolds number of Re_h = 10,595 as the non-dimensional kinematic viscosity is prescribed to be $v = 9.45 \times 10^{-5}$.

In order to provide an accurate representation of scattered particle track information, the DNS results are randomly downsampled with particle concentrations of C = 25 par/h^3, C = 125 par/h^3 and C = 250 par/h^3. The corresponding particle image densities over the projected volumes obtained as N_P = 0.01 ppp, N_P = 0.05 ppp and N_P = 0.1 ppp allowing a sensitivity investigation of the proposed data assimilation approaches to available particle concentrations. Simulation of LPT data structure is achieved via a pseudo-particle tracking approach applied over the instantaneously extracted flow field data. The procedure is initiated with random downsampling of high density flow information of the DNS data field in accordance to the prescribed particle concentrations for a selected time instant. Then a Runge–Kutta 4 time integration procedure is used to compute the particle propagation in time (Zheng and Zhang, 2017). In order to minimize the truncation error propagation due to the numerical approximations, the integration procedure is applied in both forward and backward directions in time. For accurate extraction of velocity and acceleration values, the tracks are selected to be composed of seven time-steps. Then a Gaussian noise of 0.2 voxels in all three dimensions is artificially introduced to particle locations along the tracks to account for measurement and reconstruction errors (Sciacchitano, Leclaire, and Schröder, 2022). Finally, the corresponding particle tracks are regularized with polynomials of order 2 to compute the velocity and

material acceleration.
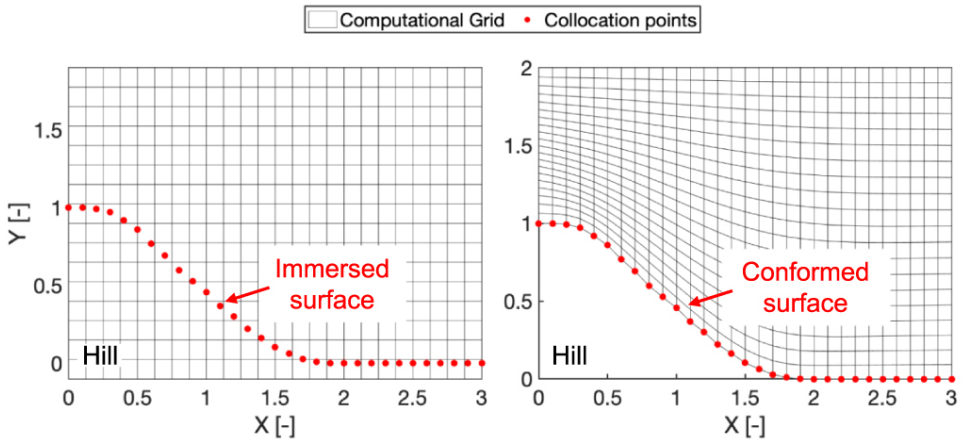
Figure 7.4: Computational grids for the dense interpolation approaches. Uniform structured mesh with the immersed boundary surface for VIC+ & ImVIC+ (left) and the curvilinear boundary fitted mesh on the hill surface for ALE-VIC+ (right).

7.3.2. RESULTS

To be able to demonstrate the improvements obtained with the proposed approaches over the state of the art of data assimilation, the standard VIC+ method is also employed to perform the dense interpolation of the velocity and material accelerations. However, since the base algorithm of VIC+ is not capable of handling the non-uniform boundary, the grid locations corresponding to the solid domain are artificially modified to have zero velocity and material acceleration values to prevent numerical divergence of the optimization procedure. Moreover, the spatial resolutions for the dense flow field reconstruction procedures are selected to have comparable grid spacing with the DNS simulations ($\Delta h = 2 \times 10^{-3}$ h), to achieve better comparison of the reconstructed flow properties with the reference flow field. The corresponding computational grids for VIC+ and ImVIC+ (uniform structured grid with the immersed boundary surface) and for ALE-VIC+ (curvilinear grid boundary-fitted on the hill surface) are illustrated in figure 7.4-left and figure 7.4-right respectively.

To start with the standard LPT approach where the AGW is used to capture flow properties in close surroundings of each grid locations, the results failed to provide almost any relevant fluidic information due to the lack of particles. Hence, the corresponding need for an interpolation approach to reconstruct a coherent flow field description is addressed by linear interpolation, VIC+, ALE-VIC+ and ImVIC+ approaches. The initial comparisons performed qualitatively over the streamwise velocity magnitude distributions reveal similar results in terms of the overall coherence characteristics for both linear interpolation and VIC+ based approaches. Both methods identify the major flow structures of high and low velocity regions in relation to the reference simulations (figure 7.5).
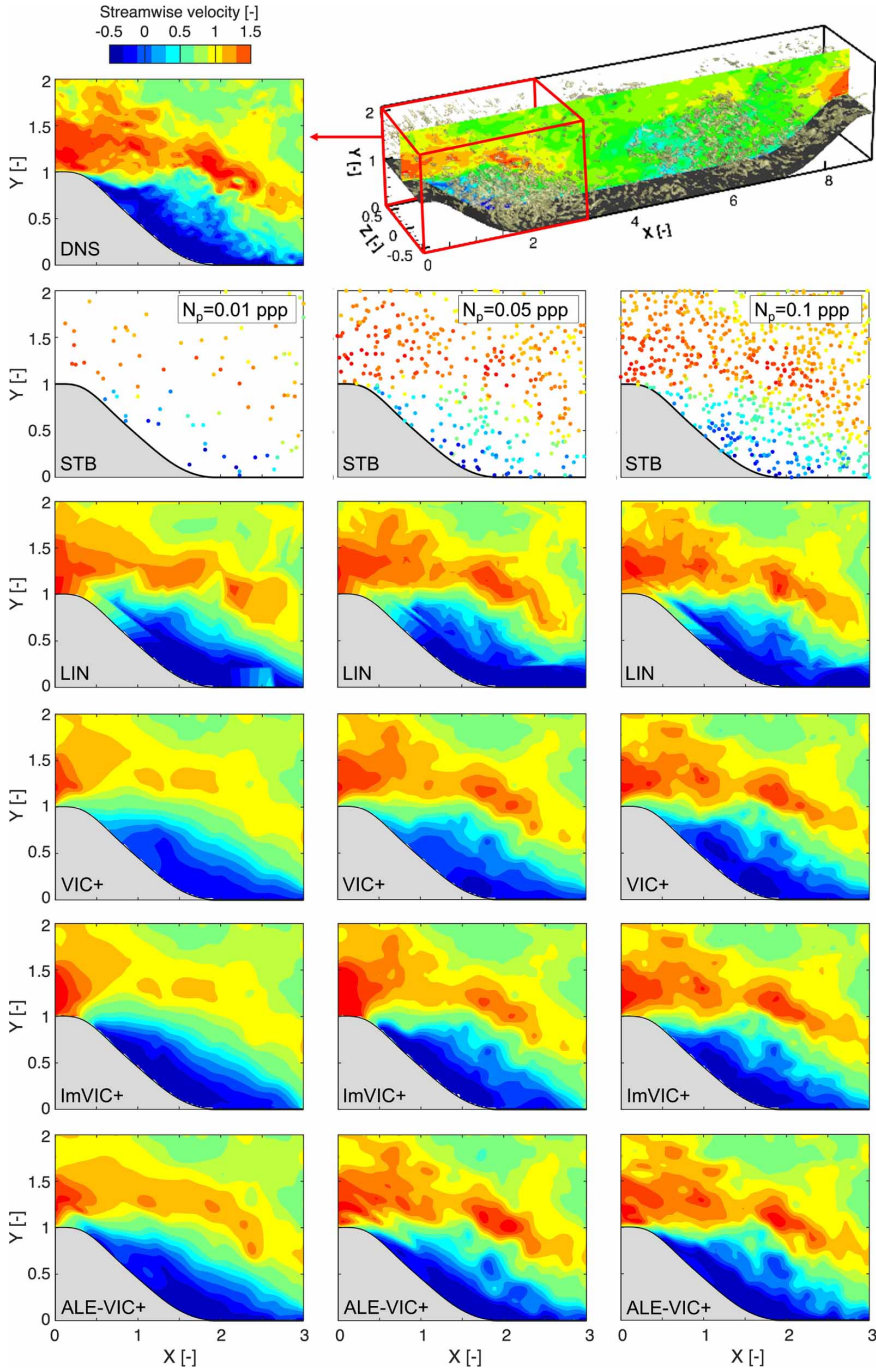
Figure 7.5: Instantaneous streamwise velocity distribution at the Z = 0 plane for the reference DNS results (1st row). Instantaneous particle distributions in a slab of $-0.25Z < 0.25h$, colour-coded by streamwise velocity (2nd row). Instantaneous streamwise velocity distributions at the Z = 0 plane obtained with tri-linear interpolation (3rd row), VIC+ (4th row), ImVIC+ (5th row) and ALE-VIC+ (6th row) at three different particle track concentrations of C = 25 par/h^3 (left), C = 125 par/ h^3 (middle) and C = 250 par/h^3 (right).
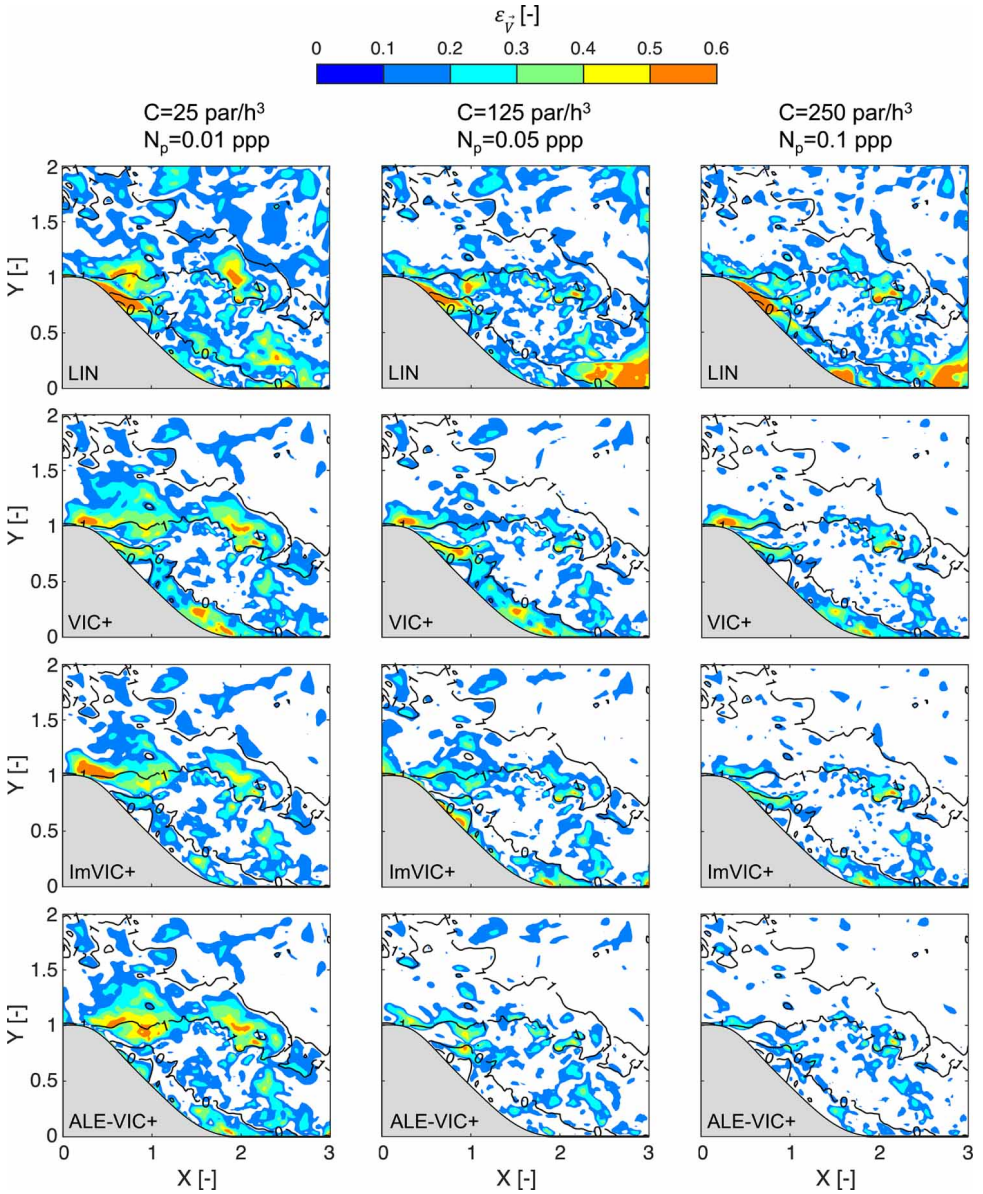
Figure 7.6: Planar distributions of velocity reconstruction error magnitudes overlayed with reference stream-wise velocity contour lines (u = 1 and u = 0, black) at Z = 0 plane obtained with tri-linear interpolation (1st row), VIC+ (2nd row), ImVIC+ (3rd row) and ALE-VIC+ (4th row) at three different particle track concentrations of C = 25 par/h^3 (left), C = 125 par/h^3 (middle) and C = 250 par/h^3 (right).
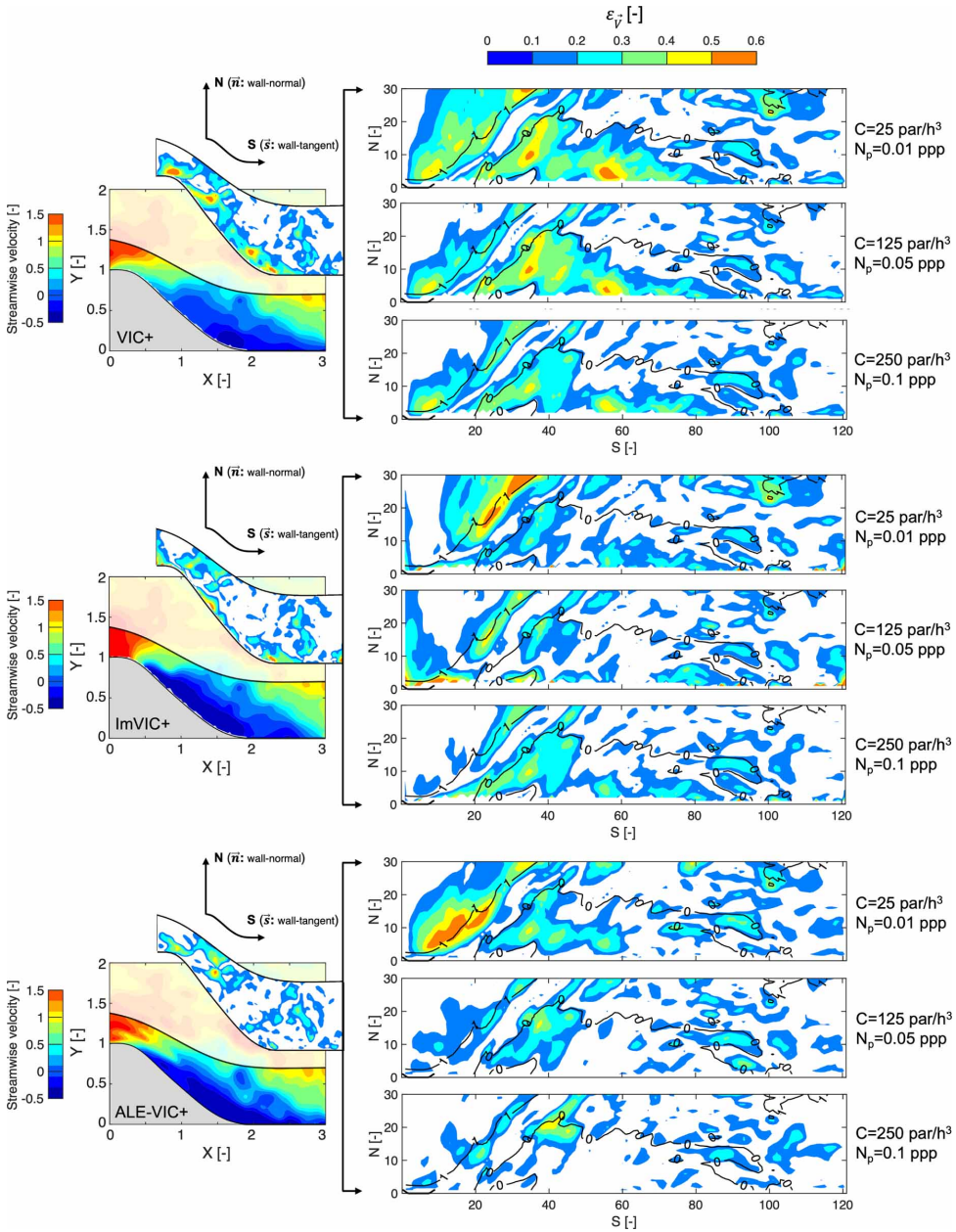
Figure 7.7: Planar distributions of velocity reconstruction errors overlaid with reference streamwise velocity contour lines (u = 1 and u = 0, black) at Z = 0 plane in close proximity of the surface (within the regions of interest indicated on the left column) obtained with VIC+ (top block), ImVIC+ (middle block) and ALE-VIC+ (bottom block) at different particle concentrations.

Accordingly, the reconstructed streamwise velocity distributions using both approaches

reveal accelerated flow behavior over the hill form and separation regions with recirculatory flow characteristics downstream of the hill. Nevertheless, the detailed flow structures of local high and low velocity magnitude variations are depicted with increased accuracy using the VIC+ based methods as the separation effects are captured with greater agreement to the reference solution. Furthermore, the superiority of VIC+ variants becomes even more apparent when the comparisons are performed over the particle concentrations $N_P \geqslant 0.05$ ppp (figure 7.5, middle and right). As the achievable resolution limits using data assimilation methods are strictly dominated by the interparticle distance of the available LPT data, low particle concentrations do not favor the excessive spatial resolution where the flow information beyond $\Delta h_{\min} = 0.25 C^{-1/3}$ is optimized without a proper cost function definition. Thus, increasing the particle concentrations while keeping the dense interpolation grid constant allows reconstruction of finer structures which demonstrates the ability of VIC+ based approaches to resolve the fluidic behavior with greater detail as well as preventing overestimation and underestimation errors by means of appropriate physical definitions.

Major differences between the original VIC+ and the proposed variants are observed especially in close proximity of the hill surface. The peak fluctuation magnitudes are resolved with a greater agreement to the reference simulations by employing both ALE-VIC+ and ImVIC+; conversely, the independence of VIC+ from the relevant surface structure caused overshoots and undershoots closer to the interface, which also propagated towards the regions further away from the surface (figure 7.5, 4th row). Although the dominant effect of the boundary treatments for VIC+ is observed over the streamwise velocity, mitigation of velocity reconstruction errors also denotes the modifications influencing both normal and spanwise components (figure 7.6). The differences in the error distributions tend to decrease significantly in regions away from the hill surface, because the influence of singularity elements decay with the Euclidean distance. However, the corrections due to immersed boundary treatment implemented by ImVIC+ have no influence on the spanwise velocity components. Considering the orientation of the surface elements for the hill form and the corresponding normal vector directions, there are two velocity components (streamwise and normal) of the flow motion that induce penetration of fluid particles through the hill surface. Accordingly, the application ImVIC+ provides modifications to the flow properties within those directions to prevent unphysical flow penetration through the surface by ensuring the satisfaction of no-through boundary condition. Since the spanwise velocity components do not affect the satisfaction of no-through boundary condition, the resultant superposition of potential and rotational velocity fields does not impose any alterations on the spanwise velocity magnitudes.

Moreover, the velocity error distributions at various heights from the hill surface demonstrate the error reduction achieved via ImVIC+ and ALE-VIC+ compared to linear interpolation and VIC+ (figure 7.7). The differences in error reductions become more distinguishable at higher seeding concentrations, with the ALE-VIC+ approach yielding the minimum errors in the near-wall region. The differences in grid locations between the uniform and conformal grids (figure 7.4) causes the path of the optimization process to vary between the two grid formations. Due to the extreme scarcity of particles in the low particle concentration case ($N_P = 0.01$ ppp), this difference causes variations of the reconstructed velocity field also away from the wall. The no-slip boundary condition

defined over the conformed hill surface restricts the capability of ALE-VIC+ to properly determine the velocity variations within the separation region, thus yielding underestimations of streamwise velocity at the crest of the hill (figure 7.5, left-6th row). At this low ppp value, only ImVIC+ reveals a significant improvement of the reconstruction accuracy over VIC+. Nevertheless, as the particle concentration is increased (N_P = 0.05 ppp), the perfectly conformed solid surface allows exact boundary conditions over the hill surface to be defined, thus enabling ALE-VIC+ to surpass the reconstruction accuracy of both VIC+ and ImVIC+ (figure 7.8-left). For the highest N_P value, the density of LPT information closer to the hill surface is considerably increased, which causes the accuracy gap between the ImVIC+ and VIC+ methods to collapse within a shorter range from the hill surface (figure 7.8, middle and right).
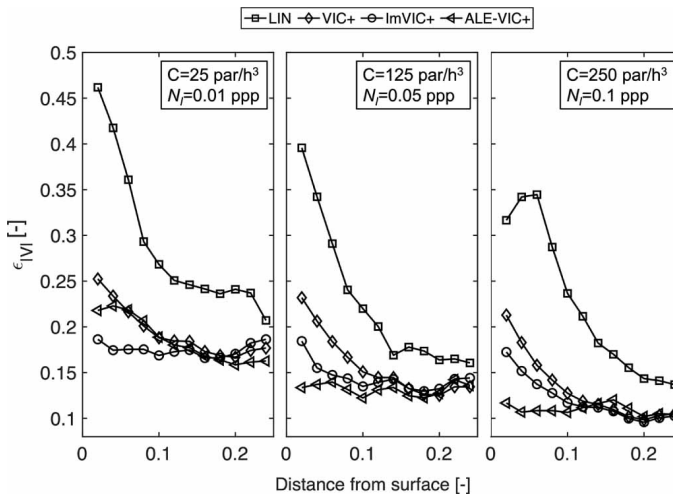
Figure 7.8: Velocity reconstruction errors extracted at various heights from the hill surface obtained with trilinear interpolation, VIC+, ImVIC+ and ALE-VIC+ at three different particle track concentrations of C = 25 par/h³ (left), C = 125 par/h³ (middle) and C = 250 par/h³ (right).

Finally, it should be noted that, whilst the modifications achieved by the proposed approaches are apparent both qualitatively and quantitatively, they are observed to be relatively mild. This is due two main reasons. Firstly, the periodic hill structure is located in close proximity of the computational domain boundaries. Secondly, the potential component of the flow is inferior in magnitude to the turbulent structures represented by means of the rotational component over the Helmholtz decomposition owing to the separation effects downstream of the hill. Accordingly, the corrections induced for the secondary flow structures of normal and spanwise flow components is relatively small which can be deduced from the correlation of velocity reconstruction errors correlating with the streamwise velocity components especially closer to the hill surface (figure 7.7). Furthermore, separation effects correspond to a turbulent flow behavior which cannot be resolved via potential flow definitions solely. Nonetheless, the appropriate combination of vortex-in-cell approach with the immersed boundary treatment provides the superposition of necessary potential and rotational flow components to reconstruct the

flow field properties with increased coherence levels to the physical flow behavior in close proximity of the hill surface.

7.4. EXPERIMENTAL ASSESSMENT

As a part of the HOMER (Holistic Optical Metrology for Aero-Elastic Research) European Union H2020 project, the experimental setup employed in this work, and already introduced in Chapter 3, is designed to investigate fluid-structure kinematics of turbulent boundary layer-unsteady panel interactions where the experiments are conducted in a low-speed wind tunnel of TU Delft High Speed Laboratory.

7.4.1. INSTANTANEOUS FLOW CHARACTERIZATION

Referring to the aforementioned discussion on the complete unsteady nature of FSI problems, the local closure of Collar's triangle of aeroelasticity demands a fully time-resolved characterization of the flow state. However, the employed large-scale experimental setup resulted in a tracer particle concentration of C = 100 par/δ_{99}^3 where the thickness of the fully developed turbulent boundary layer just upstream of the membrane was recorded as δ99 = 0.06 m (figure 7.13). Hence, with the corresponding image particle density of N_P = 0.002 ppp, the instantaneous flow field data suffers from scarcity of tracer particles which are also scattered over the measurement domain. Although the measurement volume has a size of $20 \times 20 \times 15 cm^3$, in order to reconstruct the flow properties where accurate description of boundary conditions is required, the region of interest (ROI) is restricted to a domain of $10 \times 10 \times 8 cm^3$, where sufficient particle concentration is obtained.The relative position of the ROI with respect to the elastic panel is demonstrated in figure 3.6 for different membrane deformation stages.

The structural motion of the membrane captured via the LPT system and STB algorithm is employed to reconstruct the membrane shape and deformation level both for steady (Fig. 3.6) and unsteady (Fig. 7.9) actuations. In order to quantify the accuracy of the structural motion reconstruction, the deformation of the central location of the membrane captured via the optical measurement setup is compared against the known actuation at the pressure tap location. Accordingly, figure 7.9 shows the comparison of measured and induced motion at three different frequencies (1 Hz, 3 Hz and 5 Hz) over one period of each motion cycle. The RMS error levels of the membrane central position over the actuated motion are below ≈0.8, ≈0.9 and ≈0.8 mm, respectively.

The instantaneous reconstruction characteristics are analyzed over the velocity and pressure information, by processing the time-resolved LPT data obtained for the steady and unsteady membrane deformations. For the steady deformation stages of the membrane, sampling rate for the instantaneous densely interpolated flow fields is determined based on the turbulent boundary layer profiles just upstream of the elastic membrane. The integral time scale is approximated by $T_I = \delta99/U_{inf}$. In accordance to the boundary layer properties obtained prior to this experimental campaign, the integral time scale is T_I = 0.06/10 = 6 ms. Hence, the corresponding optimal sampling rate is SR = $1/2T_I \approx 83$ Hz. As the measurements with steady membrane deformation are conducted for 3 cycles with 3 kHz acquisitions of 1 seconds each governed by the temporary storage allowance on the cameras, a total of ≈240 statistically independent time instants are post-
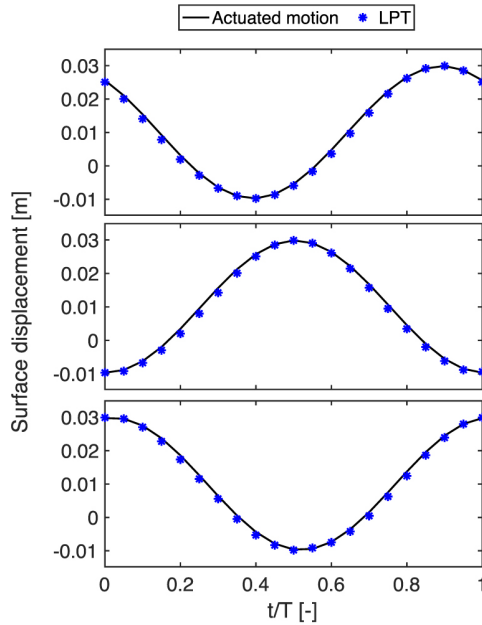
Figure 7.9: Surface deformation level of membrane central location captured via the LPT measurement system vs actuated motion by means of the DC motor-rod mechanism for actuation frequencies of 1 Hz (top), 3 Hz (middle) and 5 Hz (bottom).

7

processed with the data assimilation algorithms for statistical analysis of dense flow field interpolations. Moreover, in order to provide a reference for assessment of the reconstruction accuracy achieved with various data assimilation approaches, the available STB data computed from a total of 6000 time instants is ensemble-averaged over bins of r_{STB}= 2.5 mm ($r_{STB} = \Delta x$).
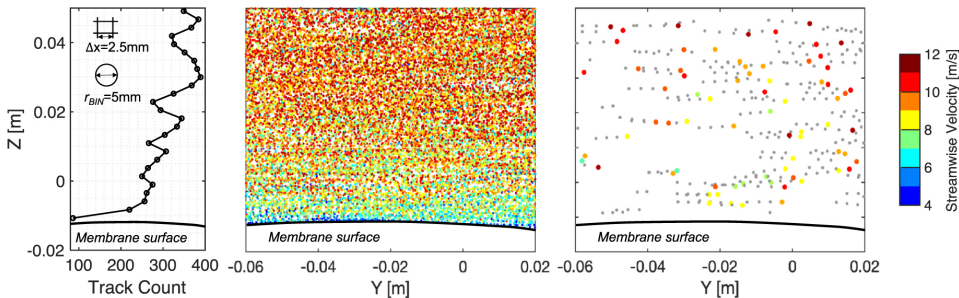
Figure 7.10: Number of particles captured over the central location of the membrane at downward deformation position for the ensemble of STB output (left). Available particle tracking information (color-coded by streamwise velocity) for phase averaged ensemble of STB output (middle) and instantaneous STB output (right). The grey particles denote the track history of the captured LPT data.
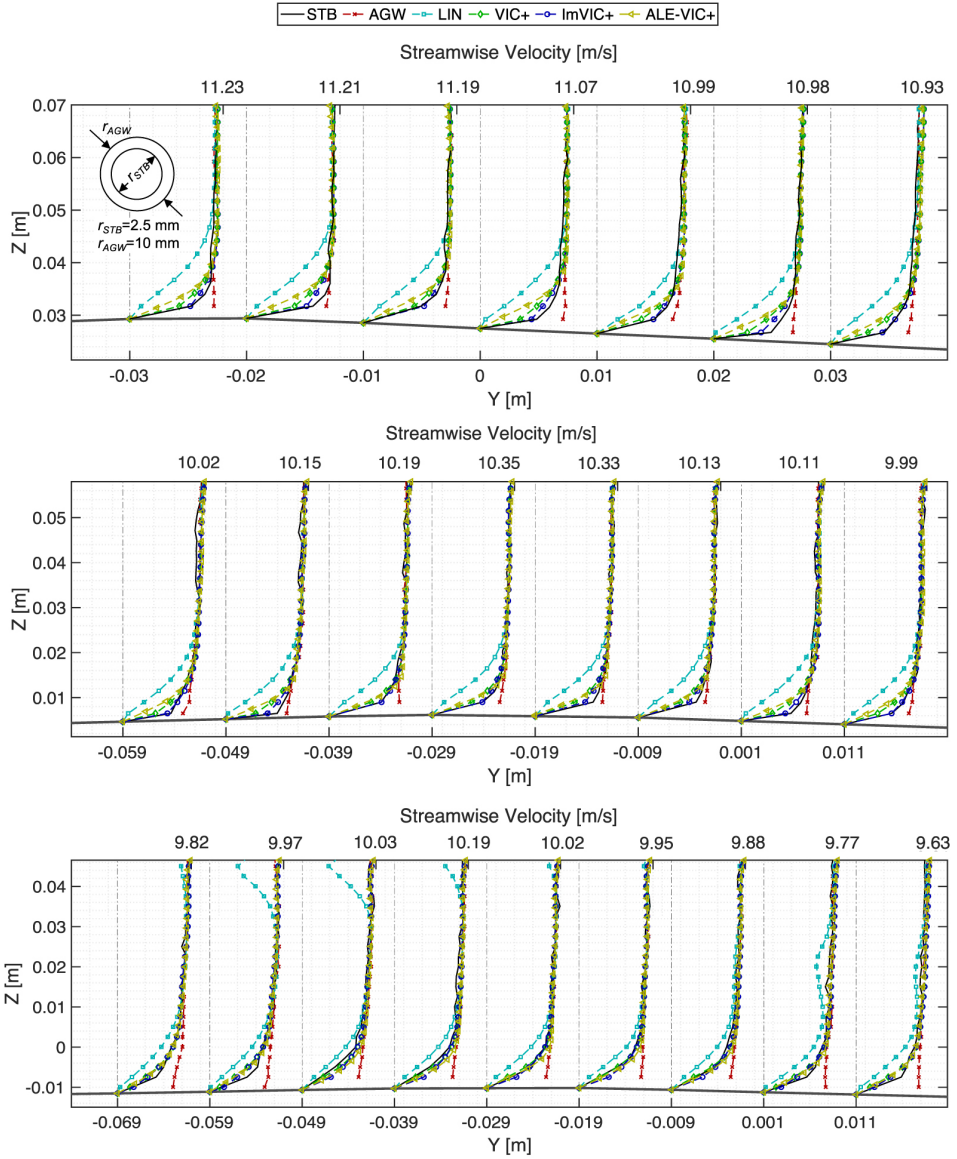
Figure 7.11: Time averaged streamwise velocity boundary layer profiles reconstructed over the membrane central axis with steady deformation stages of upward (top), neutral (middle) and downward (bottom) positions using EA-STB, AGW, linear interpolation, standard VIC+, ImVIC+ and ALE-VIC+ approaches.

The corresponding particle counts with a minimum of ≈250 tracks is regarded as a reliable source of information to represent the time averaged flow characteristics of the TBL interactions with the deformed membrane (Fig. 7.10-left). However, this can only be achieved for the steady cases due to the lower number of total measurements for the

unsteady deformations. Accordingly, the number of time instants corresponding to the upward, neutral and downward position of the membrane deformation stages for each frequency were determined by the membrane motion frequency for constant duration of measurement. Hence, the number of measurements are varied for different frequencies to match the total number of samples for each frequency. Therefore, a total 15 time instants are obtained for each membrane deformation stage for all three different motion frequencies of the membrane where the number of particles were too low to perform a reliable ensemble average.

7.4.2. VELOCITY FIELD RECONSTRUCTION

Initial investigations of the various data assimilation approaches are performed by extracting the time averaged streamwise velocity profiles within the turbulent boundary layers for steady and unsteady membrane deformations at upward, neutral and downward positions. Starting with the profiles obtained using the AGW method, the overestimation of the streamwise velocity values in close proximity to the membrane surface is apparent (figure 7.11). This is mainly attributed to the low availability of the particle tracks in the vicinity of the membrane surface. Due to the large size of spherical bins ($r_{AGW} = 10$ mm), the flow field information assigned to the grid locations close to the surface of the membrane are dominated by the particle tracks further away from the central location of the bins. Therefore, even though the influence of particle tracks are inversely related with Euclidean distance, frequent absence of any particles in the vicinity of the membrane causes the velocity values further away from the surface to dominate the resultant flow field data in close proximity to the surface.

On the other hand, linear interpolation provides the opposite characteristics with severe underestimations of the velocity profiles in close proximity to the membrane surface. This is again an influence of the scarcely present particle tracking data in close proximity of the membrane surface. Therefore, without any particles to provide the necessary velocity data in the lower layers of the turbulent boundary layers, the streamwise velocity magnitudes within the boundary layer profiles are significantly downgraded. Nevertheless, towards the locations further away from the membrane surface, the instantaneous availability of the particle tracking data increases which allows both linear interpolation and AGW to capture the boundary layer profiles with considerable accuracy. The improving accuracy towards the freestream is also a result of the physical characteristics of the turbulent boundary layers where the velocity gradients within the wall normal direction are concentrated in the vicinity of the membrane surface and possess considerably low amplitudes throughout the outer layers (Clauser, 1956).

Furthermore, as the ALE-VIC+ approach is used to reconstruct the dense flow field information, a boundary fitted grid structure is created where the membrane surface is conformed by the mesh formation. Since the boundary for the dense interpolation domain is defined over the membrane surface, a no-slip condition is required to be implemented as a boundary condition. Hence, the neglected viscosity effects within the vorticity transport equation and the absence of particles in close proximity of the membrane surface, the implementation of a no-slip boundary condition also caused the ALE-VIC+ approach to underestimate the velocity magnitudes closer to the membrane. Nevertheless, the underestimations of the streamwise velocity components are considerably

alleviated compared to the linear interpolation by means of the physics based interpolations of the VIC+ framework. This allowed the velocity gradients in close proximity of the membrane to be calculated with greater intensity compared to the linear interpolation which is also referred to as the more accurate resolution of turbulent boundary layers characteristics.
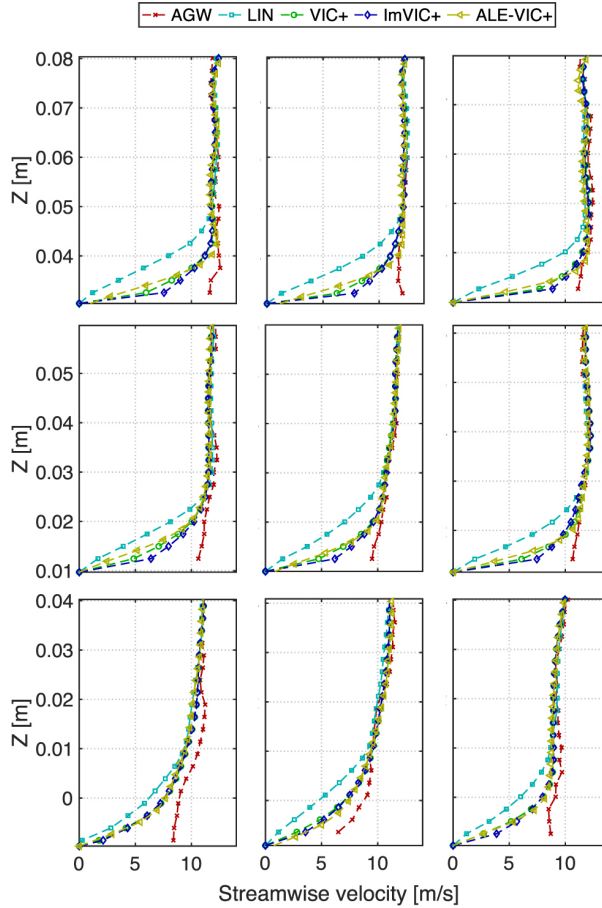
Figure 7.12: Time averaged streamwise velocity boundary layer profiles reconstructed over the membrane central axis with unsteady deformation stages of upward (top), neutral (middle) and downward (bottom) positions at 1 Hz (1st column), 3 Hz (2nd column) and 5 Hz (3rd column) using ensemble averaged STB, AGW, linear interpolation, standard VIC+, ImVIC+ and ALE-VIC+ approaches.

Moreover, the application of standard VIC+ and ImVIC+ method involves a similar approach of treating the lower boundary of the dense interpolation region which corresponds to the interior locations of the elastic membrane. Thus, the boundary conditions attributed to those locations do not necessarily refer to a no-slip boundary condition implementation over the membrane surface and allows the flow properties to vary according to the locally available particle tracking information. Therefore, especially through-

out locations over the membrane where the deformation displacements are large, the underestimations of streamwise velocity magnitudes are further diminished compared to ALE-VIC+ using the standard VIC+ approach (figure 7.11, top and figure 7.13, top). As the displacement amplitudes are reduced at the downward position of the membrane, the difference between the standard VIC+ and ALE-VIC+ is minimized since the grid layouts of the two approaches became almost identical. Hence, the resultant velocity boundary layer profiles revealed significant similarities between the standard VIC+ and ALE-VIC+ for steady and unsteady membrane deformation stage of downward position (Fig. 7.11, bottom and figure 7.13, bottom).

Furthermore, a similar comparison is also valid for between the ALE-VIC+ and ImVIC+ approaches in terms of the influence of a boundary condition imposition directly over the membrane surface. Nonetheless, the ImVIC+ approach provided the necessary acceleration on the streamwise velocity profile within the close proximity of the membrane surface. This is achieved by enforcing the no-through boundary condition which allows the immersed boundary treatment to incorporate the relevant physical impact of a solid boundary presence on the VIC+ framework. The intensity of the induced acceleration is elevated as the surface deformation is increased to create a greater curvature of the membrane, cambered towards the incoming flow field (figure 7.11, top and figure 7.12, top). Thus, the corresponding dense flow field interpolations are well adapted with ImVIC+ to the modifications on turbulent boundary layers due to the changing membrane shape. The significance of the implementation of the immersed boundary treatment is further highlighted as the modifications on the dense flow field over the standard VIC+ approach concentrated in the close vicinity of the surface where the absence of the particle tracks is considered as a major source of error that prevents capturing accurate boundary layer characteristics as deduced by Schneiders and Scarano (2016).

Finally, the physical characteristics of the turbulent boundary layers reconstructed at different membrane positions both with steady and unsteady deformations of the membrane are analyzed. The local cross sectional area of the flow streamlines are contracted as the intrusion of the membrane into to the flow field is increased from downward to upward deformation stages. Moreover, due the relatively low speed of the incoming flow ($M_\infty = 0.035 \ll 0.3$), the validity of incompressibility assumption is well preserved (Marchioro and Pulvirenti, 1994). Thus, the conservation of mass imposes an acceleration of the flow over the membrane surface, governed by the positive gradients of membrane displacement within the streamwise direction. Accordingly, the freestream velocity values are observed to be increasing with increasing deformation levels as expected for both steady and unsteady deformation cases (figures 7.11 and 7.13). Moreover, with the increasing velocities of the freestream values over the boundary layers, the boundary layers are contracted in size which is in agreement with the turbulent boundary layer theory (Schlichting and Gersten, 2017). Furthermore, the effect of elevated freestream velocity values and the reduced thickness of boundary layers are captured both between different deformation stages and locally over the membrane surface as the curvature of the membrane yields spatial variations of intrusion amplitudes towards the flow field.

A major difference is observed in terms of the velocity gradients especially in close proximity of the membrane surface between the steady and unsteady membrane deformation. As the membrane motion frequency is increased, the particle residence times

within the measurement domain become comparable with the membrane speed which is also observed as the reduced frequency transitions from quasi-steady to unsteady regimes as motion frequency is increased from 1 Hz to 5 Hz. Hence, for the 1 Hz case the effect of various membrane deformation stages becomes more profound which reduces as the motion frequency of membrane is increased where the difference between the boundary layer thicknesses at different stages of membrane motion also decreases. The gradual reduction of streamwise velocity gradients in the surface normal direction emphasizes this behavior especially for the upward deformation position where the variation of the velocity gradients and the corresponding boundary layer thickness is the greatest (Fig. 7.12).

7.4.3. PRESSURE FIELD RECONSTRUCTION

The pressure fields are computed by relating the material accelerations to the static pressure distributions over the Navier–Stokes equation (Marchioro and Pulvirenti, 1994) while neglecting the viscous diffusion terms due to the low order of magnitude, O(10-5), of their influence for turbulent flow conditions (Murai et al., 2007). While the VIC+-based data assimilation approaches already provided material acceleration information as an output of the dense interpolation scheme, the STB and linear interpolation based pressure information is computed by utilizing the raw material acceleration. For the STB, the acceleration terms are binned similar to the velocity, thus yielding the pressure gradient field from equation (7.15). For the linear interpolation, the raw acceleration data computed for the instantaneously available tracks is linearly interpolated within the spatial domain, which also yielded the pressure gradient information over the reconstruction volume. Then, the computation of pressure distribution over the measurement domain is performed by spatially integrating the pressure gradients by means of solving a Poisson equation accompanied with the proper boundary conditions due to its superior accuracy (Charonko et al., 2010).

$$\nabla^2 p = \nabla \cdot (\nabla p) = \nabla \cdot (-\rho \frac{D\mathbf{u}}{Dt}) \qquad (7.15)$$

The reconstruction of surface pressure over the non-uniformly deformed elastic membrane is performed utilizing two different approaches depending on the data-assimilation framework in use for elevating the spatial resolution characteristics. For the VIC+ and ImVIC+ employment, the rectangular uniform mesh formation is preserved throughout the data assimilation approach where the surface locations over the elastic membrane left hanging resulting in an intruding formation over the mesh structure. Hence, the pressure reconstruction is performed over the uniform Cartesian grid with masking the internal region of the solid intrusion. Then, the static pressure values over the exact surface locations are computed with an omni-directional integration procedure similar to the approach proposed by Jux, Sciacchitano, and Scarano (2020). In case of linear interpolation and ALE-VIC+ application, the resultant flow field information is represented over a boundary fitted grid structure conforming the membrane surface. Therefore, the pressure distribution over the membrane surface is computed using a reconstruction scheme with curvilinear transformations proposed by Çakir (2020). The letter approach enabled direct computation of the surface pressure alongside the global pressure infor-

mation without the need of external extrapolations.
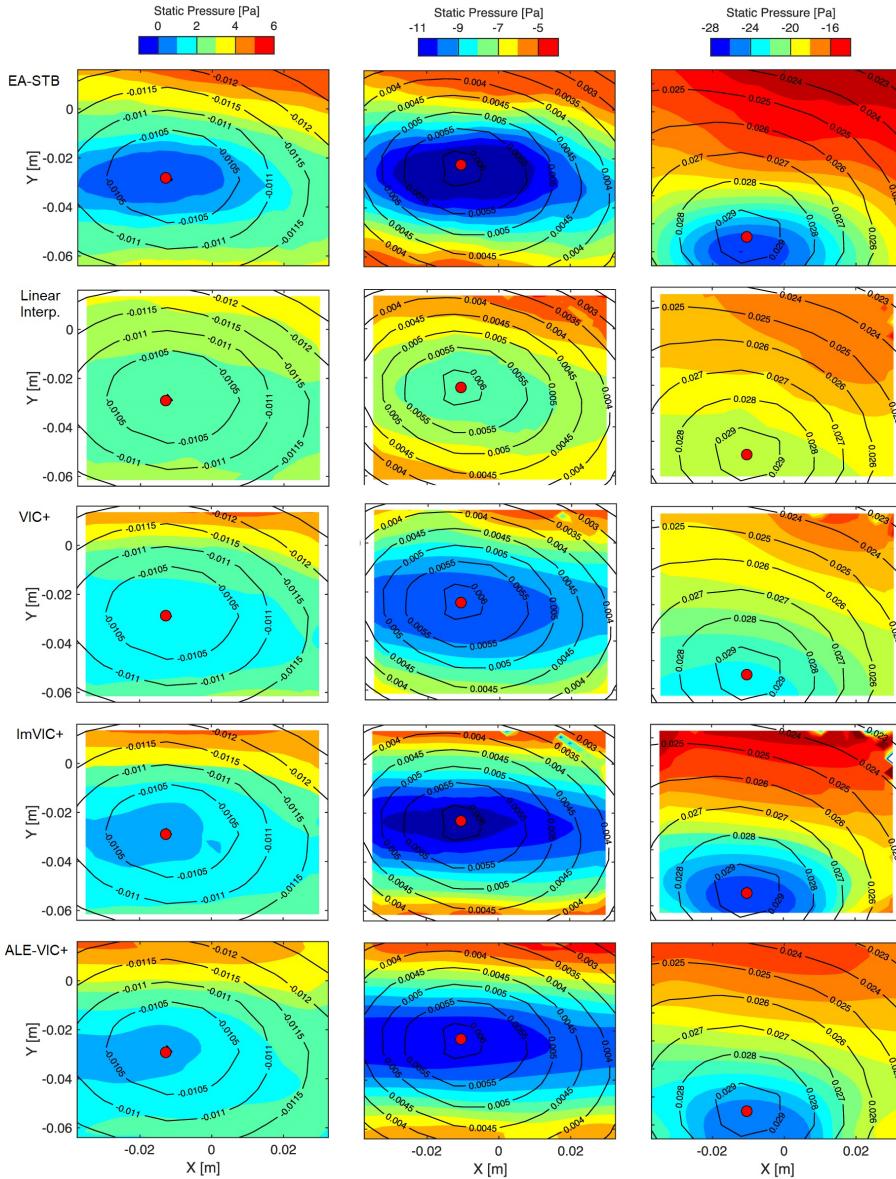
Figure 7.13: Time averaged pressure distributions reconstructed over the membrane surface with steady deformation stages of downward (left), neutral (middle) and upward (right) positions using EA-STB (1st row), linear interpolation (2nd row), standard VIC+ (3rd row), ImVIC+ (4th row) and ALE-VIC+ (5th row) approaches. Black contour lines with labels refer to the local distribution of membrane deformation levels in meters. Red dot indicates the pressure tap location.

Table 7.1: Steady static pressure values [Pa] at the central location of the membrane for different deformation stages obtained with pressure tap, EA-STB, linear interpolation, VIC+, ImVIC+ and ALE-VIC+.

Deformation stage	Upward	Neutral	Downward
Pressure tap	-25.8 ± 0.5	-10.8 ± 0.5	-0.8 ± 0.5
Ensemble-averaged STB	-25.9	-11.0	-0.8
Linear interpolation	-20.1	-8.7	2.2
VIC+	-22.5	-9.2	1.8
ImVIC+	-25.6	-10.9	0.7
ALE-VIC+	-24.2	-9.8	0.9

A significant improvement of accuracy and resolution is achieved by employing the VIC+ variants for the reconstruction of pressure information over the membrane surface. All VIC+ variants revealed similar properties in terms of capturing a lower pressure region towards the membrane central location. This corresponds to an accurate representation of the underlying physics of the problem where for all three deformation stages an upward curvature is present and the aforementioned acceleration in the direction of positive surface displacement gradients is accompanied with a reduction in static pressure (figure 3.6). Difference between the standard VIC+ approach and the proposed variants are observed to be amplified as the membrane deformation level increased. Nevertheless, even for the downward membrane position, a slight improvement in the reconstruction of pressure gradients is observed with both ALE-VIC+ and ImVIC+ over the standard VIC+ approach (figure 7.13, 3rd-5th columns-top). However, both proposed approaches are observed to be underestimating the pressure gradients over the membrane surface in comparison to the ensemble averaged STB data which yielded the static pressure at the center of the membrane to be overestimated with a value of ≈ 1.6 Pa (table 7.1).

Moreover, as the membrane's intrusion into the flow field is increased, amplitudes of the spatial pressure gradients over the membrane due to the variations in surface deformation levels are captured with elevated accuracy with both ALE-VIC+ and ImVIC+ methods (figure 7.13, 3rd-5th columns-middle and bottom). Owing to the presence of boundary layer profiles, the streamwise velocity distributions reveal to lower amplitudes over the central region of the membrane. The underestimations of streamwise velocity gradients in the surface normal direction in close proximity to the membrane surface associated with the application of linear interpolation and standard VIC+ deviate the flow field characteristics from the condition of zero pressure gradients in the surface normal direction which is valid for turbulent boundary layers (Fernholz and Finleyt, 1996). The violation of this assumption intensifies in the case of linear interpolations promoted by the increasing amplitude of velocity reconstruction errors. Hence, as the velocity gradients are computed locally from these velocity profiles the corresponding pressure gradients are completely inaccurate to capture the correct pressure distribution over the membrane surface. Nevertheless, employment of a surface treatment approach compensates the absence of particle tracks in the vicinity of the surface. In this regard, ImVIC+ provides lower deceleration over the central region of the membrane due to the modifications induced over the velocity field in order to satisfy the no through boundary

condition.

Similarly when the VIC+ variants are employed, velocity and vorticity gradients are discretized by means of locally defined finite difference approximations which compose the temporal and convective components of the material acceleration terms. Hence, as the governing equations of the VIC+ framework do not possess any terms to handle turbulence or viscosity, the corresponding material derivative computations become vulnerable against the inaccuracy issues related to the Eulerian approach whilst reconstructing dense flow field data within the turbulent boundary layers. Therefore, the accuracy of acceleration field reconstructions with VIC+ variants is dictated by the balance between the achievable mesh resolution and the dominant scale of the turbulent structures. Deriving an analogy to the large eddy simulations where the local mesh resolution is determined by the dominant large scales within the turbulence cascade (Schmitt, Richter, and Friedrich, 1986), VIC+ framework responds to the variations in flow velocity in a similar manner. In absence of any turbulent treatment, the mesh resolution of data assimilation acts as a low-pass filter removing the influence of sub-grid scale flow field variations from the densely interpolated velocity and acceleration data. However, the achievable mesh fidelity for the VIC+ variants is dictated by the instantaneous density of particle tracks which is a function of the experimental setup parameters and independent of the flow behavior. Therefore, in case of large scale vortical structures, the variations in the velocity field can be captured by the direct description of the vorticity transport equation which also yields more accurate reconstruction of the material acceleration terms (Van Gent et al., 2017).

Nonetheless, the influence of acceleration terms on the cost function is controlled by a scaling factor determined according to the relative standard deviations of velocity and acceleration terms. This is referred to as the balance between the aforementioned large and small scale flow field variation as well as an indication of their respective uncertainty levels. Therefore, the scaling factor strongly favors the velocity terms especially in case of turbulent boundary layers. Hence, even though the corresponding pressure gradients obtained from the VIC+ variants are substantially more accurate than the ones computed over an Eulerian approach, the influence of the Eulerian framework can be observed.

Comparing the surface pressure information over unsteady deformations of the membrane, the variations throughout the overall pressure profiles are observed to be relatively confined. Nevertheless, both ALE-VIC+ and ImVIC+ enabled a greater agreement with the pressure tab measurements by minor improvements (figure 7.14). Three main reasons can be deduced for these minor variations in correlation with the validation studies. First of all, the spatial gradients of both velocity and pressure over the measurement domain are dominated by the controlled motion of the elastic membrane. Hence, as the motion frequency of 1 Hz and 3 Hz corresponds to reduced frequencies of $k \leqslant 0.05$ (within the quasi-steady regime), these gradients can be reconstructed even with the linear interpolation without severe loss of accuracy. Secondly, considering the assumption of zero pressure gradients within the turbulent boundary layers and the membrane motion, the Dirichlet boundary condition dictates the majority of pressure variations in time. Although there exists non-zero pressure gradients throughout the realistic boundary layers, these relate to pressure modulations in the order of 6-8 Pa while the abso-

lute pressure difference captured at highest deformation state of the membrane is ≈30 Pa. Hence, the pressure variations aimed to be reconstructed with a superior accuracy by the proposed algorithms correspond to ≈25%. Lastly, the boundary conditions for VIC+, ALE-VIC+ and ImVIC+ methods are determined via linearly interpolating the STB data over the corresponding boundaries. Considering the close proximity of the Dirichlet boundary condition of pressure reconstruction to the computational domain boundaries of the VIC+ variants, the differences between the various approaches in terms of the absolute pressure values are further alleviated.
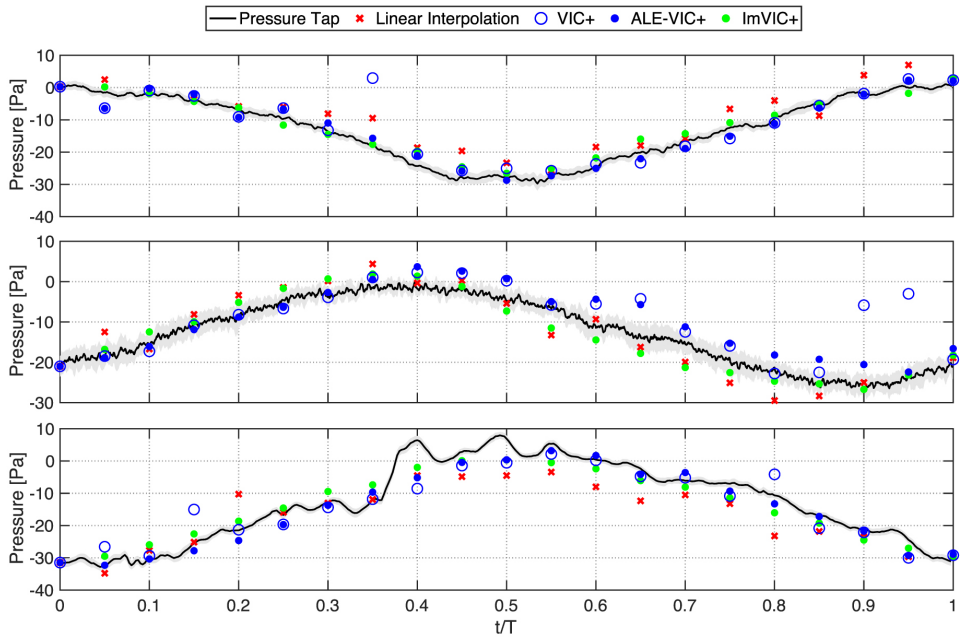
Figure 7.14: Instantaneous pressure reconstruction of linear interpolation, VIC+, ALE-VIC+ and ImVIC+ methods in comparison to the pressure tab measurements for 1 Hz (top), 3 Hz (middle) and 5 Hz (bottom) of unsteady membrane motion.

Finally, specific time instants are identified where the differences between VIC+ and the proposed variants are amplified with reconstruction errors up to ≈70% of the pressure fluctuation amplitudes obtained using VIC+. This is related to the extreme sensitivity of the standard VIC+ method to the spatial distribution of the available particle tracking information. In the absence of a proper boundary condition definition in close proximity of the elastic membrane, the VIC+ algorithm becomes strongly dependent on the presence of particles in the near wall regions to drive the optimization procedure towards an accurate solution which is a considerably rare situation in practical cases. Therefore, the ALE-VIC+ and ImVIC+ approaches provide the capability of accurately and consistently reconstructing the flow properties even in the cases of complete absence of particles in the near wall regions by providing a kinematic characterization of the solid boundary intrusions. The resultant accuracy improvements achieved by the

implementation of ALE-VIC+ and ImVIC+ over linear interpolation and VIC+ are also observed over the cumulative error levels over the pressure reconstruction profiles (Table 7.2).

Table 7.2: RMS of instantaneous pressure reconstruction errors [Pa] of linear interpolation, VIC+, ImVIC+ and ALE-VIC+ for 1 Hz, 3 Hz and 5 Hz of unsteady membrane motion.

Motion frequency	1 Hz	3 Hz	5 Hz
Linear interpolation	5.24	4.69	6.78
VIC+	4.96	5.01	5.26
ImVIC+	2.08	2.15	3.62
ALE-VIC+	2.14	2.12	4.04

7.5. CONCLUSIONS

Available spatial resolution characteristics for time-resolved flow field measurements with large scale LPT techniques are restricted due to the tracer particle specifications of HFSB tracers. However, the available governing equation based data assimilation techniques such as FlowFit (Gesemann et al., 2016) and VIC+ (Schneiders and Scarano, 2016) enable dense volumetric interpolations of flowfield information for regions of uniform rectangular computational domains with sole fluid presence. In this regard, the introduced variants of ALE-VIC+ and ImVIC+ provide the standard VIC+ algorithm with the capability of incorporating appropriate boundary condition definitions for dense flow field characterization in close proximity of solid objects with generic geometries. The ALE-VIC+ method implements the ALE method of fluid-structure interaction frameworks with a RBF based mesh deformation scheme to ensure the adaptability of the grid formations to the unsteady deformations of the FSI interface. On the other hand, ImVIC+ approach preserves FFT based Poisson solvers to increase computational efficiency using uniform predefined computational grids where immersed boundary treatments are utilized to satisfy the boundary conditions by means of additional flow components.

The validation studies of the proposed methods are performed with a numerical test case of flow over periodic hills, where the DNS datasets are manipulated to stimulate realistic experimental conditions. Even though, both linear interpolation and VIC+ variants resulted in coherent flow behaviors with the hill form, the local variations of velocity components favored the latter in terms of greater reconstruction accuracy. With the application of ALE-VIC+ and ImVIC+, reconstruction accuracy improvements over the standard VIC+ method are achieved especially in close proximity of the hill surfaces in terms of streamwise and normal velocity components composing the surface flow penetrations. Accuracy of the modifications are observed to be favoring the immersed boundary treatment approach with ALE-VIC+ containing additional numerical errors involved within the mesh transformation procedure (Lee and Tsuei, 1992) while preservation of uniform grid structures in the case of ImVIC+ enabled minimization of the computational cost. Furthermore, ImVIC+ achieved better compatibility with the standard VIC+ approach with modifications being confided to the close proximity of the hill surface where the scarcity of particle tracking information prevented the construction of an

7

accurate objective function for the optimization procedure.

Finally, both data assimilation approaches are applied to enable instantaneous flow field characterization for the measurements of turbulent boundary layer interactions with a dynamically deforming elastic membrane. The densely reconstructed flow field properties are then employed to compute the pressure distribution over membrane surface, revealing the time-resolved interaction between the flow structures and the membrane deformations. The ALE-VIC+ and ImVIC+ methods enabled the kinematic discretization of the unsteadily deforming membrane motion. Thus, the non-intrusive reconstruction of instantaneous velocity and pressure field computations are achieved compared to the trilinear interpolation and standard VIC+ approach. In comparison to surface pressure data, ImVIC+ approach also revealed a slight superiority of accuracy over ALE-VIC+ benefiting from the absence of numerical errors associated with curvilinear grids and the enforced no-slip boundary condition over the membrane surface. Nonetheless, this issue can be addressed by including the viscous terms in the NS equations provided that the particle concentrations and the corresponding spatial resolution is sufficient. In absence of these modifications, due to its versatile applicability to very complex geometries without tremendous increase of computational cost, makes ImVIC+ a potential method of choice over the ALE approach for providing physics-driven VIC+ method with the capability to accurately increasing the spatial resolution of the LPT data in the presence of generic solid boundaries.

7

8

CONCLUSIONS AND OUTLOOK

The unexamined life is not worth living.

Socrates

This is the concluding chapter of the dissertation. It gathers the most relevant scientific and technical implications of the work done throughout this period. First a summary of the conclusions of the chapters is provided. The chapter will close with an outlook toward future developments and needs for research in experimental aeroelasticity based on challenges encountered.

8.1. CONCLUSIONS

Lagrangian particle tracking has the potential to become a standard non-intrusive optical technique for aeroelastic characterization of complex phenomena. Obstacles, such as spatial resolution, accurate load determination, or strong establishment of other optical techniques, have prevented such standardization. The coming paragraphs gather the work done towards reducing or eliminating these obstacles.

The first step was reducing complexity of experimental setup, by integrating both flow and structural mechanics measurements under the same technique. A comparison between cross-correlation and tracking approaches was presented for structural displacement measurements. The experiment regarded an actuated flexible panel measured simultaneously by two different optical systems. The separation strategy followed was light frequency distinction. Results show that both techniques, LPT and DIC, perform very similarly when capturing the evolution of the moving surface, with the standard deviation of the differences being as low as 0.1% of the motion amplitude. Thus, it can be concluded that even if digital image correlation is the standard technique for displacement measurements, tracking approaches may substitute them in order to reduce the number of measurement apparatus and decrease experimental cost and complexity in general. Yet, it is true that the assessment of the techniques was performed at a single location of the surface, meaning no information about the spatial resolution is inferred. In this context and for the current experiment, DIC technique is expected to provide with a richer measurement, as the smallest scale is given by the interrogation window of the cross-correlation process. For the tracking approach, the detection of surfaces features are limited by the inter-marker distance, $d = 1$ cm for the current case. Nonetheless, large-scale FSI applications do not present scenarios where the structural motions or deformations are relatively large compared to the flow features they interact with, thus not requiring the spatial resolution of DIC technique.

LPT measurements have been shown to provide with the capability of measuring flow tracers and surface markers accurately. The remaining unknown is the accurate extraction of forces from experimental aeroelasticity by solely optical techniques. Therefore, a non-intrusive measurement methodology for aeroelastic experiments based on the Lagrangian particle tracking technique is proposed to simultaneously estimate aerodynamic, elastic and inertial loads from a deforming model. The method relies on the tracking of flow tracers to characterize the flow, and of surface markers to describe the dynamics of the structure. An experiment was carried out to show the applicability of the proposed methodology. The measurements regarded a flexible transparent foil attached to a solid cylinder and interacting with the wake of the latter. Both the flow tracers (neutrally-buoyant HFSB) and surface markers applied onto the panel were tracked in time with a single optical tomographic system. The results show the potential of evaluating the aeroelastic forces from Lagrangian Particle Tracking measurements of the flow tracers and the markers on the flexible structure. The inertia forces were successfully evaluated via time-derivation of the markers' displacements. The pressure on the foil surface was obtained extrapolating the solution of the Poisson problem from the outer flow field to the foil. The elastic forces required evaluation of the fourth spatial derivative of the displacement and turned out to be the most challenging quantity to determine. Flow analysis results show that pressure blobs associated with the Kármán vortices de-

termine the unsteady aerodynamic forcing. A phase shift exists between such external loading and the inertial and elastic response. The Collar closure criterion is introduced that considers the residual of the force equilibrium equation as a measure of the accuracy of the overall experiment. The criterion yields unfavourable results close to the foil root where displacement and acceleration are vanishing. At the foil trailing edge a consistent combination of the aeroelastic forces is observed, indicating the feasibility of the present optical diagnostic approach for aeroelastic systems characterisation.

Following the work of the flagged cylinder, an experimental study on the flow around a flexible foil attached to a cylinder was presented. LPT is performed on surface markers and flow tracers to measure the effect of the flexible foil on the flow around it, i.e. the cylinder wake. Several regimes of foil motion were imaged and identified in the range of free stream velocities $10^4 < Re < 10^5$. Based on the amplitude and the span-wise coherence of the plate motion, the regimes were classified into 4 categories: low oscillations, resonance, chaotic, and bi-stable. A statistical analysis was carried out for two aeroelastic regimes, the resonant and the chaotic. Proper Orthogonal Decomposition was applied to study the most dominant modes from each flow. Based on the latter analyses, two different coupling mechanisms were identified pertaining to the different aeroelastic regimes. For the resonant regime, the presence of the trailing foil did not disrupt the predominant two-dimensional motion. This regime occurs when the frequency of the vortex shedding coincides with the first natural frequency of the foil, corresponding to the first bending mode. Overall, the results showed a one-way coupling between the flow and the foil, meaning that the motion of the foil was driven by the dominant features of the flow, whereas the flow was mostly unaffected by the presence of the foil. Slight differences between the clean cylinder flow and the cylinder-foil flow, especially at the root of the foil, can be explained by the weak structural damping of the foil. Conversely, the chaotic regime is an example of full interaction, i.e. 2-way coupling between flow and structure. The cylinder flow at that freestream speed displayed a predominant two-dimensional flow, characteristic to sub-critical cylinder flow below $Re < 3 \times 10^5$. The results showed that the addition of the foil completely disrupted the cylinder wake by enhancing the span-wise flow oscillations and so, the three dimensional features of the wake.

The combination of particle tracking velocimetry with hellium-filled soap bubbles conveys accurate, yet gappy, data that experiences from reduced spatial resolution when scaling the technique to large-scale. Data assimilation plays an important role to increase spatial resolution of PIV data when gridding the scattered information. In this thesis, a data assimilation technique has been introduced that considers data distributed over a finite time-segment to reconstruct the optimal 3D vorticity and velocity fields described within such segment. The technique is coupled to the Vortex-in-Cell paradigm to produce a dense reconstruction of the velocity field based on spatially sparse measurements of tracers' trajectories. A first-principle analysis indicates the potential of VIC-TSA in terms of spatial resolution, by identifying three main data reduction regimes, namely impulsive, adjacent tracks and stringy. A numerical analysis that follows the approach presented in the literature is carried in a 3D lattice of sinusoids, where the velocity amplitude modulation is inspected for varying conditions of tracers concentration, sinusoids wavelength and, most importantly, time-segment length. The cut-off of am-

plitude reconstruction is delayed when the time-segment increases, consistently with the hypotheses formulated in the first-principle analysis. Experiments are conducted with large-scale PIV, where the wake of a circular cylinder at $Re_D = 27,000$ is measured using helium-filled soap bubbles and a tomographic imaging system comprising three high-speed cameras. The tracers motion analysis is delivered using the Shake-the-Box algorithm, and the database of particle trajectories is examined using VIC-TSA. The statistical analysis of vorticity fluctuations reveals that the modulation of vortex structures reconstructed by VIC-TSA decreases as the time-segment is made longer. An optimum trade-off between spatial resolution and computational burden is identified with the criterion $\tau^* = 2$, i.e. twice the value of adjacent tracks regime. The topology analysis of the vortex structure confirms the salient features of the Kármán wake with sub-structures being resolved at a scale comparable to the average inter-particle distance.

In FSI measurements, the available information close to the solid boundaries of the models is limited. However, in contrast to pure flow domains, temporal information is not enough to fill in the gaps between the flow domain and the solid boundaries. In this regard, the introduced variants of ALE-VIC+ and ImVIC+ provide the standard VIC+ algorithm with the capability of incorporating appropriate boundary condition definitions for dense flow field characterization in close proximity of solid objects with generic geometries. The ALE-VIC+ method implements the ALE method of fluid-structure interaction frameworks with a RBF based mesh deformation scheme to ensure the adaptability of the grid formations to the unsteady deformations of the FSI interface. On the other hand, ImVIC+ approach preserves FFT based Poisson solvers to increase computational efficiency using uniform predefined computational grids where immersed boundary treatments are utilized to satisfy the boundary conditions by means of additional flow components. The validation studies of the proposed methods are performed with a numerical test case of flow over periodic hills, where the DNS datasets are manipulated to stimulate realistic experimental conditions. Even though, both linear interpolation and VIC+ variants resulted in coherent flow behaviors with the hill form, the local variations of velocity components favored the latter in terms of greater reconstruction accuracy. With the application of ALE-VIC+ and ImVIC+, reconstruction accuracy improvements over the standard VIC+ method are achieved especially in close proximity of the hill surfaces in terms of streamwise and normal velocity components composing the surface flow penetrations. Accuracy of the modifications are observed to be favoring the immersed boundary treatment approach with ALE-VIC+ containing additional numerical errors involved within the mesh transformation procedure while preservation of uniform grid structures in the case of ImVIC+ enabled minimization of the computational cost. Furthermore, ImVIC+ achieved better compatibility with the standard VIC+ approach with modifications being confided to the close proximity of the hill surface where the scarcity of particle tracking information prevented the construction of an accurate objective function for the optimization procedure. Finally, both data assimilation approaches are applied to enable instantaneous flow field characterization for the measurements of turbulent boundary layer interactions with a dynamically deforming elastic membrane. The densely reconstructed flow field properties are then employed to compute the pressure distribution over membrane surface, revealing the time-resolved interaction between the flow structures and the membrane deformations. The ALE-VIC+

and ImVIC+ methods enabled the kinematic discretization of the unsteadily deforming membrane motion. Thus, the non-intrusive reconstruction of instantaneous velocity and pressure field computations are achieved compared to the trilinear interpolation and standard VIC+ approach. In comparison to surface pressure data, ImVIC+ approach also revealed a slight superiority of accuracy over ALE-VIC+ benefiting from the absence of numerical errors associated with curvilinear grids and the enforced no-slip boundary condition over the membrane surface. Nonetheless, this issue can be addressed by including the viscous terms in the NS equations provided that the particle concentrations and the corresponding spatial resolution is sufficient. In absence of these modifications, due to its versatile applicability to very complex geometries without tremendous increase of computational cost, makes ImVIC+ a potential method of choice over the ALE approach for providing physics-driven VIC+ method with the capability to accurately increasing the spatial resolution of the LPT data in the presence of generic solid boundaries.

8.2. OUTLOOK

Today, Lagrangian particle tracking is closer to become the common integrated non-intrusive measurement technique for aeroelastic loads. The process of making this possible made evident some of the challenges to overcome with future research.

Tracking simultaneously flow tracers and surface markers with a single optical system reduce considerably the complexity of the experimental apparatus. However, aeroelastic characterization with the minimum resources always give more headaches than dehydration. In order to understand the full interaction of aeroelastic phenomena, it is required camera view all around the object, for both marker tracking and aerodynamic load estimation. The latter condition is even more restrictive when the body deforms. In chapter 4, given the availability of cameras, a bypass was taken by choosing a transparent material for the flexible splitter plate. The solution allowed to track particles through the deforming body. However, a portion of the particles was not tracked due to intensity loss through the material. The ideal situation would require of an arrangement of cameras able to capture the domain all around the body. Yet it is true, LPT measurements through deforming transparent materials have been demostrated in chapters 4 and 5, and open the door to full-field measurements together with surface marker tracking of micro-air vehicles (MAV) such as Delfly (De Croon et al., 2016).

Capturing both flow and solid walls in the same images requires of a separation strategy in the processing stage. This is the case until processing algorithms are able to handle and process all species, markers and tracers, in a single step, by increasing the dynamic range of the methods. Meanwhile, separation schemes depend on behavioral or geometrical characteristics. In large-scale applications, species' velocity differs considerably (the velocity of flow tracers is much higher than that of structural markers), being this approach the most convenient. However, in small scale applications such as MAV regimes or propulsive scenarios, flow particles and solid bodies tend to have similar velocities, and so separation by geometry is required. In chapter 4, separation of species was achieved geometrically by computing a different optical transfer function for each of them. In this case, the experimental conditions, such as bottom illumination, favoured a vertically-elongated shape for the HFSB (due to the glare points) in contrast to the per-

fect circular shape of the surface markers. This situation is very case-dependent, and so, an unreliable approach to separate species. Therefore, it is encouraged the active geometrical distinction between flow tracers and surface markers, having the latter more freedom to be configured.

Load determination from marker tracking is the most challenging step for closing Collar's triangle, in particular the elastic force. Such fact is related to the dependency on the 4th spatial derivative of the shape. Chapter 4 showed that the marker spacing chosen for the description of the surface was not enough to achieve an accurate elastic load along the foil. Ideally, in order to optimize the accuracy of the elastic force determination, that is the spatial derivatives of the surface, spatial resolution should increase dramatically. However, this could interfere with the tracking algorithm, if the limit on image density is reached. The challenge of the accurate determination of elastics could be solved by fitting a model to the measured structural data. By doing so, the elastic load uncertainty would depend on the fidelity of the model, which would require extra effort in the experimental chain.

Finally, data assimilation conform a field of challenges by itself due to its close relation to the combination of computational fluid dynamics and solid mechanics environments. Earlier it was mentioned the possibility of handling all tracked species together in the same processing step; thus reducing the time and cost of the processing stage. The output encourages new data assimilation techniques focused on aeroelasticity. A devised path at this stage would be Arbitrary Lagrangian Eulerian Time segment Assimilation (ALE-TSA). Some aspects such as identification of solid boundaries among the tracked particles, choice of solid mechanics models, or the coupling at the solid-fluid inter-phase require enough effort to fill a PhD dissertation by themselves. Nonetheless, data assimilation has proven to be the perfect symbiosis between experimental efforts and computational approaches, guaranteeing its relevance in aeroelasticity for the coming decades.

8

BIBLIOGRAPHY

Abdi, Ali, Seyyed Ahmad Hosseini, and Helmut Podhaisky (2019). "Adaptive linear barycentric rational finite differences method for stiff ODEs". In: *Journal of Computational and Applied Mathematics* 357, pp. 204–214.

Adrian, Ronald J and Jerry Westerweel (2011). *Particle image velocimetry*. 30. Cambridge university press.

Agüí, Juan C and J Jimenez (1987). "On the performance of particle tracking". In: *Journal of fluid mechanics* 185, pp. 447–468.

Allen, JJ and AJ Smits (2001). "Energy harvesting eel". In: *Journal of fluids and structures* 15.3-4, pp. 629–640.

Apelt, CJ, GS West, and Albin A Szewczyk (1973). "The effects of wake splitter plates on the flow past a circular cylinder in the range 104< R< 5× 104". In: *Journal of Fluid Mechanics* 61.1, pp. 187–198.

Arroyo, MP and CA Greated (1991). "Stereoscopic particle image velocimetry". In: *Measurement science and technology* 2.12, p. 1181.

Ashmore, David W et al. (2022). "Proper orthogonal decomposition of ice velocity identifies drivers of flow variability at Sermeq Kujalleq (Jakobshavn Isbræ)". In: *The Cryosphere* 16.1, pp. 219–236.

Assi, Gustavo RS and Peter W Bearman (2015). "Transverse galloping of circular cylinders fitted with solid and slotted splitter plates". In: *Journal of Fluids and Structures* 54, pp. 263–280.

Assi, Gustavo RS, Peter W Bearman, and Michael A Tognarelli (2014). "On the stability of a free-to-rotate short-tail fairing and a splitter plate as suppressors of vortex-induced vibration". In: *Ocean engineering* 92, pp. 234–244.

Balcaen, Ruben et al. (2017). "Stereo-DIC uncertainty quantification based on simulated images". In: *Experimental Mechanics* 57, pp. 939–951.

Bartlett, Maurice S (1950). "Periodogram analysis and continuous spectra". In: *Biometrika* 37.1/2, pp. 1–16.

Beale, J Thomas and Claude Greengard (1994). "Convergence of euler-stokes splitting of the navier-stokes equations". In: *Communications on Pure and Applied Mathematics* 47.8, pp. 1083–1115.

Beckert, Armin and Holger Wendland (2001). "Multivariate interpolation for fluid-structure-interaction problems using radial basis functions". In: *Aerospace Science and Technology* 5.2, pp. 125–134.

Beresh, Steven J (2021). "Time-resolved particle image velocimetry". In: *Measurement Science and Technology* 32.10, p. 102003.

Berkooz, Gal, Philip Holmes, and John L Lumley (1993). "The proper orthogonal decomposition in the analysis of turbulent flows". In: *Annual review of fluid mechanics* 25.1, pp. 539–575.

BHATIA, KUMAR and Jiri Wertheimer (1993). "Aeroelastic challenges for a high speed civil transport". In: *34th Structures, Structural Dynamics and Materials Conference*, p. 1478.

Bhattacharya, Sayantan and Pavlos P Vlachos (2020). "Volumetric particle tracking velocimetry (PTV) uncertainty quantification". In: *Experiments in Fluids* 61, pp. 1–18.

Bisplinghoff, Raymond L and Holt Ashley (2013). *Principles of aeroelasticity*. Courier Corporation.

Bleischwitz, Robert, Roeland De Kat, and Bharathram Ganapathisubramani (2017). "On the fluid-structure interaction of flexible membrane wings for MAVs in and out of ground-effect". In: *Journal of Fluids and Structures* 70, pp. 214–234.

Blevins, Robert D (1977). "Flow-induced vibration". In: *New York*.

Bloor, M Susan (1964). "The transition to turbulence in the wake of a circular cylinder". In: *Journal of Fluid Mechanics* 19.2, pp. 290–304.

Bodnár, Tomáš, Giovanni P Galdi, and Šárka Nečasová (2014). *Fluid-structure interaction and biomedical applications*. Springer.

Bosbach, Johannes, Matthias Kühn, and Claus Wagner (2009). "Large scale particle image velocimetry with helium filled soap bubbles". In: *Experiments in fluids* 46, pp. 539–547.

Brennen, Christopher E (2005). "Fundamentals of multiphase flow". In.

Brigham, E Oran (1988). *The fast Fourier transform and its applications*. Prentice-Hall, Inc.

Bushnell, Dennis M (2006). "Scaling: Wind tunnel to flight". In: *Annu. Rev. Fluid Mech.* 38, pp. 111–128.

Çakir, Bora (2020). "Bridging experimental simulations with computational frameworks for time-resolved characterization of fluid-structure interactions". In.

Cardell, GS (1993). "Flow past a circular cylinder with a permeable splitter plate". In: *California Institute of Technology*.

Carrera, Erasmo and Enrico Zappino (2014). "Aeroelastic analysis of pinched panels in supersonic flow changing with altitude". In: *Journal of Spacecraft and Rockets* 51.1, pp. 187–199.

Chandramouli, Pranav, Etienne Mémin, and Dominique Heitz (2020). "4D large scale variational data assimilation of a turbulent flow with a dynamics error model". In: *Journal of Computational Physics* 412, p. 109446.

Charonko, John J et al. (2010). "Assessment of pressure field calculations from particle image velocimetry measurements". In: *Measurement Science and technology* 21.10, p. 105401.

Chatterjee, Anindya (2000). "An introduction to the proper orthogonal decomposition". In: *Current science*, pp. 808–817.

Chen, Shoei-Sheng (1985). *Flow-induced vibration of circular cylindrical structures*. Tech. rep. Argonne National Lab.(ANL), Argonne, IL (United States).

Chen, Zhen Li et al. (2014). "Wall modeling for implicit large-eddy simulation and immersed-interface methods". In: *Theoretical and Computational Fluid Dynamics* 28, pp. 1–21.

Christiansen, IP (1973). "Numerical simulation of hydrodynamics by the method of point vortices". In: *Journal of Computational Physics* 13.3, pp. 363–379.

Cimbala, John M and Jonathan Leon (1996). "Drag of freely rotatable cylinder/splitter-plate body at subcritical Reynolds number". In: *AIAA journal* 34.11, pp. 2446–2448.

Clauser, Francis H (1956). "The turbulent boundary layer". In: *Advances in applied mechanics* 4, pp. 1–51.

Collar, A Ro (1946). "The expanding domain of aeroelasticity". In: *The Aeronautical Journal* 50.428, pp. 613–636.

Cottet, G-H and Philippe Poncet (2004). "Advances in direct numerical simulations of 3D wall-bounded flows by vortex-in-cell methods". In: *Journal of computational physics* 193.1, pp. 136–158.

Cottet, Georges-Henri, Petros D Koumoutsakos, et al. (2000). *Vortex methods: theory and practice*. Vol. 8. Cambridge university press Cambridge.

Coutanceau, Madeleine and Jean-Rene Defaye (1991). "Circular cylinder wake configurations: A flow visualization survey". In.

De Boer, Aukje, Martijn S Van der Schoot, and Hester Bijl (2007). "Mesh deformation based on radial basis function interpolation". In: *Computers & structures* 85.11-14, pp. 784–795.

De Croon, GCHE et al. (2016). "The delfly". In: *Dordrecht: Springer Netherlands. doi* 10, pp. 978–94.

De Figueiredo, HV et al. (2021). "Aeroelastic vibration measurement based on laser and computer vision technique". In: *Experimental Techniques* 45, pp. 95–107.

De Kat, R and BW Van Oudheusden (2012). "Instantaneous planar pressure determination from PIV in turbulent flow". In: *Experiments in fluids* 52, pp. 1089–1106.

De Nayer, Guillaume and Michael Breuer (2014). "Numerical FSI investigation based on LES: Flow past a cylinder with a flexible splitter plate involving large deformations (FSI-PfS-2a)". In: *International Journal of Heat and Fluid Flow* 50, pp. 300–315.

De Nayer, Guillaume et al. (2014). "Flow past a cylinder with a flexible splitter plate: A complementary experimental–numerical investigation and a new FSI test case (FSI-PfS-1a)". In: *Computers & Fluids* 99, pp. 18–43.

Den Hartog, Jacob Pieter (1985). *Mechanical vibrations*. Courier Corporation.

Dimitriadis, Grigorios and Jonathan E Cooper (2001). "Flutter prediction from flight flutter test data". In: *Journal of Aircraft* 38.2, pp. 355–367.

Dowell, Earl, John Edwards, and Thomas Strganac (2003). "Nonlinear aeroelasticity". In: *Journal of aircraft* 40.5, pp. 857–874.

Dowell, Earl H (2014). *A modern course in aeroelasticity*. Vol. 217. Springer.

Dowell, Earl H et al. (2021). *A modern course in aeroelasticity*. Springer.

Ehlers, Frithjof, Andreas Schröder, and Sebastian Gesemann (2020). "Enforcing temporal consistency in physically constrained flow field reconstruction with FlowFit by use of virtual tracer particles". In: *Measurement Science and Technology* 31.9, p. 094013.

Elsinga, Gerrit E et al. (2006). "Tomographic particle image velocimetry". In: *Experiments in fluids* 41.6, pp. 933–947.

Faleiros, David Engler et al. (2018). "Helium-filled soap bubbles tracing fidelity in wall-bounded turbulence". In: *Experiments in Fluids* 59.3, p. 56.

Farhat, Charbel, Michael Lesoinne, and Patrick Le Tallec (1998). "Load and motion transfer algorithms for fluid/structure interaction problems with non-matching discrete interfaces: Momentum and energy conservation, optimal discretization and applica-

tion to aeroelasticity". In: *Computer methods in applied mechanics and engineering* 157.1-2, pp. 95–114.

Fernholz, HH and PJ Finleyt (1996). "The incompressible zero-pressure-gradient turbulent boundary layer: an assessment of the data". In: *Progress in Aerospace Sciences* 32.4, pp. 245–311.

Ferziger, Joel H, Milovan Perić, and Robert L Street (2019). *Computational methods for fluid dynamics*. springer.

Fujarra, André Luis Condino et al. (2001). "Vortex-induced vibration of a flexible cantilever". In: *Journal of Fluids and Structures* 15.3-4, pp. 651–658.

Fung, Yuan Cheng (2008). *An introduction to the theory of aeroelasticity*. Courier Dover Publications.

Gao, Chuanqiang and Weiwei Zhang (2020). "Transonic aeroelasticity: A new perspective from the fluid mode". In: *Progress in Aerospace Sciences* 113, p. 100596.

Gerrard, JH (1966). "The mechanics of the formation region of vortices behind bluff bodies". In: *Journal of fluid mechanics* 25.2, pp. 401–413.

Gesemann, Sebastian et al. (2016). "From noisy particle tracks to velocity, acceleration and pressure fields using B-splines and penalties". In: *18th international symposium on applications of laser and imaging techniques to fluid mechanics, Lisbon, Portugal*. Vol. 4. 7.

Göge, Dennis et al. (2007). "Ground vibration testing of large aircraft–state-of-the-art and future perspectives". In: *25th International Modal Analysis Conference*.

Guo, Chang Qin and Michael P Païdoussis (2000). "Stability of rectangular plates with free side-edges in two-dimensional inviscid channel flow". In: *J. Appl. Mech.* 67.1, pp. 171–176.

Hamlehdar, Maryam, Alibakhsh Kasaeian, and Mohammad Reza Safaei (2019). "Energy harvesting from fluid flow using piezoelectrics: A critical review". In: *Renewable Energy* 143, pp. 1826–1838.

Hansen, Morten H (2007). "Aeroelastic instability problems for wind turbines". In: *Wind Energy: An International Journal for Progress and Applications in Wind Power Conversion Technology* 10.6, pp. 551–577.

Helenbrook, Brian T (2003). "Mesh deformation using the biharmonic operator". In: *International journal for numerical methods in engineering* 56.7, pp. 1007–1021.

Hess, John L and A_M O Smith (1967). "Calculation of potential flow about arbitrary bodies". In: *Progress in Aerospace Sciences* 8, pp. 1–138.

Hübner, Björn, Elmar Walhorn, and Dieter Dinkler (2004). "A monolithic approach to fluid–structure interaction using space–time finite elements". In: *Computer methods in applied mechanics and engineering* 193.23-26, pp. 2087–2104.

Huhn, Florian et al. (2017). "Large-scale volumetric flow measurement in a pure thermal plume by dense tracking of helium-filled soap bubbles". In: *Experiments in Fluids* 58, pp. 1–19.

Ifju, P et al. (2002). "Flexible-wing-based micro air vehicles". In: *40th AIAA aerospace sciences meeting & exhibit*, p. 705.

Igbalajobi, A et al. (2013). "The effect of a wake-mounted splitter plate on the flow around a surface-mounted finite-height circular cylinder". In: *Journal of Fluids and Structures* 37, pp. 185–200.

Jacobi, Gunnar and Alex Nila (2021). "Simultaneous PIV and DIC Measurements in a Towing Tank Environment with a Flexible Hydrofoil". In: *14th International Symposium on Particle Image Velocimetry*. Vol. 1. 1.

Janeliukstis, Rims and Xiao Chen (2021). "Review of digital image correlation application to large-scale composite structure testing". In: *Composite Structures* 271, p. 114143.

Jeon, Young Jin et al. (2018). "Efficient reconstruction of flow field with pressure from particle tracks: VIC". In: *Bulletin of the American Physical Society* 63.

— (2019). "Data assimilation-based flow field reconstruction from particle tracks over multiple time steps". In: *Proc. 13th Int. Symp. on Particle Image Velocimetry*.

Jones, William and Jamshid Samareh-Abolhassani (1995). "A grid generation system for multi-disciplinary design optimization". In: *12th Computational Fluid Dynamics Conference*, p. 1689.

Jux, C, A Sciacchitano, and F Scarano (2020). "Flow pressure evaluation on generic surfaces by robotic volumetric PTV". In: *Measurement Science and Technology* 31.10, p. 104001.

Jux, Constantin et al. (2018). "Robotic volumetric PIV of a full-scale cyclist". In: *Experiments in Fluids* 59, pp. 1–15.

Kähler, Christian J et al. (2016). "Main results of the 4th International PIV Challenge". In: *Experiments in Fluids* 57, pp. 1–71.

Kalmbach, Andreas and Michael Breuer (2013). "Experimental PIV/V3V measurements of vortex-induced fluid–structure interaction in turbulent flow—A new benchmark FSI-PfS-2a". In: *Journal of Fluids and Structures* 42, pp. 369–387.

Kanaris, Nicolas, Dimokratis Grigoriadis, and Stavros Kassinos (2011). "Three dimensional flow around a circular cylinder confined in a plane channel". In: *Physics of fluids* 23.6.

Katz, Joseph and Allen Plotkin (2001). *Low-speed aerodynamics*. Vol. 13. Cambridge university press.

Kehoe, Michael W (1995). "A historical overview of flight flutter testing". In: *AGARD Structures and Materials Panel Meeting*. NASA-TM-4720.

King, Roger (1977). "A review of vortex shedding research and its application". In: *Ocean Engineering* 4.3, pp. 141–171.

Klimmek, Thomas (2009). "Parameterization of topology and geometry for the multidisciplinary optimization of wing structures". In: *Proceedings" CEAS 2009"*.

Kudela, Henryk and Tomasz Kozłowski (2009). "Vortex in cell method for exterior problems". In: *Journal of Theoretical and Applied Mechanics* 47.4, pp. 779–796.

Kühn, Matthias, Johannes Bosbach, and Claus Wagner (2009). "Experimental parametric study of forced and mixed convection in a passenger aircraft cabin mock-up". In: *Building and Environment* 44.5, pp. 961–970.

Kuipers, Matthew et al. (2007). "Adaptive control of an aeroelastic airbreathing hypersonic cruise vehicle". In: *AIAA Guidance, Navigation and Control Conference and Exhibit*, p. 6326.

Lee, BHK, SJ Price, and YS Wong (1999). "Nonlinear aeroelastic analysis of airfoils: bifurcation and chaos". In: *Progress in aerospace sciences* 35.3, pp. 205–334.

Lee, D and YM Tsuei (1992). "A formula for estimation of truncation errors of convection terms in a curvilinear coordinate system". In: *Journal of Computational Physics* 98.1, pp. 90–100.

Lee, Jinmo and Donghyun You (2013). "An implicit ghost-cell immersed boundary method for simulations of moving body problems with control of spurious force oscillations". In: *Journal of Computational Physics* 233, pp. 295–314.

Leishman, Gordon J (2006). *Principles of helicopter aerodynamics with CD extra*. Cambridge university press.

Lewis, Reginald Ivan (1991). "Vortex element methods for fluid dynamic analysis of engineering systems". In: *NASA STI/Recon Technical Report A* 91, p. 35539.

Liepmann, Hans Wolfgang (1952). "On the application of statistical concepts to the buffeting problem". In: *Journal of the Aeronautical Sciences* 19.12, pp. 793–800.

Liu, Dong C and Jorge Nocedal (1989). "On the limited memory BFGS method for large scale optimization". In: *Mathematical programming* 45.1-3, pp. 503–528.

Liu, GR et al. (2006). "A linearly conforming radial point interpolation method for solid mechanics problems". In: *International Journal of Computational Methods* 3.04, pp. 401–428.

Löhner, Rainald and Chi Yang (1996). "Improved ALE mesh velocities for moving bodies". In: *Communications in numerical methods in engineering* 12.10, pp. 599–608.

Luke, Edward, Eric Collins, and Eric Blades (2012). "A fast mesh deformation method using explicit interpolation". In: *Journal of Computational Physics* 231.2, pp. 586–601.

Lynch, KP and F Scarano (2015). "An efficient and accurate approach to MTE-MART for time-resolved tomographic PIV". In: *Experiments in Fluids* 56, pp. 1–16.

Maas, HG, A Gruen, and D Papantoniou (1993). "Particle tracking velocimetry in three-dimensional flows: Part 1. Photogrammetric determination of particle coordinates". In: *Experiments in fluids* 15.2, pp. 133–146.

Malik, NA, Th Dracos, and DA Papantoniou (1993). "Particle tracking velocimetry in three-dimensional flows: Part II: Particle tracking". In: *Experiments in fluids* 15, pp. 279–294.

Maljaars, PJ et al. (2020). "BEM–FEM coupling for the analysis of flexible propellers in non-uniform flows and validation with full-scale measurements". In: *Journal of Fluids and Structures* 95, p. 102946.

Marchioro, Carlo and Mario Pulvirenti (1994). "General Considerations on the Euler Equation". In: *Mathematical Theory of Incompressible Nonviscous Fluids*, pp. 1–58.

Marimon Giovannetti, Laura (2017). "Fluid structure interaction testing, modelling and development of passive adaptive composite foils". PhD thesis. University of Southampton.

McCormick, Nick and Jerry Lord (2010). "Digital image correlation". In: *Materials today* 13.12, pp. 52–54.

Mella, DA et al. (2019). "Image-based tracking technique assessment and application to a fluid–structure interaction experiment". In: *Proceedings of the Institution of Mechanical Engineers, Part C: Journal of Mechanical Engineering Science* 233.16, pp. 5724–5734.

Mendez, MA et al. (2017). "POD-based background removal for particle image velocimetry". In: *Experimental Thermal and Fluid Science* 80, pp. 181–192.

Mertens, Christoph et al. (2022). "Aeroelastic characterization of a flexible wing using particle tracking velocimetry measurements". In: *AIAA Journal* 60.1, pp. 276–286.

Michaelis, D et al. (2010). "Comparison of volume reconstruction techniques at different particle densities". In: *15th international symposium on applications of laser techniques to fluid mechanics*, pp. 3–17.

Michaelis, Dirk and Bernhard Wieneke (2019). "Comparative experimental assessment of velocity, vorticity, acceleration and pressure calculation using time resolved and multi-pulse Shake-the-Box and tomographic PIV". In: *Munich, Germany* 1.

Mitrotta, Francesco MA et al. (2019). "Experimental investigation of the fluid-structure interaction between a flexible plate and a periodic gust by means of Robotic Volumetric PIV". In: *13th International Symposium on Particle Image Velocimetry*. Universität der Bundeswehr München Neubiberg, Germany, pp. 645–656.

Montgomery, Douglas C, Elizabeth A Peck, and G Geoffrey Vining (2021). *Introduction to linear regression analysis*. John Wiley & Sons.

Morgenthal, G and Jens Honore Walther (2007). "An immersed interface method for the vortex-in-cell algorithm". In: *Computers & structures* 85.11-14, pp. 712–726.

Murai, Yuichi et al. (2007). "Particle tracking velocimetry applied to estimate the pressure field around a Savonius turbine". In: *Measurement science and technology* 18.8, p. 2491.

Neeteson, Nathan J et al. (2016). "Pressure-field extraction from Lagrangian flow measurements: first experiences with 4D-PTV data". In: *Experiments in Fluids* 57, pp. 1–18.

Nishino, Koichi, Nobuhide Kasagi, and Masaru Hirata (1989). "Three-dimensional particle tracking velocimetry based on automated digital image processing". In.

Noh, William F (1963). *CEL: A time-dependent, two-space-dimensional, coupled Eulerian-Lagrange code*. Tech. rep. Lawrence Radiation Lab., Univ. of California, Livermore.

Novara, Matteo and Fulvio Scarano (2013). "A particle-tracking approach for accurate material derivative measurements with tomographic PIV". In: *Experiments in fluids* 54.8, pp. 1–12.

Pan, Bing, LiPing Yu, and QianBing Zhang (2018). "Review of single-camera stereo-digital image correlation techniques for full-field 3D shape and deformation measurement". In: *Science China Technological Sciences* 61, pp. 2–20.

Pan, Bing et al. (2009). "Two-dimensional digital image correlation for in-plane displacement and strain measurement: a review". In: *Measurement science and technology* 20.6, p. 062001.

Panc, Vladimír (1975). *Theories of elastic plates*. Vol. 2. Springer Science & Business Media.

Parnaudeau, Philippe et al. (2008). "Experimental and numerical studies of the flow over a circular cylinder at Reynolds number 3900". In: *Physics of fluids* 20.8.

Peeters, Bart et al. (2009). "Modern solutions for ground vibration testing of large aircraft". In: *Sound and vibration* 43.1, p. 8.

Peskin, Charles S (1982). "The fluid dynamics of heart valves: experimental, theoretical, and computational methods". In: *Annual review of fluid mechanics* 14.1, pp. 235–259.

Pettit, Chris L (2004). "Uncertainty quantification in aeroelasticity: recent results and research challenges". In: *Journal of Aircraft* 41.5, pp. 1217–1229.

Pfister, J-L and Olivier Marquet (2020). "Fluid–structure stability analyses and nonlinear dynamics of flexible splitter plates interacting with a circular cylinder flow". In: *Journal of Fluid Mechanics* 896, A24.

Prasad, Anil and Charles HK Williamson (1997). "Three-dimensional effects in turbulent bluff-body wakes". In: *Journal of Fluid Mechanics* 343, pp. 235–265.

Raffel, Markus et al. (2018). *Particle image velocimetry: a practical guide*. Springer.

Raiola, Marco, Stefano Discetti, and Andrea Ianiro (2015). "On PIV random error minimization with optimal POD-based low-order reconstruction". In: *Experiments in fluids* 56, pp. 1–15.

Razavi, Seyed Esmail, Vahid Farhangmehr, and Farzad Barar (2008). "Impact of a splitter plate on flow and heat transfer around circular cylinder at low Reynolds numbers". In: *Journal of applied sciences* 8.7, pp. 1286–1292.

Reddy, Junuthula Narasimha (1999). *Theory and analysis of elastic plates and shells*. CRC press.

Roshko, Anatol (1954). *On the development of turbulent wakes from vortex streets*. Tech. rep.

Saiz, Gabriel González, Andrea Sciacchitano, and Fulvio Scarano (2022). "On the closure of Collar's triangle by optical diagnostics". In: *Experiments in Fluids* 63.8, p. 128.

Saumier, Louis-Philippe, Boualem Khouider, and Martial Agueh (2016). "Effective filtering and interpolation of 2D discrete velocity fields with Navier–Stokes equations". In: *Inverse Problems* 32.11, p. 115006.

Scanlan, RH (1978). "The action of flexible bridges under wind, I: Flutter theory". In: *Journal of Sound and Vibration* 60.2, pp. 187–199.

Scarano, Fulvio (2012). "Tomographic PIV: principles and practice". In: *Measurement Science and Technology* 24.1, p. 012001.

Scarano, Fulvio and Michel L Riethmuller (2000). "Advances in iterative multigrid PIV image processing". In: *Experiments in fluids* 29.Suppl 1, S051–S060.

Scarano, Fulvio et al. (2015). "On the use of helium-filled soap bubbles for large-scale tomographic PIV in wind tunnel experiments". In: *Experiments in Fluids* 56, pp. 1–12.

Schanz, Daniel, Sebastian Gesemann, and Andreas Schröder (2016). "Shake-The-Box: Lagrangian particle tracking at high particle image densities". In: *Experiments in fluids* 57, pp. 1–27.

Schanz, Daniel et al. (2012). "Non-uniform optical transfer functions in particle imaging: calibration and application to tomographic reconstruction". In: *Measurement Science and Technology* 24.2, p. 024009.

Schanz, Daniel et al. (2013). "'Shake The Box': A highly efficient and accurate Tomographic Particle Tracking Velocimetry (TOMO-PTV) method using prediction of particle positions". In: *PIV13; 10th International Symposium on Particle Image Velocimetry, Delft, The Netherlands, July 1-3, 2013*. Delft University of Technology, Faculty of Mechanical, Maritime and . . .

Schiavazzi, Daniele et al. (2014). "A matching pursuit approach to solenoidal filtering of three-dimensional velocity measurements". In: *Journal of Computational Physics* 263, pp. 206–221.

Schlichting, Hermann and Klaus Gersten (2016). *Boundary-layer theory*. springer.

— (2017). "Unsteady turbulent boundary layers". In: *Boundary-Layer Theory*, pp. 645–651.

Schmitt, L, K Richter, and R Friedrich (1986). "Large-eddy simulation of turbulent boundary layer and channel flow at high Reynolds number". In: *Direct and Large Eddy Simulation of Turbulence: Proceedings of the EUROMECH Colloquium No. 199, München, FRG, September 30 to October 2, 1985*. Springer, pp. 161–176.

Schneiders, Jan and Fulvio Scarano (2018). "On the use of full particle trajectories and vorticity transport for dense velocity field reconstruction". In: *19th Int Symp Appl Laser Imaging Tech Fluid Mech, Lisbon*.

Schneiders, Jan FG, Richard P Dwight, and Fulvio Scarano (2014). "Time-supersampling of 3D-PIV measurements with vortex-in-cell simulation". In: *Experiments in Fluids* 55, pp. 1–15.

Schneiders, Jan FG and Fulvio Scarano (2016). "Dense velocity reconstruction from tomographic PTV with material derivatives". In: *Experiments in fluids* 57, pp. 1–22.

Schneiders, Jan FG, Fulvio Scarano, and Gerrit E Elsinga (2017). "Resolving vorticity and dissipation in a turbulent boundary layer by tomographic PTV and VIC+". In: *Experiments in Fluids* 58, pp. 1–14.

Schröder, Andreas and Christian E Willert (2008). "Particle image velocimetry: new developments and recent applications". In.

Schröder, Andreas et al. (2022). "Large-scale volumetric flow studies on transport of aerosol particles using a breathing human model with and without face protections". In: *Physics of Fluids* 34.3, p. 035133.

Schuster, David M, Danny D Liu, and Lawerence J Huttsell (2003). "Computational aeroelasticity: success, progress, challenge". In: *Journal of Aircraft* 40.5, pp. 843–856.

Sciacchitano, Andrea, Benjamin Leclaire, and Andreas Schröder (2022). "Main results of the analysis of the HOMER Lagrangian Particle Tracking and Data Assimilation database". In: *Proceedings of the 20th International Symposium on the Application of Laser and Imaging Techniques to Fluid Mechanics*. 142, pp. 1823–1847.

Sciacchitano, Andrea, Benjamin Leclaire, and Andreas Schroeder (2021). "Main results of the first lagrangian particle tracking challenge". In: *Proceedings of 14th international symposium on particle image velocimetry*. Vol. 1. 1. ILLINOIS Tech/Paul V. Galvin Library, pp. 1–14.

Sciacchitano, Andrea and Fulvio Scarano (2014). "Elimination of PIV light reflections via a temporal high pass filter". In: *Measurement Science and Technology* 25.8, p. 084009.

Sciammarella, Cesar A (1982). "The moiré method—A review: The main developments in the area of moiré as a tool to measure displacements, contours, slopes and strains are reviewed and some typical applications are shown". In: *Experimental mechanics* 22, pp. 418–433.

Sciammarella, Cesar A and Federico M Sciammarella (2012). *Experimental mechanics of solids*. John Wiley & Sons.

Sharma, KR and Sushanta Dutta (2020). "Flow control over a square cylinder using attached rigid and flexible splitter plate at intermediate flow regime". In: *Physics of Fluids* 32.1.

Shukla, S, RN Govardhan, and JH Arakeri (2013). "Dynamics of a flexible splitter plate in the wake of a circular cylinder". In: *Journal of Fluids and Structures* 41, pp. 127–134.

Sirohi, Rajpal S (2020). "Speckle methods in experimental mechanics". In: *Speckle metrology*. CRC Press, pp. 99–156.

Smith, Marilyn J, Carlos ES Cesnik, and Dewey H Hodges (2000). "Evaluation of some data transfer algorithms for noncontiguous meshes". In: *Journal of Aerospace Engineering* 13.2, pp. 52–58.

Soifer, Victor A (2012). *Computer design of diffractive optics*. Elsevier.

Soloff, Steven M, Ronald J Adrian, and Zi-Chao Liu (1997). "Distortion compensation for generalized stereoscopic particle image velocimetry". In: *Measurement science and technology* 8.12, p. 1441.

Sutton, MA et al. (2001). "Development and assessment of a single-image fringe projection method for dynamic applications". In: *Experimental Mechanics* 41, pp. 205–217.

Taira, Kunihiko et al. (2017). "Modal analysis of fluid flows: An overview". In: *Aiaa Journal* 55.12, pp. 4013–4041.

Tarafder, Mohammad Shahjada, Goutam Kumar Saha, and Sayeed Tanvir Mehedi (2010). "Analysis of potential flow around 3-dimensional hydrofoils by combined source and dipole based panel method". In: *Journal of Marine Science and Technology* 18.3, pp. 376–384.

Taylor, George W et al. (2001). "The energy harvesting eel: a small subsurface ocean/river power generator". In: *IEEE journal of oceanic engineering* 26.4, pp. 539–547.

Turek, Stefan and Jaroslav Hron (2006). *Proposal for numerical benchmarking of fluid-structure interaction between an elastic object and laminar incompressible flow*. Springer.

Van Gent, PL et al. (2017). "Comparative assessment of pressure field reconstructions from particle image velocimetry measurements and Lagrangian particle tracking". In: *Experiments in Fluids* 58, pp. 1–23.

Van Oudheusden, Bas W et al. (2007). "Evaluation of integral forces and pressure fields from planar velocimetry data for incompressible and compressible flows". In: *Experiments in fluids* 43, pp. 153–162.

Van Oudheusden, BW (2013). "PIV-based pressure measurement". In: *Measurement Science and Technology* 24.3, p. 032001.

Vedula, Prakash and RJ Adrian (2005). "Optimal solenoidal interpolation of turbulent vector fields: application to PTV and super-resolution PIV". In: *Experiments in fluids* 39, pp. 213–221.

Virant, Marko and Themistocles Dracos (1997). "3D PTV and its application on Lagrangian motion". In: *Measurement science and technology* 8.12, p. 1539.

Walther, Jens Honoré and G Morgenthal (2002). "An immersed interface method for the vortex-in-cell algorithm". In: *Journal of Turbulence* 3.1, p. 039.

Wang, Yueqi et al. (2013). "Application of a multi-camera stereo dic set-up to assess strain fields in an erichsen test: methodology and validation". In: *Strain* 49.2, pp. 190–198.

Wang, Z and A Przekwas (1994). "Unsteady flow computation using moving grid with mesh enrichment". In: *32nd Aerospace Sciences Meeting and Exhibit*, p. 285.

Welch, Peter (1967). "The use of fast Fourier transform for the estimation of power spectra: a method based on time averaging over short, modified periodograms". In: *IEEE Transactions on audio and electroacoustics* 15.2, pp. 70–73.

Wieneke, B (2008). "Volume self-calibration for 3D particle image velocimetry". In: *Experiments in fluids* 45.4, pp. 549–556.

Wieneke, Bernhard (2012). "Iterative reconstruction of volumetric particle distribution". In: *Measurement Science and Technology* 24.2, p. 024008.

Wieneke, BFA (2017). "PIV uncertainty quantification and beyond". PhD thesis. Delft University of Technology.

Willert, Christian et al. (2010). "Pulsed operation of high-power light emitting diodes for imaging flow velocimetry". In: *Measurement Science and Technology* 21.7, p. 075402.

Willert, Christian E and Morteza Gharib (1991). "Digital particle image velocimetry". In: *Experiments in fluids* 10.4, pp. 181–193.

Williamson, Charles HK (1996). "Vortex dynamics in the cylinder wake". In: *Annual review of fluid mechanics* 28.1, pp. 477–539.

Wu, Jing, Joseph JaJa, and Elias Balaras (2013). "An optimized FFT-based direct Poisson solver on CUDA GPUs". In: *IEEE Transactions on Parallel and Distributed Systems* 25.3, pp. 550–559.

Xu, You Lin and KCS Kwok (1993). "Mode shape corrections for wind tunnel tests of tall buildings". In: *Engineering Structures* 15.5, pp. 387–392.

Zheng, Liancun and Xinxin Zhang (2017). *Modeling and analysis of modern fluid problems*. Academic Press.

Curriculum Vitæ

Gabriel González Saiz

28-12-1994   Born in Madrid, Spain.

Education

2012–2016   Bachelor in Aerospace Engineering with minor in Propulsion
                 Universidad Carlos III de Madrid
Thesis: Plasma Diagnostics with Langmuir Probe: Fabrication, Theory,
                 and Application
Promotor: Dr. X. Chen

2016–2018   Master of Science in Aerospace Engineering
                 Universidad Carlos III de Madrid (TU Delft collaboration)
Thesis: Three-dimensional jet analysis with pressure spectra estimation
                 from a single snapshot
Promotor: Dr. D. Ragni, Dr. F. Avallone & Dr. A. Ianiro

2018–2023   PhD in Aerospace Engineering - Aerodynamics
                 Delft University of Technology
Thesis: Advancements in optical diagnostics for experimental aeroelas-
                 ticity
Promotor: Prof. dr. F. Scarano & Dr. A. Sciacchitano

LIST OF PUBLICATIONS

Peer-review journals

4. Cakir, B. O., **Saiz, G. G.**, Sciacchitano, A. (submitted). Surface pressure reconstruction from LPT data with boundary conforming grids.

3. Scarano, F., Schneiders, J. F., **Saiz, G. G.**, & Sciacchitano, A. (2022). Dense velocity reconstruction with VIC-based time-segment assimilation. *Experiments in Fluids*, 63(6), 96.

2. Cakir, B. O., **Saiz, G. G.**, Sciacchitano, A., & van Oudheusden, B. (2022). Dense interpolations of LPT data in the presence of generic solid objects. *Measurement Science and Technology*, 33(12), 124009.

1. **Saiz, G. G.**, Sciacchitano, A., & Scarano, F. (2022). On the closure of Collar's triangle by optical diagnostics. *Experiments in Fluids*, 63(8), 128.

Conference proceedings

5. **Saiz, G. G.**, Sciacchitano, A., & Scarano, F. (2022). On the wake dynamics of a cylinder with flexible splitter plate. *In 20th Lisbon Laser Symposium 2022*

4. **Saiz, G. G.**, Sciacchitano, A., & Scarano, F. (2021). Towards the closure of Collar's triangle by optical diagnostics. *In 14th International Symposium on Particle Image Velocimetry*

3. Cakir, B. O., Sciacchitano, A., **Saiz, G. G.**, & van Oudheusden, B. (2021). Dense flow field interpolations from PTV data in the presence of generic solid boundaries. *In 14th International Symposium on Particle Image Velocimetry*

2. Scarano, F., **Saiz, G. G.**, & Sciacchitano, A. (2021) Velocity field reconstruction with time segment assimilation. *In Book of Abstracts.*

1. **González, G.**, Sciacchitano, A., & Scarano, F. (2019). Dense volumetric velocity field reconstruction with time-segment assimilation. *In 13th International Symposium on Particle Image Velocimetry.*